INAUGURAL - DISSERTATION

zur
Erlangung der Doktorwürde

der
Naturwissenschaftlich-Mathematischen
Gesamtfakultät

der
Ruprecht-Karls-Universität
Heidelberg

vorgelegt von

Dipl. Phys. Frank Herfurth
aus Altenburg (Thüringen)

Tag der mündlichen Prüfung: 03.05.2001

Ein neuer Ionenstrahlkühler und -pulser für ISOLTRAP und Massenmessungen an radioaktiven Argonisotopen

Gutachter: Prof. Dr. H.-Jürgen Kluge
Prof. Dr. Dirk Schwalm

Dissertation
submitted to the
Combined Faculties for the Natural Sciences and for Mathematics
of the Rupertus Carola University of
Heidelberg, Germany
for the degree of
Doctor of Natural Sciences

A new ion beam cooler and buncher for ISOLTRAP and mass measurements of radioactive argon isotopes

presented by
Diplom-Physicist Frank Herfurth
born in Altenburg (Thuringia, Germany)

Heidelberg, 03 May 2001

Referees: Prof. Dr. H.-Jürgen Kluge
Prof. Dr. Dirk Schwalm

Ein neuer Ionenstrahlkühler und -pulser für ISOLTRAP und Massenmessungen an radioaktiven Argonisotopen - ISOLTRAP ist ein Penningfallenmassenspektrometer, das an ISOLDE/CERN installiert ist. Es dient zur Massenmessung an kurzlebigen Nukliden mit einer hohen relativen Genauigkeit $\delta m/m$ von $1 \cdot 10^{-7}$. In dieser Arbeit wurde ein Ionenstrahlkühler und -pulser auf der Basis einer linearen Hochfrequenzquadrupolfalle eingebaut und charakterisiert. Damit wurde die Gesamteffizienz von ISOLTRAP um drei Größenordnungen verbessert. Das erlaubt die Messung von Nukliden die nur in kleinen Mengen produziert werden, wie zum Beispiel ^{33}Ar. In dieser Arbeit wurden die Massen von ^{33,34,42,43}Ar mit einer relativen Genauigkeit von $1 \cdot 10^{-7}$ gemessen. ^{33}Ar ist mit einer Halbwertszeit von nur 174 ms das kurzlebigste Nuklid, das jemals in einer Penningfalle untersucht wurde. Die hohe Genauigkeit der ^{33}Ar Massenmessung ermöglichte einen zwingenden Test der IMME Gleichung für die Isospin Quartette mit $A = 33$, $T = 3/2$.

A new ion beam cooler and buncher for ISOLTRAP and mass measurements of radioactive argon isotopes - ISOLTRAP is a Penning trap mass spectrometer installed at ISOLDE/CERN. It is set up to measure the mass of short-lived nuclides with a relative accuracy $\delta m/m$ of typically $1 \cdot 10^{-7}$. In this work an ion beam cooler and buncher based on a linear radio frequency quadrupole trap has been installed and characterized. By this the overall efficiency of the ISOLTRAP spectrometer was increased by three orders of magnitude. This allows for measuring nuclides that are only produced in minute quantities as for instance ^{33}Ar. In this work the mass of ^{33,34,42,43}Ar has been measured with a relative accuracy of about $1 \cdot 10^{-7}$. ^{33}Ar with its half-live of only 174 ms is the shortest-lived nuclide ever investigated in a Penning trap. The high accuracy of the mass measurement of ^{33}Ar made a stringent IMME test for the $A = 33$, $T = 3/2$ isospin quartets possible.

What is the head good for?
To shadow the body!
(Florian - Jul. 2000)

Contents

List of Figures

List of Tables

1 Introduction

Mass measurements of short-lived nuclides have been of great interest for many years. This is because the atomic mass is a gross property of a nuclide that embodies all the effects of the forces that are interplaying within its nucleus. Generally, a large-scale survey of the mass surface is needed in order to detect trends in the nuclear binding energy as well as to fit the free parameters of nuclear models. However, there are nuclides of special interest, spread all over the nuclear chart, the mass of which is often needed to an extraordinarily high precision, as for example in the context of tests of the Standard Model.

One example is the search for scalar or tensor type contributions to the Standard Model for the weak interaction. Until now the presence of this type of interaction in addition to the main contributions, the vector and axial-vector terms, is not yet ruled out by experimental investigations. Here, possible experiments are high-accuracy measurements of the kinematics of the nuclear β-decay, i.e. the angular correlation between the positron and the neutrino. Prerequisites for these experiments are the masses of the decaying nuclei and of the daughter nuclei. For example, in the recently performed experiment using the β-delayed proton emission of ^{32}Ar [Ade99] the significance of the limit on scalar contributions to the weak interaction critically depends on the accuracy of the ^{32}Ar mass.

Other examples are the tests of the Conserved Vector Current (CVC) hypothesis as well as the unitarity of the CKM matrix, which require a high-accuracy investigation of superallowed β decays. Until now nine superallowed β decays have been measured to very high precision. Additional interesting candidates in this context are ^{34}Ar, due to its large predicted Coulomb corrections, and ^{74}Rb, which provides a CVC test at high Z. In addition to the half-life and branching ratio, a very accurate Q-value of the β decay of the investigated nuclides is needed, requiring precise mass values of mother and daughter nuclei [Har99].

A third example is the isobaric multiplet mass equation (IMME), that supplies a quadratic correlation between the isospin projection and the mass of members of an isospin multiplet [Bri98]. To test this equation, the masses of at least four members of an isospin multiplet have to be known with high accuracy. Very often the mass of the most exotic and therefore shortest-lived member of an isospin multiplet is known the least accurately. Some of these masses are ground state masses and thus accessible by direct mass spectrometry.

Generally, precision and a very short half-life are contradictory which is especially true for Penning trap mass spectrometry. The high accuracy achieved in mass measurements with Penning traps [Bra99, Car99b] are based on the well defined electric and very homogeneous magnetic fields and especially, on very long observation times (up to months) that are needed to measure frequencies precisely. Unfortunately, in the case of short-lived nuclides, the observation time can not exceed the half-life by too much, limiting the accuracy.

Since the very exotic nuclides are strongly disfavored in most production reactions, the production yields are rather low compared to nuclides closer to the valley of β stability. In some unfavorable cases this is even compounded by the time required by the reaction products to diffuse out of the target matrix into the ion source. Therefore, a very efficient coupling of production and measurement apparatus is a prerequisite for investigations of very exotic and thus very short-lived nuclides. The efficient transfer from the target-ion source unit into an ion trap is therefore the subject of world-wide efforts aiming at a large variety of experiments with very exotic nuclides in ion traps. The ISOLTRAP spectrometer at the radioactive beam facility ISOLDE has played a leading role in these efforts. Both these installations are described in Chapter 2.

This work reports on mass measurements of the radioactive argon isotopes ^{33,34,42,43}Ar. With a half-life of $T_{1/2} = 174\,\mathrm{ms}$, ^{33}Ar is the shortest-lived nuclide ever investigated in a Penning trap. Since this measurement, ISOLTRAP has succeeded in measuring the mass of ^{74}Rb whose half-live of only 65 ms considerably breaks this record. ^{33}Ar is a member of an isospin quartet. The measurement accuracy allowed for a significant test of the isobaric multiplet mass equation (IMME) for the $A = 33$ and $T = 1/2$, $3/2$ and $5/2$ isospin quartets.

In order to perform these measurements the existing ISOLTRAP setup was imperatively improved by installing a linear radio-frequency ion trap as ion beam accumulator, cooler, buncher, and emittance improver, described in Chapter 3. The implementation of this device increased the sensitivity of the ISOLTRAP spectrometer by at least two orders of magnitude and preserves ISOLTRAP's capability for the measurement of all chemical species. Additionally, a very short measurement cycle was introduced for minimizing decay losses. This is described in Chapter 4 in the context of the argon mass measurements and their results.

2 Overview of the ISOLTRAP experiment

2.1 Introduction

ISOLTRAP is a Penning trap mass spectrometer installed at the on-line mass separator ISOLDE/CERN [Kug92]. It was designed to measure the mass of short-lived nuclides with very high accuracy. The masses of more than 200 nuclides have been measured so far with a typical accuracy of $\delta m/m = 1 \cdot 10^{-7}$.

From the very beginning, ISOLTRAP has consisted out of three major parts (Fig. 2.1): a beam preparation part, where the 60 keV ions delivered by ISOLDE are converted into a low-energy beam suitable for injection into a Penning trap; a cooler Penning trap for cooling, purification and bunching the ions; a high-precision Penning trap for the actual mass measurement. The first mass measurements with the ISOLTRAP spectrometer were performed in 1989 [Bol89, Sto90]. Since then not only the Penning trap used for the actual mass measurements but also the beam preparation has undergone several modifications.

The first approach used a re-ionizer placed in a buffer gas filled Penning trap, the cooler trap. The ISOLDE beam was first implanted into the re-ionizer and then released within the cooler trap where an ion bunch was formed. Later the re-ionizer was moved out of the first Penning trap to improve mass resolving power and performance of this cooler trap. Nevertheless, the spectrometer was still only applicable to surface-ionizable elements. This restriction was removed with the installation of a very large Paul trap to capture the ISOLDE ion beam in flight [Sch99]. Another restriction was the efficiency of the transformation of the ISOLDE ion beam into cooled, low-energy ion bunches. This was improved over the years but a remarkable step forward was the installation of the linear RFQ ion beam cooler and buncher as described in this work. This allows one to perform mass measurements on nuclides further away from the valley of β stability for which the production rates decrease exponentially with the increasing distance from the valley of stability.

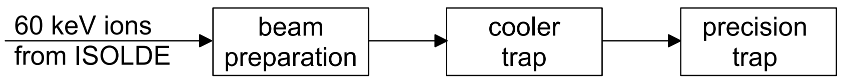

Figure 2.1: Schematic of the ISOLTRAP mass spectrometer.

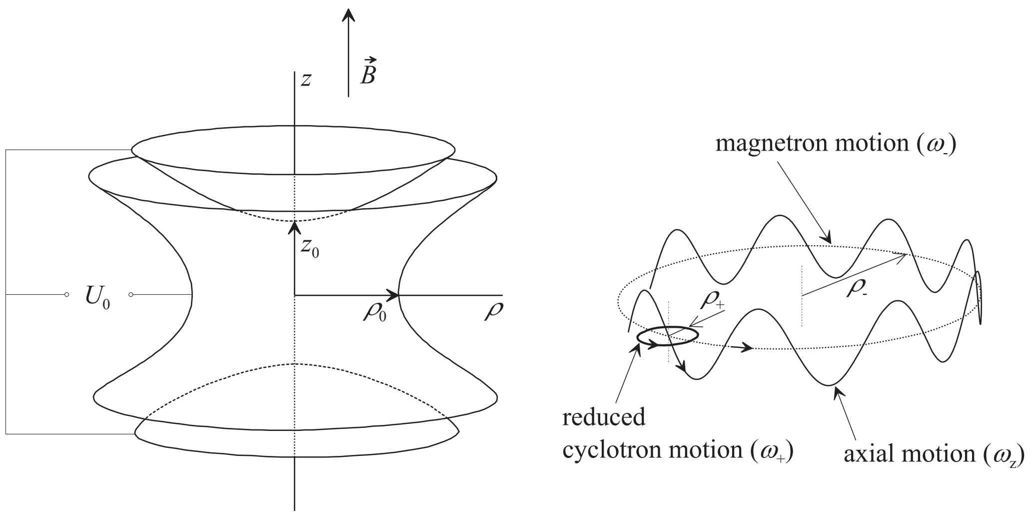

Figure 2.2: Penning trap and the orbit of a charged particle in a Penning trap.

2.2 The on-line isotope separator ISOLDE/CERN

The on-line isotope separator ISOLDE [Kug00] is part of the European organization for nuclear research (CERN) in Geneva/Switzerland. ISOLDE produces a large variety of radioactive nuclei. Since it has been and still is the world leading facility regarding the production yields of most radioactive nuclei, it is well suited for nuclear physics as well as atomic physics experiments requiring radioactive nuclei.

Proton pulses, accelerated by a linac and CERN's PS-Booster (a stack of four synchrotrons) are sent to the ISOLDE target with an energy of either 1 or 1.4 GeV. Every pulse contains up to $3 \cdot 10^{13}$ protons giving an average intensity of up to $2\,\mu$A. Radioactive nuclides are produced from the stable target nuclei by spallation, fragmentation or fission reactions. The reaction products diffuse out of the target into the ion source where they are ionized either by surface ionization, by electron impact in a hot plasma or by resonant laser ionization. The ions are extracted from the ion source, accelerated to 60 keV and sent to one of the two magnetic mass separators. The general purpose separator (GPS) can deliver the beam of radioactive ions to three different beam lines simultaneously with limited resolving power ($R_{\text{calculated}} \leq 2400$) while the high resolution separator (HRS) is capable of a mass resolving power of about 15 000 [Kug00]. In the experimental hall of ISOLDE the mass separated ion beam is delivered to the various experiments via an extensive electrostatic beam-line system.

2.3 Principle of Penning trap mass spectrometry

2.3.1 A charged particle in a Penning trap

A Penning trap is a three dimensional confining device for charged particles combining the effect of a homogeneous magnetic field $\vec{B} = B \cdot \hat{z}$ with that of an electric quadrupole field with the potential

$$U(\rho, z) = \frac{U_0}{4d^2}(2z^2 - \rho^2) \tag{2.1}$$

where U_0 is the trap voltage, ρ is the radial distance of the stored particle from the trap center and d the characteristic trap dimension. If the quadrupole potential is produced by placing three electrodes (one ring electrode and two endcaps) along the equipotential surfaces of $U(\rho, z)$ (see Fig. 2.2), then d is defined as

$$d^2 = \frac{1}{2}(z_0^2 + \frac{\rho_0^2}{2}). \tag{2.2}$$

The magnetic field in z-direction confines the charged particles to circular orbits perpendicular to the z-axis, while the electric quadrupole field confines the motion in z-direction. The equations of motions for a charged particle in these fields can be solved analytically by classical [Bro86, Kre90] or quantum mechanical means [Sok65].

The motion of a charged particle in a Penning trap can be described by three decoupled characteristic eigenmodes. In axial direction a harmonic oscillation is found, with a frequency

$$\omega_\mathrm{z} = \sqrt{\frac{qU_0}{md^2}}. \tag{2.3}$$

In the radial plane the motion consists of two circular modes, the fast, reduced cyclotron motion with frequency ω_+ and the slow magnetron motion with frequency ω_-. The reduced cyclotron motion is circular. The center of this motion, the magnetron motion, is itself a circular motion so that the trapped particle moves on an epicycle. The frequencies of the radial motions in terms of the axial frequency ω_z and the true cyclotron frequency $\omega_\mathrm{c} = q/mB$ are

$$\omega_\pm = \frac{\omega_\mathrm{c}}{2} \pm \frac{1}{2}\sqrt{\omega_\mathrm{c}^2 - 2\omega_\mathrm{z}^2}. \tag{2.4}$$

In most cases the potential created by the magnetic field is much stronger than the electric quadrupole potential and thus $\omega_+ \approx \omega_\mathrm{c}$, $\omega_+ \gg \omega_\mathrm{z} \gg \omega_-$. With this in mind, Eq. (2.4) can be expanded into a Taylor series in ω_z yielding approximations for the magnetron frequency and the reduced cyclotron frequency,

$$\omega_- \approx \frac{U_0}{2d^2B} \tag{2.5}$$

and

$$\omega_+ \approx \omega_\mathrm{c} - \frac{U_0}{2d^2B}. \tag{2.6}$$

From these approximations it is easily seen that the magnetron motion is practically mass and charge independent.

Furthermore Eq. (2.4) reveals that the sum of the two radial eigenfrequencies equals the cyclotron frequency

$$\omega_- + \omega_+ = \omega_\mathrm{c} = \frac{q}{m} \cdot B. \tag{2.7}$$

Thus, it is possible to determine the mass m of a particle with charge q in a Penning trap by measuring its cyclotron frequency if the magnetic field B is known. B can be measured via a determination of the cyclotron frequency of a reference particle with a well known mass. Hence, a direct link between a well known mass and an unknown mass is obtained by measuring the ratio of two cyclotron frequencies.

2.3.2 Excitation of the motion of the charged particle

The cyclotron frequency is measured by detecting the change in radial energy after the excitation of the motion with a radio-frequency field. The radial energy is given by [Bro86, Bol89]

$$\begin{aligned} E_\rho &= \tfrac{m}{2}\left[\rho_+^2(\omega_+^2 - \omega_+\omega_-) + \rho_-^2(\omega_-^2 - \omega_+\omega_-)\right] \\ &= (E_+^\mathrm{kin} + E_+^\mathrm{pot}) + (E_-^\mathrm{kin} + E_-^\mathrm{kin}) \end{aligned} \tag{2.8}$$

with the radius of the reduced cyclotron motion ρ_+ and the radius of the magentron motion ρ_- (See also Fig. 2.2). Since $\omega_+ > \omega_-$, the magnetron motion is dominated by its negative potential energy. An important consequence is that an increase of the radius of the magnetron motion causes a decrease in radial energy.

The application of an azimuthal radio-frequency *dipole* field in the trap leaves the three characteristic motions decoupled. If the radio frequency is equal to the frequency of one of the radial eigenmotions, the amplitude of this motion increases with time. This can be used to perform a mass selective cleaning procedure by exciting the reduced cyclotron motion until the cyclotron radius is larger than the trap radius and the particles are lost. It can also be used to place all particles regardless their mass on a defined magnetron radius by exciting the magnetron motion for the corresponding time period.

An azimuthal radio-frequency *quadrupole* field couples the two radial eigenmotions. If the RF-frequency is equal to the cyclotron frequency ω_c an initial motion which is pure magnetron will periodically be converted into a pure cyclotron motion and back. This can be used to detect the cyclotron frequency of a stored particle observing the radial energy change that is caused by this conversion [Bol90].

2.4 ISOLTRAP - experimental setup

Figure 2.3 shows an overview of the layout of the Penning trap mass spectrometer ISOLTRAP. It consists of three main parts: (1), a linear gas-filled radio-frequency

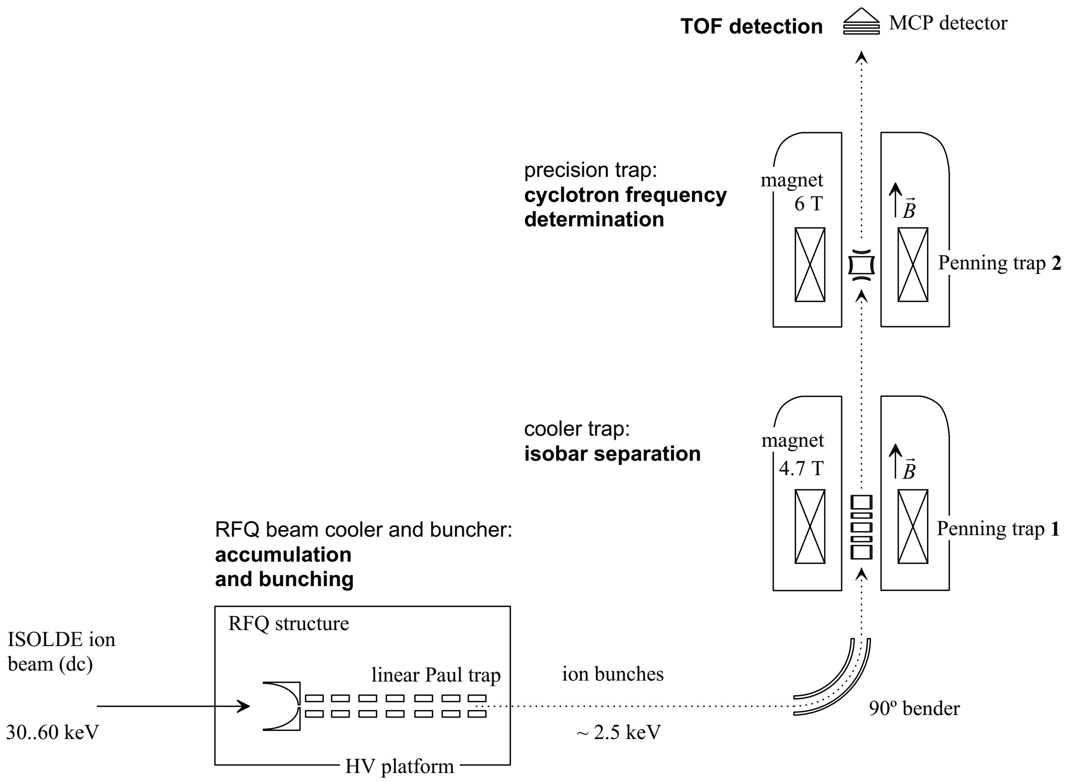

Figure 2.3: Experimental setup of the ISOLTRAP Penning trap mass spectrometer. The three main parts are: (1), a linear gas-filled radio-frequency quadrupole (RFQ) trap for retardation, accumulation, cooling and bunched ejection at low energy, (2), a gas-filled cylindrical Penning trap for further cooling and isobaric separation, and (3), an ultra-high vacuum hyperboloidal Penning trap for isomeric separation and the actual mass measurement.

quadrupole (RFQ) trap for retardation, accumulation, cooling and bunched ejection at low energy, (2), a gas-filled cylindrical Penning trap for further cooling and isobaric separation, and (3), an ultra-high vacuum hyperboloidal Penning trap for isomeric separation and the actual mass measurement. The detailed function and performance of the two Penning traps are described in [Bol96, Rai97]. The recently added linear Paul trap is discussed in [Her00] and in Chapt. 3.2. Nevertheless, a short overview will be given here, illustrating the principles of operations and the basic features of the setup.

The linear RFQ trap acts as an ion beam cooler and buncher for the 60-keV ion beam delivered by ISOLDE. It transforms the quasi-continuous 60-keV ion beam into short ion bunches at low energy. This is required in order to efficiently transfer the ions to the first Penning trap and to capture them there.

This cylindrical Penning trap, the so called "cooler" trap (see Fig. 2.4), is filled with helium buffer gas [Rai97]. The tasks of this trap are the purification of the ion cloud from contaminating ions and the preparation of a cold ion bunch. This provides optimal and reproducible starting conditions for the mass measurement performed in the precision

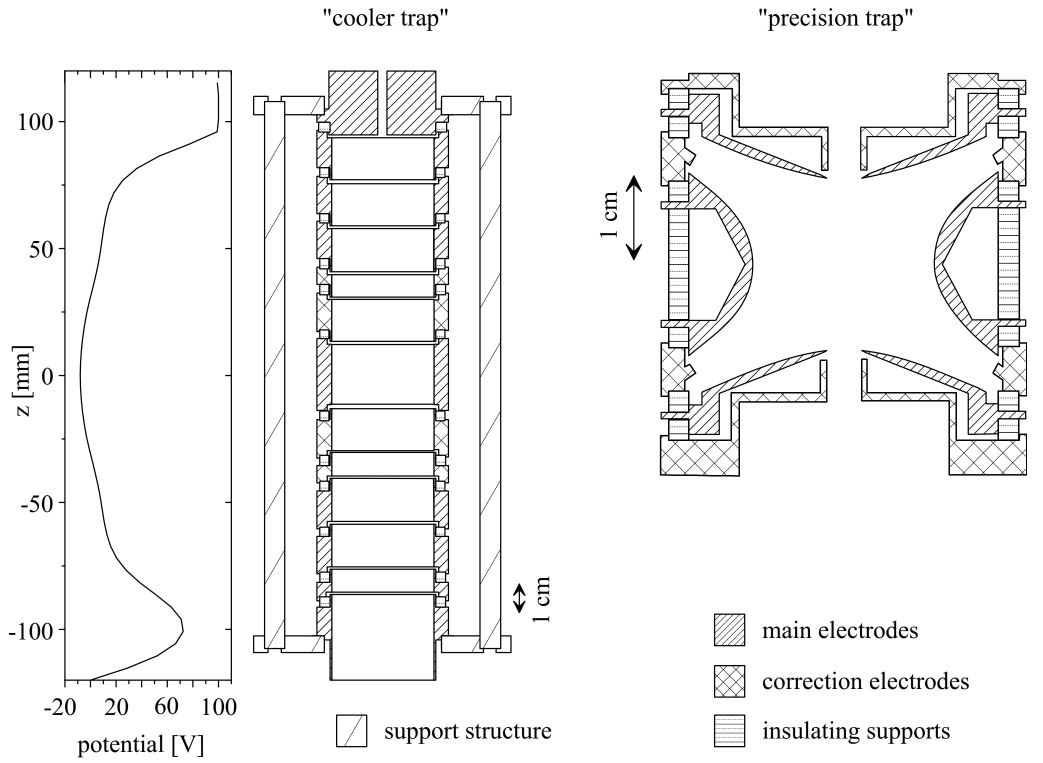

Figure 2.4: The two Penning traps of ISOLTRAP. Also depicted is the potential in the cooler trap. Note that the precision trap is enlarged with respect to the cooler trap.

trap.

The cooler trap is built of 13 electrodes that allow the formation of a nested trap (see trap potential in Fig. 2.4). The outer box-shaped potential well serves for an efficient ion capture. The inner part is carefully shaped to form a quadrupole potential over a large volume. This avoids mass dependent frequency shifts in the ion motion, which finally limit the achievable mass resolving power.

The second trap is a high-precision, compensated, hyperbolical Penning trap (see Fig. 2.4). This trap design incorporates two sets of correction electrodes. With the inner correction electrodes the finite dimensions of the hyperbolical electrodes is compensated. The correction electrodes just outside the entrance and exit holes minimize the perturbation of the hyperbolical trap potential by the “missing” conducting boundary. This trap is used for the mass measurement of the ions delivered by the first Penning trap by determining their cyclotron frequency using a time-of-flight technique [Grä80].

A multi-channel plate detector (MCP) installed at the very top of the experimental setup (see Fig. 2.3) is used for single ion counting. The detector consists of two multi-channel plates in a chevron arrangement. Typical detection efficiencies for this type of detector range from 30 to 60% [Bre95, Obe97].

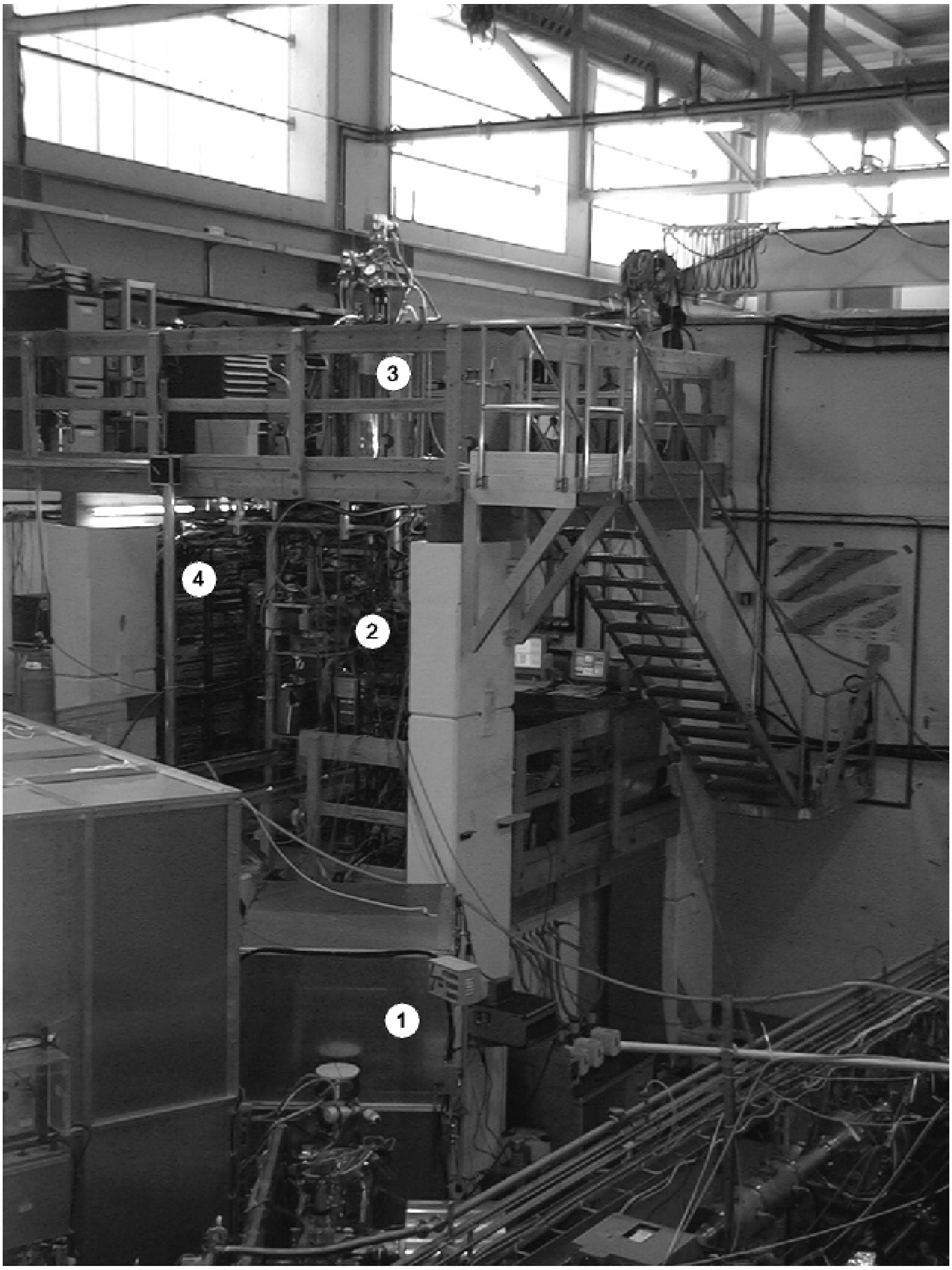

Figure 2.5: ISOLTRAP overview photograph. Visible are: 1) the high-voltage cage housing the RFQ ion beam cooler and buncher, 2) the first floor with the vessel of the superconducting magnet (4.7 T) of the cooler Penning trap, 3) the vessel of the superconducting magnet (5.9 T) of the precision trap, 4) the racks containing the HV-supplies and control electronics for the two Penning traps.

2.5 ISOLTRAP - experimental procedure

The ions are produced either in the ISOLDE ion source (see also Sect. 2.2) or in the ISOLTRAP test ion source used to tune the spectrometer (see App. A). The continuous ion beam is sent to the ISOLTRAP ion beam cooler and buncher. In most cases a beam gate allows only a fraction of the ion beam to enter the ion beam cooler and buncher to avoid overloading the precision trap. After a certain time an ion cloud is formed in the potential well at the end of the ion beam cooler and buncher. This ion cloud is ejected in a bunch and sent to the cooler trap.

In the cooler trap the ion bunch is captured dynamically in flight by synchronizing the voltage applied to the electrodes on the entrance side of the outer potential well. The captured ions are then cooled axially to room temperature by collisions with the buffer gas atoms. The axial cooling forces them to accumulate in the inner harmonic potential well.

In this inner potential well also radial cooling takes place by a combination of buffer gas collisions and RF excitation at ω_c. According to Eq. 2.8 the radius of the cyclotron motion shrinks while the magnetron radius expands with time. By applying a radio frequency quadrupole field at the cyclotron frequency ω_c of the stored particles, the two radial motions are coupled [Bol90] and both motions are cooled [Sav91].

The fact that the coupling works only at the cyclotron frequency $\omega_\mathrm{c} = q/mB$, can be used for a mass selective cooling scheme. At ISOLTRAP the following procedure is used. First an RF dipole field is applied to increase the magnetron radius of all ions regardless their mass. This radius is larger than the exit hole of the cooler trap (diameter $d = 3\,\mathrm{mm}$) which means the ions must be re-centered if they are to be extracted. This is done using the mass selective azimuthal quadrupole excitation. This mass selective cooling scheme allows the operation of the trap as an isobar separator with a resolving power of up to $R \approx 10^5$ for ions with mass number $A \approx 100$ [Rai97].

The reachable resolving power depends mainly on the buffer gas pressure. The highest resolving power is reached for low buffer gas pressure. Low buffer gas pressures, however, result in long cooling and excitation times [Kön95]. If it is necessary to cool very fast, a relatively high buffer gas pressure ($\approx 10^{-4}\,\mathrm{mbar}$) is chosen. This restricts the reachable resolving power to $R \approx 10^4$.

The ions delivered by the cooler trap are dynamically captured in flight in the precision trap by switching the voltage of its lower end cap. At the correct switching time the axial energy of the ions is minimal after trapping since the trap center of the precision trap is on the same potential as the trap center of the cooler trap.

The ion motion is excited in two steps. First an azimuthal radio frequency (RF) dipole field with $\omega_\mathrm{RF} = \omega_-$ is applied for a certain time to prepare a defined magnetron amplitude. Then the ion motion is excited by an azimuthal RF quadrupole field with $\omega_\mathrm{RF} = \omega_\mathrm{c}$ of the stored particle. If the RF-field has the correct amplitude and duration, the initial magnetron motion is transferred to cyclotron motion and therefore the radial energy is increased (see Eq. 2.8). After ejection at low axial energy, the particle drifts through the

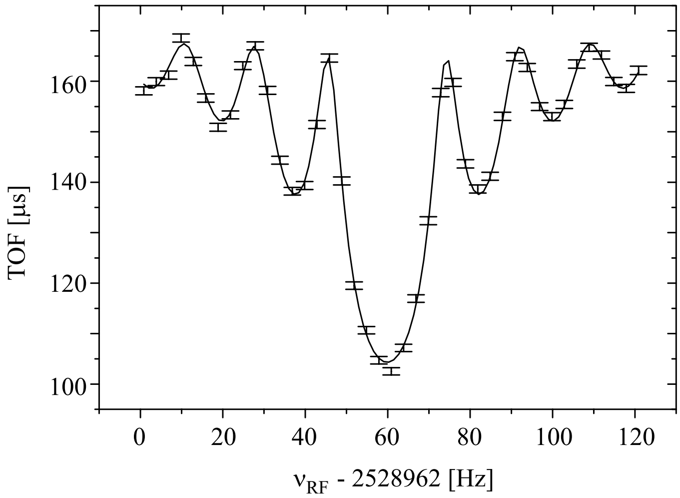

Figure 2.6: Cyclotron resonance curve for ^{36}Ar. Shown is the time of flight (TOF) of the ions from the trap to the ion detector as a function of the applied radio frequency. The solid line is a fit of the theoretical line shape [Kön95] to the data points.

inhomogeneous part of the magnetic field. There, the orbital magnetic moment of the ion that is proportional to its radial energy causes the ion to be accelerated corresponding to the magnitude of the magnetic moment. Thus, if $\omega_{\mathrm{RF}} = \omega_{\mathrm{c}}$, the ejected ion will arrive at the ion detector earlier than in the case of $\omega_{\mathrm{RF}} \neq \omega_{\mathrm{c}}$.

As an example, Fig. 2.6 shows a cyclotron resonance curve for ^{36}Ar. Depicted is the time of flight (TOF) of the ions from the trap to the ion detector as a function of the applied radio frequency. The solid line is a fit of the theoretical line shape [Kön95] to the data points. Since the formation of the time-of-flight spectrum is well understood the fitted line reproduces the measured points perfectly.

The line width of the resonance curve is mainly determined by the period of time the RF-field is applied for coupling the two radial motions. The characteristics of the radial-to-axial energy conversion have an additional (small) influence on the width. Using the time of flight detection scheme an experimental line width

$$\Delta\nu(\mathrm{FWHM}) \approx \frac{0.9}{T_{\mathrm{RF}}} \tag{2.9}$$

is reached with an excitation time T_{RF}. Therefore, the mass resolution and also the precision of the determination of the cyclotron frequency depends strongly on the excitation time.

3 A linear Paul trap as an ion beam cooler and buncher

3.1 Introduction

The development of new techniques for the manipulation of radioactive ion beams is actively pursued by several groups world-wide. One of the main objectives is a better matching of the properties of the radioactive ion beams to the specific requirements of the experiments. Here ion trap techniques have started to play an increasingly important role, in particular for the accumulation, cooling, and bunching of these beams. Both, Penning traps [Bol97, Ame98, Sch01] and radio-frequency multipole ion traps or guides [GR92] can fulfill this task. In addition, Penning traps offer high-resolution mass separation and can be used for beam purification [Rai97]. Radio-frequency multipole ion guides have been employed in ion chemistry and molecular physics for many years [Tel74, Ger92]. Now they have gained increasing importance in the field of nuclear physics, where they are used for guiding charged nuclear reaction products from high-pressure gas cells into high-vacuum regions in order to form low-energy radioactive ion beams [Kud98, Fuj97, Pen97, Sav99] or for enabling ultra-sensitive laser experiments on radioactive ions [Bac97].

A rather new application is the use of radio-frequency multipole systems for the manipulation and improvement of radioactive ion beams as they are available from on-line mass separators. Already several years ago, a development of an ion beam accumulator based on a Paul trap system was started. Its task was the conversion of the continuous 60-keV ISOLDE ion beam into low-energy, low-emittance ion bunches that can be transferred with high efficiency into the ISOLTRAP mass spectrometer. Such a system [GR92, Sch99] was indeed realized and has been used successfully in the ISOLTRAP experiment [Sch99]. However, it was found that the acceptance of the Paul trap system was not well matched to the ISOLDE beam emittance and that the ejection of the ions out of the system was very critical. Therefore, a new technical approach had to be found that preserves the advantages of the earlier Paul trap system, like element independence, but avoids the mentioned difficulties.

As a solution, within this work, a beam accumulator, cooler, buncher, and emittance improver based on a linear radio-frequency quadrupole (RFQ) ion trap has been realized and used for on-line physics experiments. In the following the working principles and characteristics of this new beam handling device will be presented.

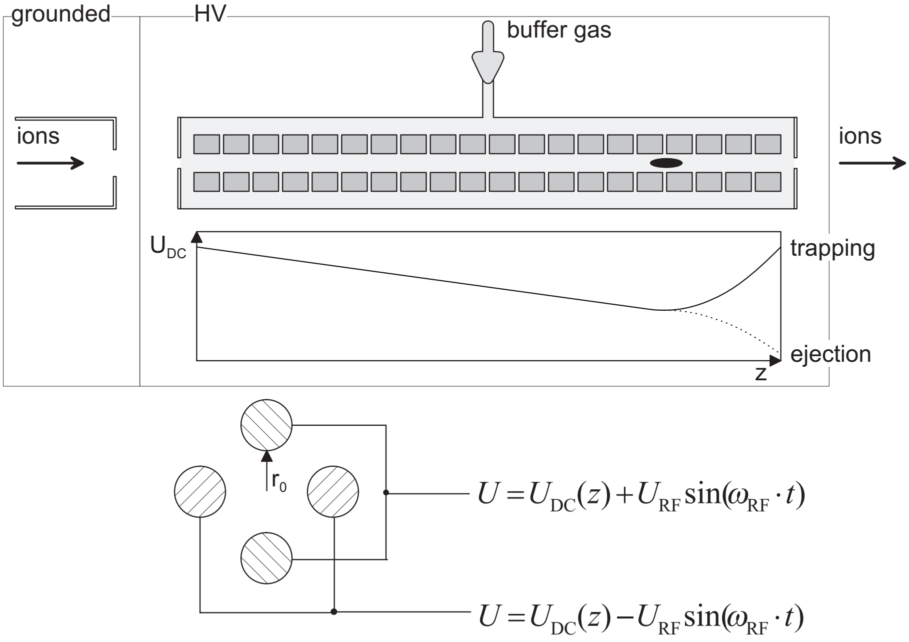

Figure 3.1: Basic scheme of a radio-frequency ion beam cooler and buncher. The upper figure shows a schematic side view of such a system together with the potential along the symmetry axis. The lower figure shows a transverse cut of the four rods and the applied radio-frequency and DC voltages.

3.2 Principle of the ISOLTRAP ion beam cooler and buncher

The principle of the ISOLTRAP ion beam cooler and buncher is illustrated in Fig. 3.1. The 60-keV ISOLDE ion beam is electrostatically retarded to an energy of a few eV and injected into a linear radio-frequency quadrupole ion trap, which is filled with a buffer gas. The trap system consists of four segmented rods to which radio-frequency voltages are applied so as to obtain a transversely focusing force. The segmentation of the rods allows the creation of a DC electric field along the axis of the system. Ions entering the linear trap will lose transverse and longitudinal energy due to collisions with the buffer gas. They are finally accumulated in the potential well at the end of the system forming an ion bunch. By switching the potential of the last rod segments, as indicated in the figure, the ion bunch can be extracted. For a discussion of the principle of similar devices used as an ion guide see [Lun99, Kel00].

3.2.1 Linear radio-frequency quadrupole ion traps

The confinement of an ion in a linear RFQ trap as presented here is achieved by combining a static trapping potential V_{DC} along the axis of the system with a radial confinement. The latter results from the interaction of the trapped ion with a radio-frequency quadrupole field generated by the RF voltages applied to the rods of the system.

The radial confinement in a quadrupolar field can be described in terms of the Mathieu equations [Daw76, Pau90], which also define the stability criteria of the motion. It is useful to consider the resulting motion as being that of a particle in a pseudopotential well [Deh67] of depth V_{RF}. While the electric field configuration of the linear trap produces motions that cannot be exactly described in terms of the Mathieu functions (due to the strong radial and azimuthal dependence of the axial field), it is still useful to consider the first-order solution of the motion as a linear superposition of the DC axial field potential and the RF quadrupole pseudopotential.

The pseudopotential is generated by radio-frequency voltages with amplitudes $\pm U_{\mathrm{RF}}$ and angular frequency ω_{RF}. As shown in Fig. 3.1, these voltages are applied with 180° phase difference to pairwise connected opposite elements of a quadrupole rod system. The separation between the surfaces of opposite electrodes is $2r_0$. The resulting pseudopotential is given by

$$V_{\mathrm{RF}}(r) = \frac{q \cdot U_{\mathrm{RF}}}{4r_0^2} r^2 \tag{3.1}$$

where

$$q = 4\frac{eU_{\mathrm{RF}}}{mr_0^2\omega_{\mathrm{RF}}^2} \tag{3.2}$$

is the relevant Mathieu parameter and e and m are the charge and mass of the stored ion. The solution of the Mathieu equation shows that the motion is stable as long as $q < 0.908$. However, the pseudo potential approximation is only applicable for small q parameters, i.e. $q < 0.4$. In the radio-frequency field, the ion performs a micro-motion at the frequency ω_{RF} of the field and a macro-motion that can be understood as an oscillation in the pseudopotential V_{RF}. To a good approximation for $q < 0.4$, its oscillation frequency is

$$\omega_{\mathrm{m}} = \frac{q}{\sqrt{8}}\omega_{\mathrm{RF}} \quad . \tag{3.3}$$

As an example, a singly charged ion with mass number $A = 39$ in a four-rod structure with $r_0 = 6\,\mathrm{mm}$ operated with $\omega_{\mathrm{RF}} = 2\pi \cdot 1\,\mathrm{MHz}$, $U_{\mathrm{RF}} = 80\,\mathrm{V}$ will experience a depth of the radial trapping potential of about 11 V in which it oscillates with $\omega_{\mathrm{m}} = 196\,\mathrm{kHz}$.

As illustrated in Fig. 3.1, the axial confinement is provided by applying different DC voltages to the rod segments in order to create a potential gradient along the trap axis. The minimum of the potential curve can be approximated by a parabola $V_{\mathrm{DC}}(r = 0, z) = (U_{\mathrm{DC}}/z_0^2) \cdot z^2$ defined by the characteristic length z_0 and voltage U_{DC}. Since $\triangle V_{\mathrm{DC}}(r, z) = 0$, the corresponding axisymmetric quadrupole potential is

$$V_{\mathrm{DC}}(r, z) = \frac{U_{\mathrm{DC}}}{z_0^2}\left(z^2 - \frac{r^2}{2}\right) \quad . \tag{3.4}$$

In the region where the DC potential along the trap axis has its minimum, the radial confinement due to the radio-frequency field is counteracted by the repelling radial part of the DC potential. The overall potential close to the trap minimum then becomes

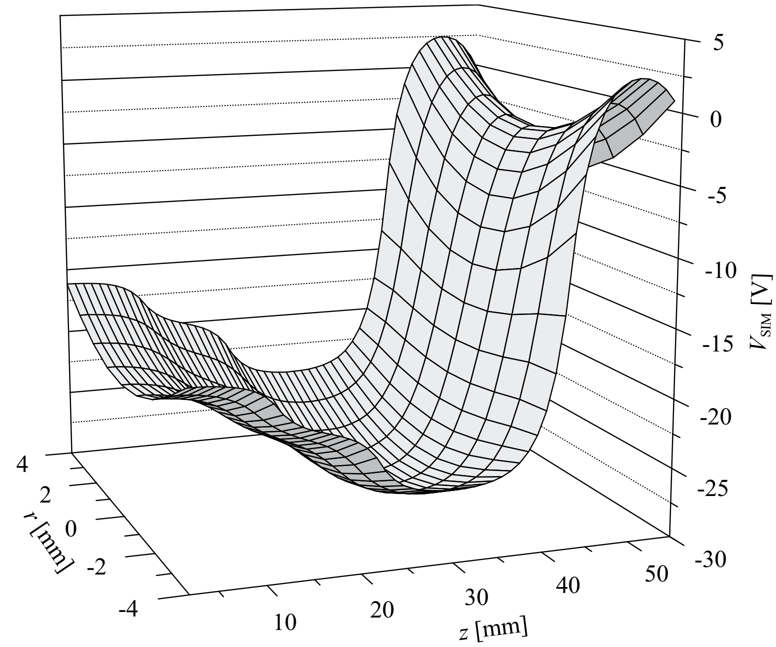

Figure 3.2: Overall potential of the RFQ trap for mass $A = 133$ and parameters presented in Sect. 3.4.0.

$$\bar{V}(r,z) = \frac{U_{\mathrm{DC}}}{z_0^2} z^2 + \left(\frac{q}{4} \frac{U_{\mathrm{RF}}}{r_0^2} - \frac{U_{\mathrm{DC}}}{2z_0^2} \right) r^2 \quad . \tag{3.5}$$

With the parameters used above and $U_{\mathrm{DC}}/z_0^2 = 10\,\mathrm{V/cm}^2$, the radial trapping potential well is reduced by about 1.8 V compared to the RF-only case. From Eq. 3.5 the condition

$$U_{\mathrm{RF,min}} = r_0^2 \cdot \omega_{\mathrm{RF}} \sqrt{\frac{m}{e} \frac{U_{\mathrm{DC}}}{2z_0^2}} \tag{3.6}$$

can be derived for the minimum RF voltage required for three-dimensional ion trapping.

3.2.2 Realistic potential shape

The pseudo potential and the DC potential in the trap region as given in the preceding section have been assumed to be of pure quadrupolar shape. However, the segmentation and the non-hyperbolical shape of the electrodes together with the voltages applied give rise to higher order multipoles in the potential.

The pseudo potential created by an inhomogeneous RF field

$$\vec{E}(x,y,z,t) = \vec{E}_0(x,y,z) \cos(\omega_{\mathrm{RF}} t) \tag{3.7}$$

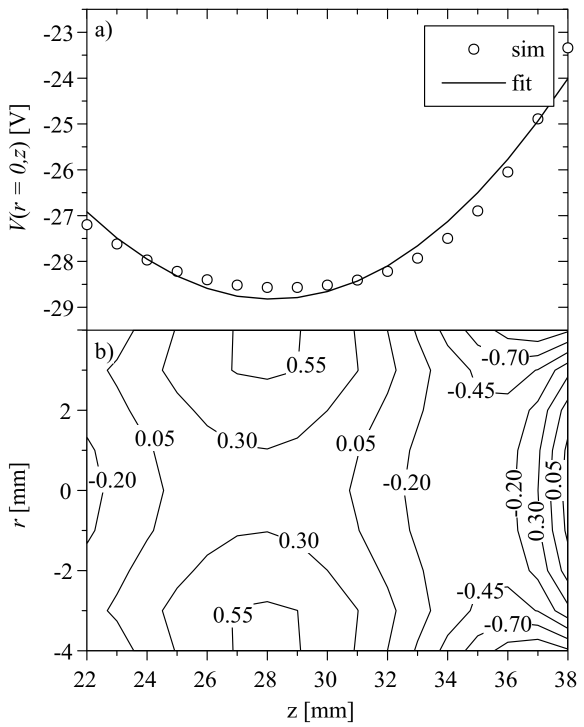

Figure 3.3: a) The potential $V(r,z)$ plotted versus z for $r = 0$. The points are the values resulting from an overall potential calculation with SIMION 3D 6.0 using the real geometry and voltages. The line is the potential from (3.5) with U_{DC}/z_0^2 adjusted to be $3.9\,\mathrm{V/cm^2}$. b) The difference of the simulated overall potential $V_{\mathrm{SIM}}(r,z)$ and the potential $\bar{V}(r,z)$ from (3.5) plotted in Volt.

with amplitude $\vec{E}_0(x,y,z)$ is for a small parameter q given by [Deh67]

$$V_{\mathrm{RF}}(x,y,z) = \frac{e}{4m\omega_{\mathrm{RF}}^2}\vec{E}_0^2 \quad . \tag{3.8}$$

For the rod system of the ISOLTRAP cooler and buncher the amplitude $\vec{E}_0^2$ has been calculated with the ion optics calculation program SIMION 3D 6.0. This program, written by David A. Dahl, uses finite difference solution techniques for solving electrostatic boundary value problems. For given mass number and operational parameters of the trap this allows one to obtain a realistic picture of the pseudo-potential. This can be superimposed to the DC-potential created by the segmented electrodes, which has also been calculated with SIMION. Using the trap parameters as listed in Tab. 3.1 and Tab 3.2 an overall potential V_{SIM} is obtained as shown in Fig. 3.2 for the case of ions with mass number 133.

Two features are observed: the potential well in radial direction is rather shallow compared to that in the axial direction. The latter is highly asymmetric with modest potential decrease towards the potential minimum and a steep increase as one preceeds further towards the trap exit.

Only very close to its minimum the potential can be approximated by a harmonic potential. Fig. 3.3 a shows the potential in this region along the axis of the system together with a fit by a parabola. Fig. 3.3 b shows the difference between V_{SIM} and the potential $\bar{V}(r,z)$ obtained by Eq. 3.5 using the characteristic parameter $U_{\mathrm{DC}}/z_0^2 = 3.9\,\mathrm{V/cm^2}$ resulting from the fit. But due to the strong asymmetry of the potential in axial direction the characteristic parameter symbolizing the potential gradient is drastically changing towards the trap exit. This causes the radial trapping potential to be almost cancelled in the region $40 \leq z \leq 50\,\mathrm{mm}$ hindering the trapping of ions that are not well cooled when they arrive at this position.

3.2.3 Buffer gas cooling

After the ions have entered the linear radio-frequency quadrupole, they interact with the buffer gas. The ions are elastically scattered at the buffer gas atoms transferring part of their energy to them. Thus, the motion of the ions is damped until they finally come into thermal equilibrium with the buffer gas in the minimum of the trapping potential.

To study the overall cooling process, it is sufficient to describe the action of the gas as that of a viscous force. However, for an understanding of ion loss mechanisms and final ion temperatures, a microscopic modeling of the deceleration and cooling process including the radio-frequency field is required. Various calculations of both kinds have been carried out for the system presented here. In the following the most basic aspects of buffer gas cooling in such a system will be discussed.

For low ion energies (less than a few eV), the damping of the ion motion is dominated by the long-range interaction of the ion with buffer gas atoms polarized by this ion. This interaction results in an average damping force

$$\vec{F} = -\delta \cdot m \cdot \vec{v} \quad , \tag{3.9}$$

where m and v are the mass and the velocity of the ion. The damping coefficient

$$\delta = \frac{e}{m}\frac{1}{\mu}\frac{p/p_{\mathrm{N}}}{T/T_{\mathrm{N}}} \tag{3.10}$$

is proportional to the gas pressure p (in fractions of the normal pressure p_{N}) and inversely proportional to the temperature T (in fractions of the normal temperature T_{N}) and the reduced ion mobility μ [McD73], which for low kinetic energies of the ions is constant for a given ion species and type of buffer gas. For kinetic energies $> 1\,\mathrm{eV}$ the ion mobility decreases (see discussion in [Lun99]). For the purpose of this work it is sufficient to take the constant low-energy values as an upper limit for the ion mobility.

Figure 3.4 illustrates the cooling and accumulation process in a linear trap with an axial potential as shown in Fig. 3.1. The simulation has been performed for a $^{39}\mathrm{K}^+$ ion entering the system with an initial kinetic energy of $E_{\mathrm{kin}} = 10\,\mathrm{eV}$. The axial potential well depth is $V_{\mathrm{z0}} = 50\,\mathrm{V}$ and the trap has a total length of $L = 1\,\mathrm{m}$ with the potential minimum at $l_0 = 0.8\,\mathrm{m}$. A helium buffer gas pressure of $p_{\mathrm{He}} = 10^{-2}\,\mathrm{mbar}$ has been used. With an ion mobility $\mu(\mathrm{K}^+ - \mathrm{He}) = 2.15 \cdot 10^{-3}\,\mathrm{m^2/Vs}$, the damping constant reaches a value of $\delta = 11500\,\mathrm{s}^{-1}$. As can be seen in Fig. 3.4(a) and (b), both the axial and the radial oscillation

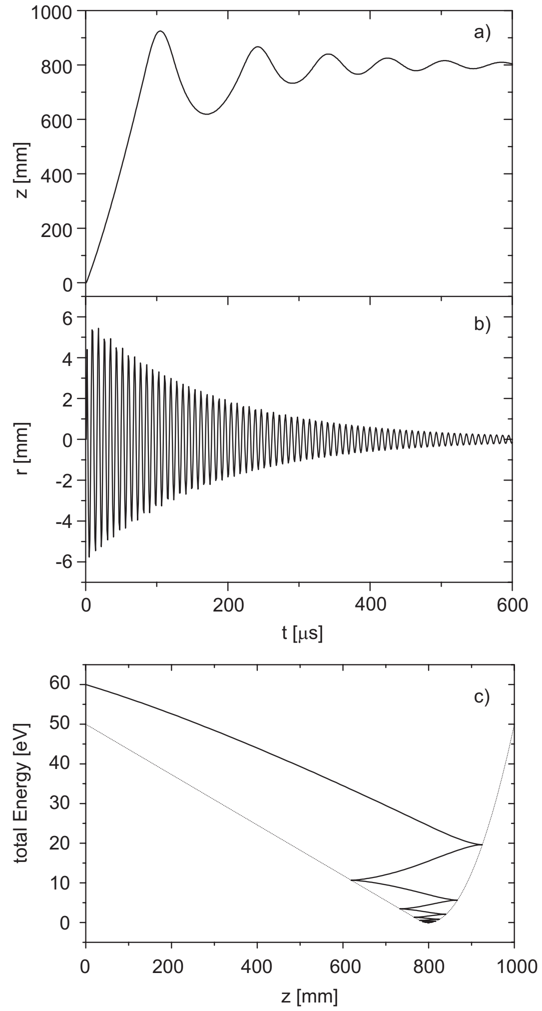

Figure 3.4: Simulation of the accumulation and cooling process in a linear RFQ trap: a) the axial oscillation as a function of time, b) the radial oscillation as a function of time, and c) the total axial energy as a function of the axial position (shown together with the axial potential).

amplitude of the ion are damped very quickly. Even more illustrative is Fig. 3.4(c) which shows the total energy of the ion as a function of the axial position. Already during its first oscillation in the system the ion loses more than 50 % of its initial total energy. The equilibrium with the buffer-gas temperature is reached within about 1 ms.

The viscous damping approach presented above is valid at low velocity for ions with masses much heavier than the mass of the buffer gas atoms. Therefore, in the case of Cs ions in He, the viscous damping description is adequate. This changes as soon as lighter ions or heavier buffer gas atoms are used. This is illustrated in Figure 3.5. A comparison of the ion motion in the first (linear potential) part of the quadrupole system is shown, as calculated under the assumption of viscous damping and in a full Monte-Carlo calculation. In this calculation the trajectories of the ions have been investigated using realistic interaction

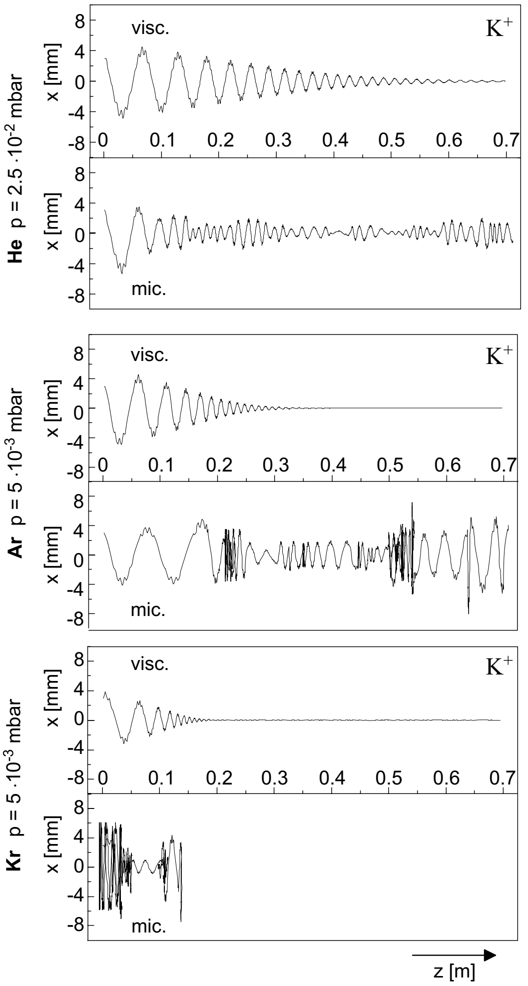

Figure 3.5: Comparison of ion damping in a linear cooler as obtained by calculations based on a viscous damping approach (**visc**) and a microscopic description (**mic**). Shown is the radial position of the ions as a function of their axial position. The calculations have been performed for K^+ in He, Ar, and Kr at different pressures.

potentials for the collision of the ions with the buffer-gas atoms (details of this microscopic calculation are discussed in [Sch99]).

For K ions in He a cooling effect can be observed only in time average. If Ar is used as buffer gas only very few K ions pass through the quadrupole system (one example trajectory is shown in Fig. 3.5) and no net cooling effect can be observed. In the case of K^+ in Kr, the motion becomes unstable very quickly and the ion is radially ejected out of the system. The reason is that the micro-motion of an ion colliding with a heavier atom can make a phase jump with respect to the driving radio-frequency which leads to an increase of the kinetic energy. This process is called RF-heating. In the case of ions having a mass equal or smaller than the buffer gas atoms it is the predominant cause of ion loss from RFQ traps.

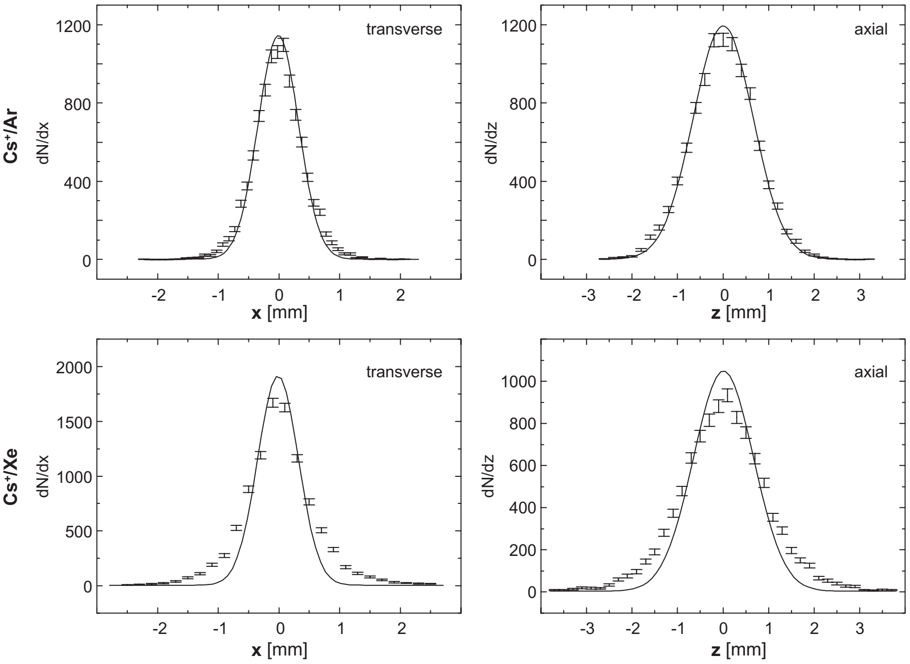

Figure 3.6: Transverse and axial amplitude distribution of Cs ions in the potential minimum of the linear ion trap. The solid curves show distributions for an ion cloud temperature of 300 K in the total static (pseudo)-potential. The points are the result of a microscopic calculation taking the RF field and ion-atom collisions into account.

In order to determine the properties of ion bunches extracted from the trap, one must know the final spatial distribution of the trapped and cooled ions. As a first approach the form of the overall potential in the trap center from Eq. 3.5 and the parameters used above are taken assuming that the ions reach a final temperature $T = 300\,\mathrm{K}$ equal to that of the buffer gas. Assuming Boltzmann distributions, axial and transverse distributions as shown as solid curves in Fig. 3.6 are obtained for Cs^+ ions. The points are the result of a microscopic calculation. It can be seen that the oscillating electrical field and the collisions with the gas have only a very small effect on the ion distribution for Cs^+ in Ar but a significant one for Cs^+ in Xe. Practically no effect is seen for Cs^+ in He (not shown in Fig. 3.6).

3.2.4 Ion injection and extraction

Deceleration and injection

In order to stop an energetic ion beam in the linear ion trap by gas collisions, first the beam has to be decelerated to low energies (in the order of 10 eV). This can be accomplished by placing the whole ion trap on a potential slightly below the corresponding ion beam energy. With reduction of energy the divergence of the beam increases. Therefore, the original emittance of the ion beam will determine how far the energy of the beam can

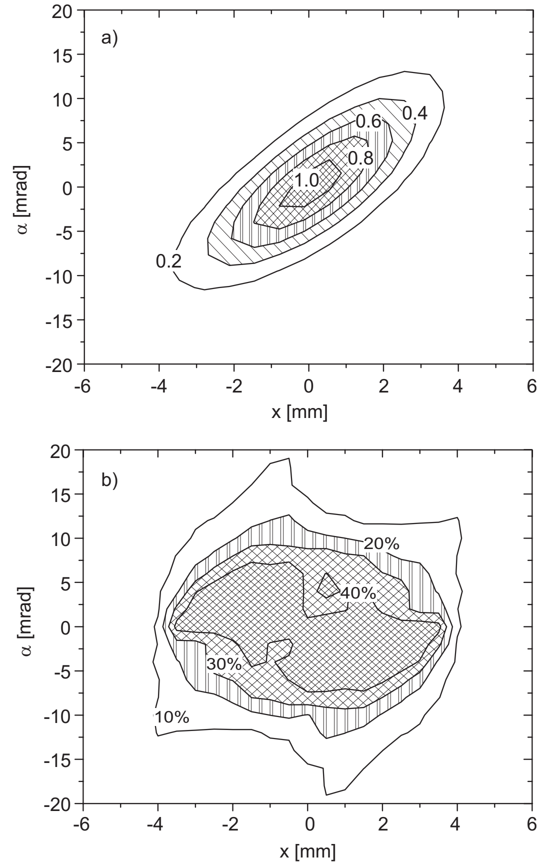

Figure 3.7: a): Calculated emittance diagram of the ISOLDE ion beam. Shown is the ISOLDE beam intensity (in arbitrary units) as a function of beam displacement x and angle α. b): Corresponding acceptance diagram of the ISOLTRAP ion cooler and buncher for x and α. Shown is the probability of successful ion injection, obtained by averaging over the results of the beam parameters y and β and all RF phases.

be reduced by electrostatic means. For example, an ion beam of $E_0 = 60\,\mathrm{keV}$ with an emittance of $\epsilon = 35\,\pi\,\mathrm{mm\,mrad}$ that is decelerated to $E_1 = 20\,\mathrm{eV}$ and focused to fit through a 5-mm-diameter opening has a maximum divergence of $\alpha \approx 45°$ and a maximum transverse energy of about 10 eV. Whether such a beam can be injected into a linear trap without losses depends on the acceptance of the system. The latter is determined by the transverse dimensions and the transverse focusing force inside the trap.

For the ion beam buncher discussed here, a number of injection calculations have been performed in order to determine the acceptance of the system. As an example, Fig. 3.7 shows a comparison of the transverse acceptance of the ISOLTRAP ion beam buncher and the transverse emittance of the ISOLDE ion beam, both at beam energies of 30 keV. The diagrams are calculated at a position 140 mm upstream from the 6-mm hole of the retardation electrode (see Sect. 3.3.1).

The emittance diagram in Fig. 3.7 a was obtained from beam transport calculations

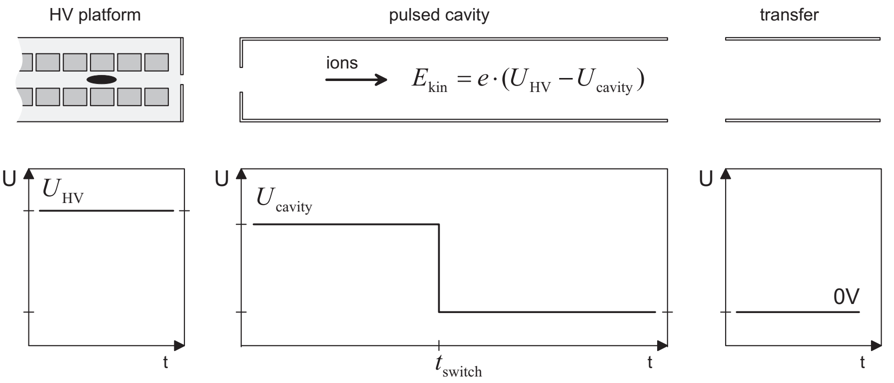

Figure 3.8: Principle of creating variable energy ion pulses by employing a pulsed cavity

(GIOSP [Wol87]) of the ISOLDE beam from the ion source to the apparatus. For the acceptance diagram, a Monte-Carlo simulation for the ion injection into the buncher was performed modeling the interaction of the ions with the buffer gas atoms by hard ball collisions (for the RFQ parameters see Table 3.2). The hard ball collision model for $^{133}\text{Cs}^+$ ions cooled in helium is in excellent agreement with the more realistic interaction potentials described in [Sch99]. An ion was considered to be confined when it passed the first 200 mm of the quadrupole rod system without hitting an electrode. The calculation was repeated for various phases of the radio-frequency field. For each x and α value an average of the result was taken including the beam dimensions y and β. The result is the acceptance diagram shown in Fig. 3.7 b. From this acceptance and the ISOLDE beam emittance a value of $\epsilon_{\text{calc}} \approx 35\,\%$ is obtained for the theoretical capture efficiency.

Extraction and acceleration

When the ions have been accumulated in the trap potential minimum, they can be extracted by switching the potential as indicated in Fig. 3.1. With appropriate voltages applied to the electrodes, ion pulses not longer than a few microseconds can be generated. The beam properties of the extracted ion pulses depend on the temperature and spatial distribution of the ion cloud. The time structure depends in addition on the shape of the potential used to extract the ions. If no further measures are taken, the ion pulse leaving the trap at the potential of the HV platform will be accelerated towards ground potential and once again reach the energy of the injected ion beam minus a few ten electron volts that they lost in the buffer gas. For the transfer into the ISOLTRAP Penning traps, low-energy ($\approx 2.5\,\text{keV}$) ion pulses are required.

An elegant way to modify the potential energy of an ion pulse is to have the ions enter a pulsed cavity. The principle is illustrated in Fig. 3.8. After having left the linear ion trap at a potential U_{HV} the ion pulse is accelerated towards a cavity at a potential U_{cavity} to gain a kinetic energy $E_{\text{kin}} = e \cdot (U_{\text{HV}} - U_{\text{cavity}})$. When the ion pulse reaches the field-free region inside the cavity, the latter is switched to ground potential and the ions leave it without any further change of their kinetic energy since they will feel no field gradient when they exit the cavity.

3.3 The experimental setup

Figure 3.9 shows the setup of the ISOLTRAP ion beam cooler and buncher. On one side the system is connected to the ISOLDE beam line and on the other side to the ion beam transport system of ISOLTRAP. A 60-keV test ion source and a beam switchyard (not shown in the figure - see App. A.3) are installed upstream in order to allow test measurements without the ISOLDE ion beam. Beam intensities and profiles can be measured with a needle beam scanner and a Faraday cup in front of the ion beam buncher. Most of the relevant parts of the cooler and buncher, including the electronics and the gas inlet system, are placed on a 60-kV high-voltage platform in a high-voltage cage. Ceramic insulators separate the vacuum system on the HV platform from the beam lines on ground potential. Efficient pumping is achieved by turbo-molecular pumps at ground potential placed close to the insulators.

The ion-optical elements of the cooler and buncher can be grouped into three functional sections. In the first section the deceleration of the ISOLDE ion beam takes place, the second section is the linear ion trap, and in the third section the extracted ion bunches are accelerated to the desired transport energy. All electrodes are made of stainless steel. Alumina or glass ceramic (Macor®) are used for insulating parts. The electrical connections to the ion-optical elements are made via UHV multi-pin feedthroughs and Kapton®-insulated wires. Table 3.1 summarizes some important mechanical parameters of the system which will be discussed below in more detail.

Table 3.1: Dimensions of the ISOLTRAP ion beam buncher

Element	Dimension [mm]
diameter of injection hole	6
diameter of extraction hole	6
distance between opposite rods ($2 \cdot r_0$)	12
diameter of rod segments	18
total length of quadrupole rods	881.5
length of rod segments	
# 1, 2	20.5
# 3 – 19	41.5
# 20	20.5
# 21	41.5
# 22 – 25	10.0
# 26	20.5
length of pulsed cavity	380

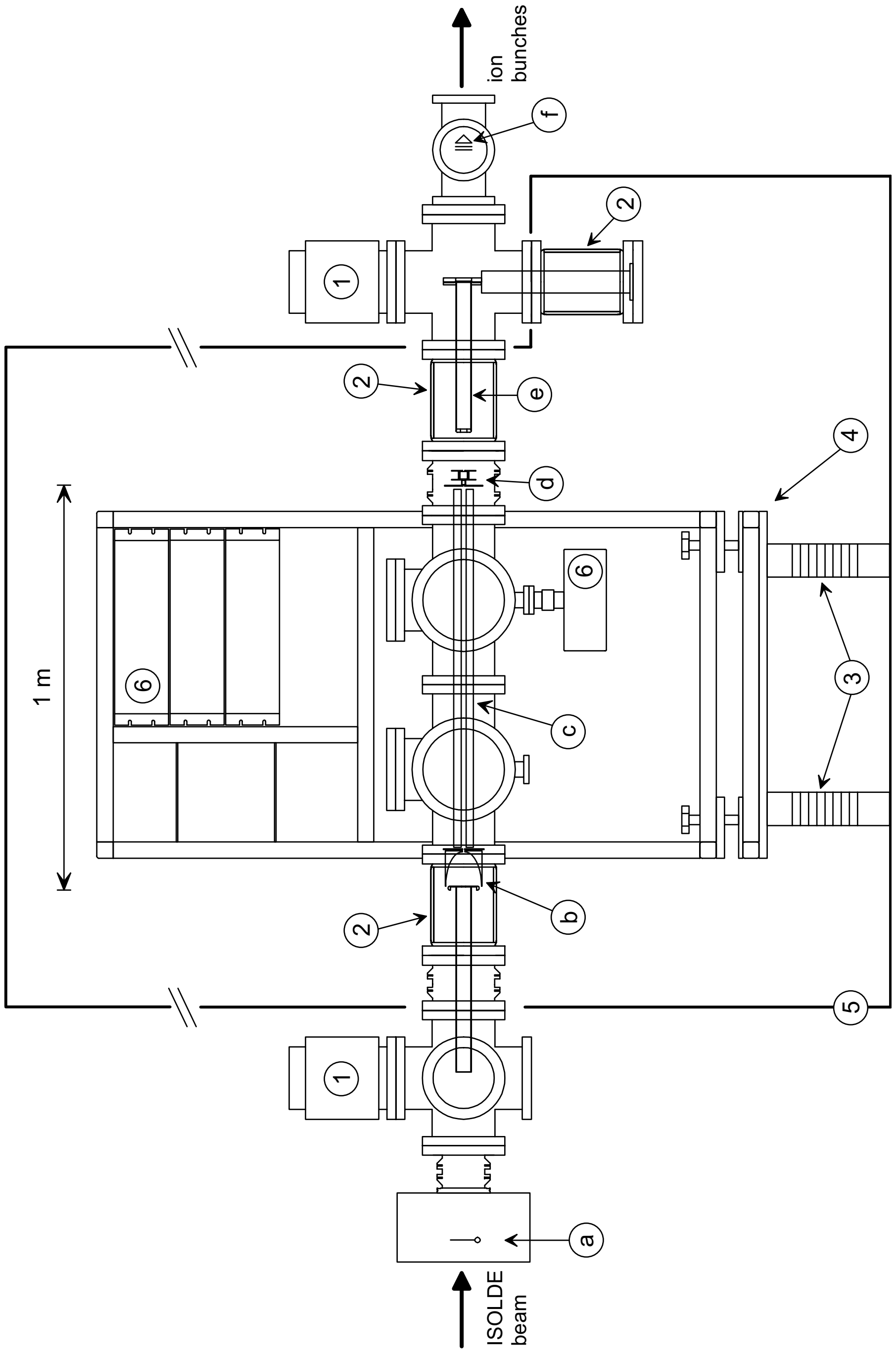

Figure 3.9: Experimental setup of the ISOLTRAP ion beam cooler and buncher. The main components are: (1) turbo-molecular pump, (2) insulator, (3) insulating support, (4) HV platform, (5) grounded cage, (6) DC and RF supplies, (a) beam scanner and Faraday cup, (b) deceleration section, (c) linear ion trap, (d) extraction section, (e) pulsed cavity, (f) MCP detector.

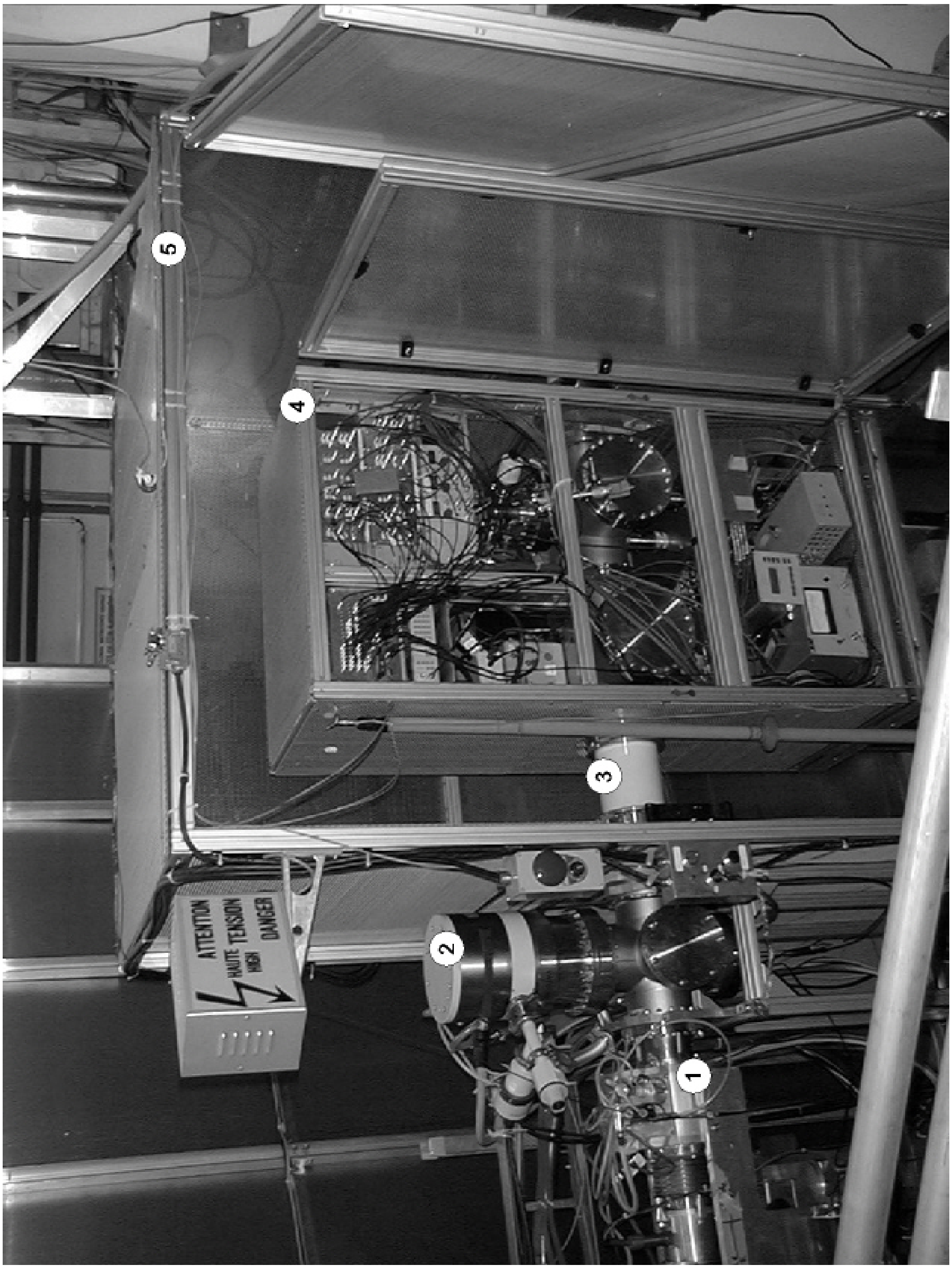

Figure 3.10: Photograph of the experimental setup of the ISOLTRAP ion beam cooler and buncher. Visible are: 1) the ISOLDE beam line with beam scanner; 2) a turbo-molecular pump; 3) a Ceramic insulator; 4) the inner cage housing the electronics and vacuum parts that reside on the HV; 5) the Outer cage that is grounded.

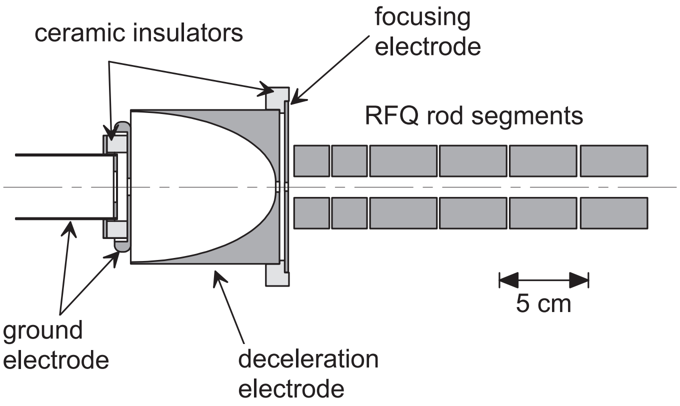

Figure 3.11: Ion optical elements for the deceleration of the 60 keV ion beam and first part of the linear ion trap.

3.3.1 The deceleration and injection section

Figure 3.11 shows the design of the deceleration electrode system and its connection to the linear ion trap system discussed below. This deceleration electrode system is the copy of a prototype described in more detail in [Kel00]. The ISOLDE ion beam enters through the ground electrode which is equipped with an insulated diaphragm for current measurements. The shape of the deceleration electrode is designed to focus the beam through the 6-mm opening at its end. An additional electrode and the first segments of the four-rod structure are used to obtain the final retardation and to focus the beam towards the axis of the system.

For the presented cooler and buncher ion optical simulations were performed so as to determine the optimal position of the ground electrode with respect to the deceleration electrode and to get a set of voltages that give the best injection efficiency into the trap system. These voltages were used as start values for the experimental optimization. A set of typical voltages for the deceleration section are listed in Tab. 3.2 below together with parameters for the other sections.

3.3.2 The linear ion trap

Figure 3.12 shows a photograph of the assembled electrode system of the linear ion trap with the deceleration electrode mounted. Figure 3.13 shows a detailed view of a part of a rod and how the cylindrical electrode segments are mounted together. The quadrupole rods have a total length of 881.5 mm. Each rod consists of 26 segments. All electrodes have a diameter of 18 mm. They are aligned by four inner support rods with ceramic insulators in-between, separating the electrodes by 0.5 mm axially. The quadrupole rods themselves are mounted via ceramic supports to four mounting disks as shown in the right part of the Fig. 3.13. The inner distance between opposite quadrupole rods is $2r_0 = 12\,\text{mm}$. The holding disks are kept at fixed distances by the four outer support rods. Additional ceramic

Figure 3.12: Photograph of the assembled four-rod electrode system of the ISOLTRAP ion beam cooler and buncher and the mounted deceleration electrode.

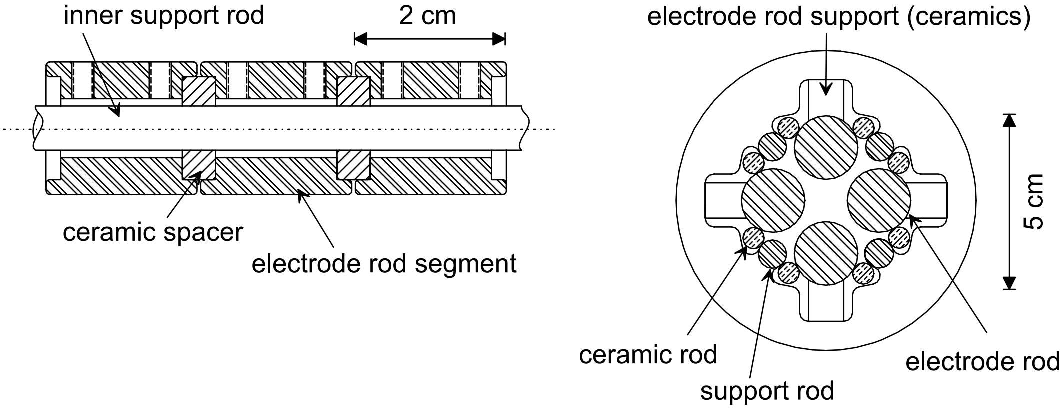

Figure 3.13: Detail of the rod structure. The segments are insulated from each other by ceramic spacers. The four rods are mounted to disks as shown in the right part.

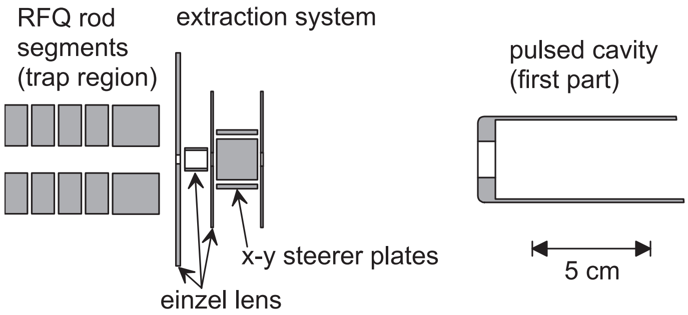

Figure 3.14: Exit side of the linear trap with extraction lens, x-y steerers and a pulsed cavity

rods are provided to “seal” the system. This is to maximize the gas pressure inside the trap while minimizing the pumping requirements of the whole system. Electrode segments of various lengths are used (see Tab. 3.1). The shorter segments at the entrance of the trap allow to set up an axial potential gradient for retardation and focusing of the incoming ions as discussed above. In the part of the trap where the potential decreases slowly and linearly, longer segments are sufficient. A high segmentation is again required in the region where the ions are finally accumulated and ejected.

3.3.3 The extraction section and the pulsed cavity

Figure 3.14 shows the extraction optics of the buncher and the pulsed cavity. The extraction hole has a diameter of 6 mm. The extraction optics consists of an einzel lens formed by a cylindrical electrode between two diaphragms and a set of x-y steerers. The purpose of this arrangement is to adapt the divergence of the extracted ion bunch to the ion optics downstream and to allow adjustments of the ion-flight direction.

At a distance of 90 mm downstream from the extraction optics, the ions enter the pulsed cavity, which is only partly shown in the figure. The cavity is designed to shield the ion pulse from external fields and has a total length of 380 mm. This is larger than the expected length of a pulse of ions with mass number $A > 20$ that is injected into the cavity with an kinetic energy of 2 to 3 keV. In Fig. 3.9 it can be seen that the pulsed cavity is fixed to a support directly mounted on an insulated flange perpendicular to the beam axis.

3.3.4 Vacuum system and gas supply

Figure 3.15 gives a schematic overview of the vacuum and gas inlet system. The vacuum system that houses the ion-optical parts discussed above consists of several vacuum chambers mostly of CF 150 size. Two magnetic-bearing turbo-molecular pumps (Pfeiffer TMU 1000MC) with a pumping speed of 870 l/s for helium are connected on both sides of the system. These pumps are backed by one 40 m^3/h roughing pump. Differential pumping is

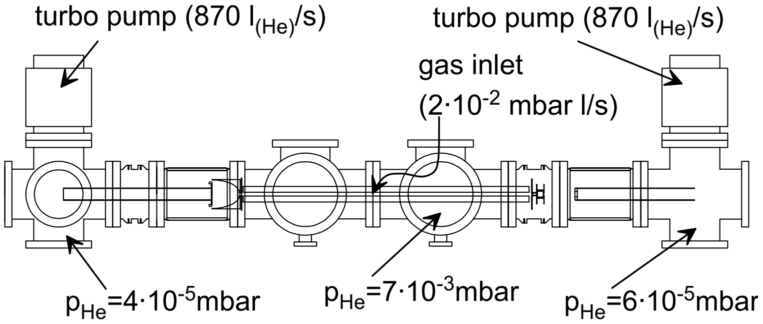

Figure 3.15: Schematic of the vacuum system of the ISOLTRAP ion beam cooler and buncher. Gas flow value (valve controller reading), pumping speeds (for He), and measured pressures values (He-corrected) are shown.

accomplished by diaphragms at the entrance and exit side in order to reduce the gas flow out of the trapping region. The trap is mainly pumped via the entrance and exit holes for the ions. The buffer-gas inlet is via a needle valve connected to a pressure controller (Balzers EVR 116 + RVC 200). Inside the vacuum chamber, a thin stainless steel tube guides the gas into the central region of the RFQ structure. A full-range pressure gauge (Balzers PKR 250) is connected to the vacuum chamber on the HV platform. Its reading is used as the input for the pressure controller. The pressure value measured with the gauge is of course lower than the pressure inside the structure. From gas flow simulations, it is expected that the gauge gives a reading which is about a factor of 10 lower than the actual pressure inside the center of the structure[1].

A reasonable working pressure inside the RF-structure is $p_{\mathrm{He}} \approx 10^{-2}\,\mathrm{mbar}$. With the resulting gas load, care has to be taken about possible discharge processes in the system. A critical point is the region where the ground injection electrode is close to the deceleration electrode (Fig. 3.11) with a gap of 5 mm and a potential difference of up to 60 kV. One has to make sure that at this gap a pressure regime is reached where the discharge probability is minimized. The Paschen curve [Mee53] for helium gives a maximum pressure of the order of 10^{-5} mbar. Gas flow calculations have confirmed that such values can be reached with the applied pumping speed, the entrance and exit openings of the linear trap, the desired inside pressure, and the required gas flow. The experimentally measured pressures are given in Fig. 3.15.

Another point of concern are gas impurities in the system which can give rise to charge exchange and loss of ions. Such effects have been seen in the start-up of the system when ions like argon were injected into the ion beam cooler and buncher. Meanwhile, this has been cured by baking the whole system. Furthermore, pellets of non-evaporable getter material (SAES St 172 type) have been installed in the gas inlet line of the buncher for gas purification.

---

[1] In this work, the values given for the measured pressure are the vacuum gauge readings corrected for the gas-specific factor.

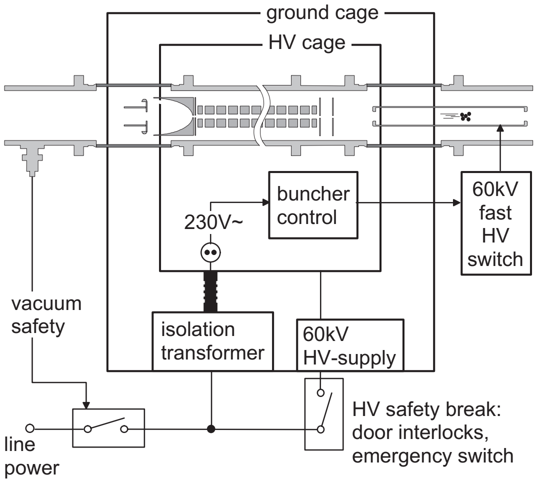

Figure 3.16: Line power and HV supply for the high-voltage platform. Also shown are the safety interlocks that cut the high voltage in the event of too high pressure and allow safe access to the cage.

3.3.5 Electronics and control system

The high-voltage system

Figure 3.16 shows schematically the high-voltage and the line power supply for the high-voltage platform. An oil-free 2-kW isolation transformer is used to provide line power to the platform. The platform potential is provided by a remote-controllable power supply (FUG HCN 140M-65000) with a maximum voltage of 65 kV and a short- and long-term voltage stability of 10^{-5}. This power supply is connected to the secondary windings of the transformer via a 5.6-kΩ current-limiting resistor. Varistors across the secondary winding of the isolation transformer protect the electronic equipment on the high-voltage platform from high-voltage transients caused by occasional sparkovers.

Figure 3.17 shows the circuit used for the switching of the potential of the cavity. A fast high-voltage transistor switch (Behlke HTS 650) discharges the cavity with a fall-time $t_\mathrm{f} = 220\,\mathrm{ns}$. After a constant on-time of $60\,\mu\mathrm{s}$ the switch opens again, allowing the cavity to be charged again to high voltage with a rise-time $t_\mathrm{r} = 22\,\mathrm{ms}$.

Radio-frequency and DC supplies for the buncher

The RF voltage for the radial pseudopotential has to be applied to all segments of the system but with a phase shift of 180° between segments of neighboring rods. The DC potentials are applied in two different modes, depending on whether the element is used for a static potential or whether the potential is dynamically switched within less than one microsecond.

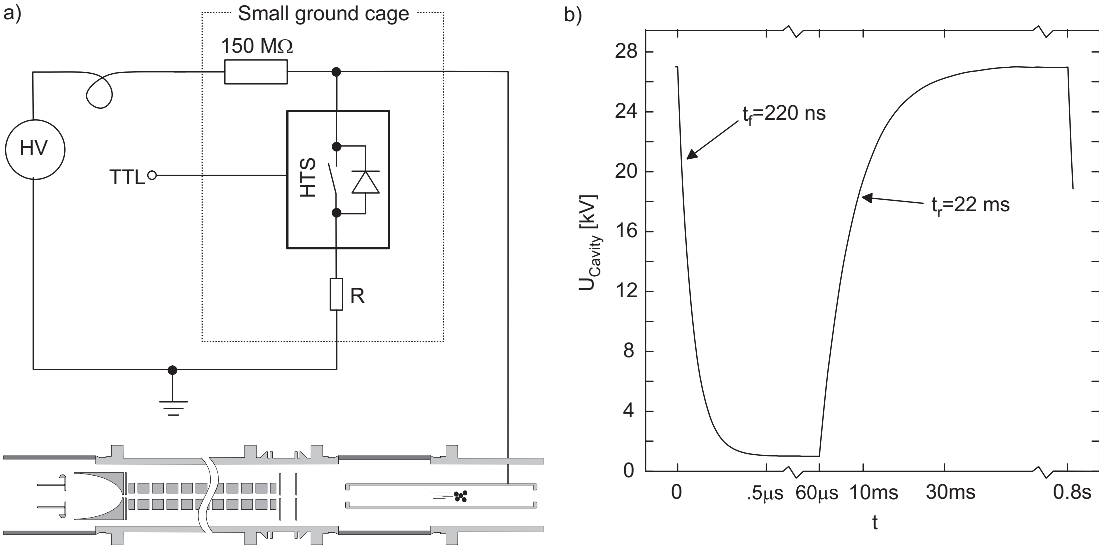

Figure 3.17: Circuit used for the fast switching of the pulsed cavity from a potential of ≤60 kV to ground potential (a). Measured voltage for a switching from ≈30 keV to ground as a function of time (b). HV: high-voltage power supply; HTS: high-voltage transistor switch; R: current limiting resistor ($I_{\mathrm{max}} = 30\,\mathrm{A}$). The times t_{f} (fall-time) and t_{r} (rise-time) are the times needed for the signal to change between 10 and 90% of its maximum strength.

Two different types of circuits are used. The circuit shown in Fig. 3.18 a is used for all elements where a static DC voltage is required. The RF voltage $U_{\mathrm{RF,in}}$ is provided by a function generator (Stanford Research DS 345) after amplification by a 200-W radio-frequency amplifier (ENI 240L) and fed into a transformer. The secondary winding has a grounded center tap in order to generate two symmetrical radio-frequency signals $U_{\mathrm{RF}\pm}$ of opposite sign. These RF voltages are added via capacitors $C = 10\,\mathrm{nF}$ to the DC voltages $U_{\mathrm{DC},i}$ ($i = 1 \ldots k$) in order to obtain a combined RF/DC signal which is applied to the different pairs of electrodes $S_{i\pm}$ ($i = 1 \ldots k$). Two inductances $L_{\mathrm{b}} = 3.9\,\mathrm{mH}$ protect each DC feeding point from the two RF signals. The DC voltages are provided by 0 to 500-V power supply modules (Brandenburg). The voltage series required for the generation of the linear potential slope (see Fig. 3.1) is obtained via a resistive voltage divider chain fed by two of the DC power supply modules. The most critical electrodes closest to the injection side of the buncher and those in the trapping region have separate voltage supplies. The inductance of the transformer and the capacitances have been matched to the capacitance of the electrodes in order to obtain a maximum RF voltage at a frequency of $\nu \approx 1\,\mathrm{MHz}$. An amplitude $U_{\mathrm{RF}} \approx 125\,\mathrm{V}$ is reached with about 40 W RF power.

For the extraction of the ions from the buncher it is necessary to switch the potential of the last segments of the linear trap very quickly. Therefore, the relevant segments are supplied with a circuit as shown in Fig. 3.18 b. The DC voltage from the DC modules is sent to the center tap of the transformer via a fast transistor switch. With this system, a fall-time of 0.5 μs is obtained.

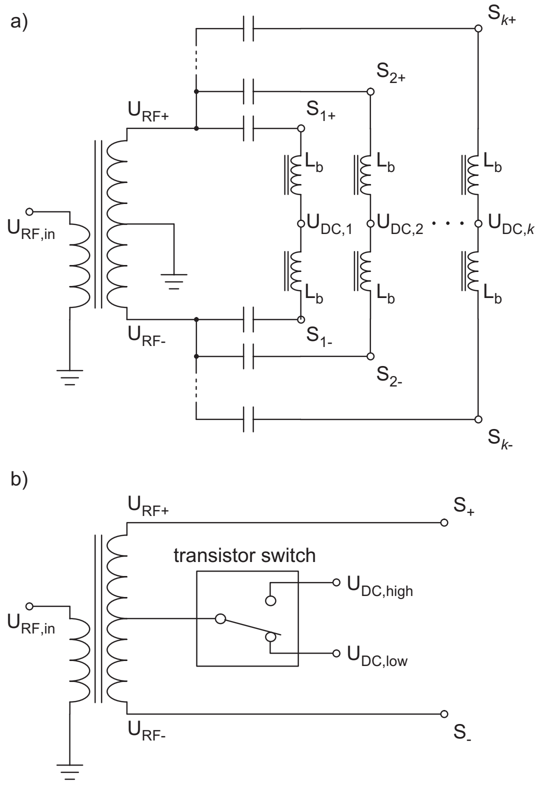

Figure 3.18: Principle of the electronic circuits used to provide the different segments $S_{k\pm}$ of the four rods with DC ($U_{\mathrm{DC},k}$) and RF ($U_{\mathrm{RF}\pm}$) voltages. a) circuit for those electrodes which require RF and static DC voltages; b) circuit for those electrodes which require RF and switched DC voltages.

A number of additional power supplies is used for the voltages of the deceleration and focusing electrode (see Fig. 3.11) and the extraction optics (see Fig. 3.14). The high voltage U_{cavity} for the pulsed cavity (see Fig. 3.17) is also provided from the HV platform.

The control system

Figure 3.19 shows the layout of those parts of the control system relevant for the operation of the cooler and buncher. Since most of the electronics is installed on the HV platform, remote control of the system is mandatory. Three different optical links provide the communication between the VME-based computer system of the ISOLTRAP spectrometer and the electronics on the HV-platform. A GPIB link (National Instruments GPIB-140) is used to control the function generator for the radio-frequency signal and to read out a pico-amperemeter. A field bus system (Profibus) equipped with DACs and ADCs is used for analog programming and monitoring a total of 28 voltage supplies. It also serves for programming the pressure regulation system. A fast TTL link (Harting) is used to provide the trigger for the fast voltage switching required for the ion extraction from the buncher.

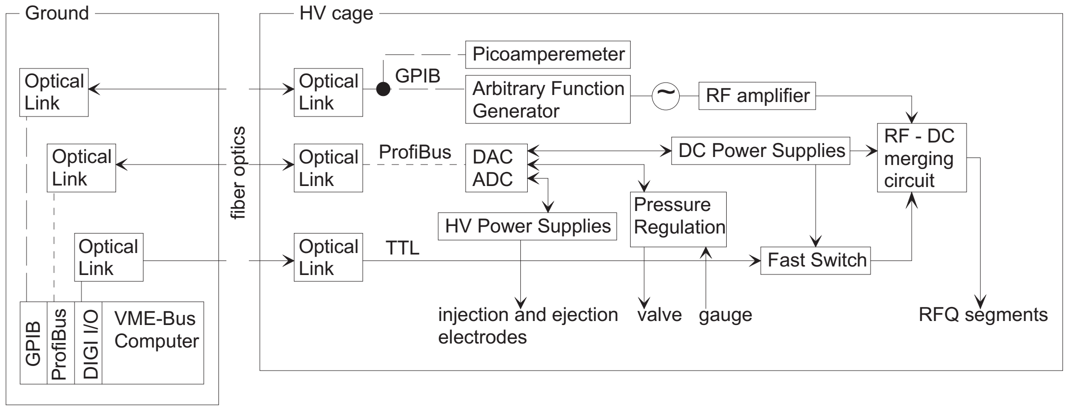

Figure 3.19: Layout of the control system of the ISOLTRAP buncher. The electronics on the HV platform is controlled via three optical links.

3.3.6 Diagnostics

Several tools are available for the optimization and diagnosis of the performance of the ion beam cooler and buncher. The ISOLDE beam scanner and movable Faraday-cup in front of the buncher allow the measurement of profile and current of beams from both ISOLDE and the test ion source. In order to optimize the injection of the 60-keV ion beam into the buncher, it is important to perform a beam current measurement on the high-voltage platform. For this purpose a picoamperemeter (Keithley 485) is installed on the platform which can be connected to any of the buncher electrodes. On the ejection side another Faraday cup and a micro-channel plate (MCP) detector are available. This detector consists of 2 MCP's with 18 mm active area mounted in a Chevron arrangement. No electron repelling grid is used (see discussion in 3.4.2). This MCP detector has been used for most of the test measurements reported. It has been used in single ion detection mode, i.e. the signal created by a single ion is transformed to a standard electronic signal and fed into a multi channel scaler. This detection scheme limits the number of ions that can be reliable detected to about 10 ions per micro second, determined by the response function of the multi-channel plate detector and the following electronics to a single ion. More MCP detectors are available further downstream for the tuning of the ion beam transport to the Penning trap system. In addition, a beam viewing system is available which can be installed behind the 90° vertical deflector (see fig. 2.3) to obtain the spatial distribution of the ion beam. This system (Colutron BVS-2), which is mounted on a flange with a viewport, consists of an MCP with a phosphor screen behind it. The fluorescent light from the phosphor screen originated by the secondary electrons of the MCP after ion impact, can be viewed through this window with a CCD camera. When this detector is used the deflector electrode system is removed from its vacuum chamber in order to allow the ions to pass through.

3.4 Performance of the ISOLTRAP cooler and buncher

A number of systematic investigations have been performed with the buncher in order to characterize its performance and to compare the results with simulations. For these measurements, ions both from ISOLDE and from the test ion source have been used.

3.4.0 Operation

Table 3.2 gives a typical set of operating parameters for ions with mass number close to $A = 39$ and $A = 133$. The ions enter the linear trap with an energy of 20 eV after retardation. The value given for the buffer gas pressure value is the (helium-corrected) vacuum gauge reading. As discussed above the pressure inside the linear trap is estimated to be a factor of 10 higher. Depending on the delivered ion beam current, the ions are accumulated for a period $T_{\text{accu}} = 0.01 \ldots 1000\,\text{ms}$. In order to avoid saturation effects in the read-out electronics of the MCP detector the time was chosen such that the ejected pulses did not contain more than 20 ions during all test measurements performed on the first MCP detector after the ion beam cooler and buncher. For mass measurements this number was increased by two to three orders of magnitude. The ions are allowed to complete their cooling into the trap potential minimum for an additional period $T_{\text{cool}} = 2\,\text{ms}$ before they are ejected. The timing of the switching of the cavity is adapted to the mass-dependent time of flight of the ions. For a 2.65-keV extraction and an $A = 40$ ion, $t_{\text{switch}} = 12\,\mu\text{s}$. The system has been tested with repetition rates up to 5 Hz. In general, repetition rates of about 1 Hz are used for the mass measurements.

3.4.1 Injection, capture, and ejection

Ion energy

A critical parameter for the injection and capture of the ions into the buncher is the energy of the ions when they enter the system. This energy is determined by the potential of the linear trap on the HV platform with respect to the initial ion beam energy. If the potential is too high, then the ions are not able to enter the system. If it is too low, then the energy loss in the gas is not sufficient to prevent the ions from leaving the system on the exit side or to be stopped before the extraction diaphragm.

In order to optimize the injection and the platform potential, two kinds of measurements are performed. In the first case, all electrodes of the extraction system (see Fig. 3.14) are connected together for a direct current measurement. Radio-frequency and DC potentials are applied to the segmented rods as given in Tab. 3.2 for the ejection mode. No buffer gas is used.

In Fig. 3.20 (top) the result of such a measurement is shown for a 30-keV $^{132}\text{Xe}^+$-ion beam as a function of the potential of the HV platform. At the ion beam energy of 30 keV maximum transmission is observed. Increasing the potential from 30 000 V to 30 030 V gives a sharp drop in transmission. At a potential larger than 30 030 V no ions

Table 3.2: Typical operating parameters of the cooler and buncher for ions in the mass ranges $A \approx 39$ and $A \approx 133$.

Parameter		Value		
helium pressure (at gauge position) p_{He}		$6 \cdot 10^{-3}$		mbar
RF frequency $\nu_{\text{RF}} = \omega_{\text{RF}}/2\pi$		970		kHz
RF amplitude U_{RF}	for $A \approx 133$	135		V
	for $A \approx 39$	97		V
cooling time T_{cool}	for $A \approx 133$	10		ms
	for $A \approx 39$	2		ms
cage voltage U_{HV}		30 000	60 000	V
electrode voltages U_{elec} relative to the cage voltage U_{HV}:				
deceleration electrode		–1 350	–3 000	V
focusing electrode		–230	–180	V
quadrupole rod segment	# 1	–60		V
	# 2	–40		V
	# 3	–25		V
	# 4 to #22	–10 to –20		V
	# 23 (accumulation)	–24		V
	# 23 (ejection)	+2		V
	# 24, # 25	–29		V
	# 26 (accumulation)	0		V
	# 26 (ejection)	–55		V
plates of the extraction system		–420		V
einzel lens		–55		V
pulsed cavity		–2 650		V

are transmitted. For potentials lower than 30 kV and correspondingly higher ion beam energy in the system, the transmission decreases gradually. This can be understood since the focusing of the ion optics in the injection part was optimized for a beam entering the cooler and buncher at about 20 eV kinetic energy.

This transmission mode of operation is particularly useful for a fast tuning of the beam injection into the cooler and buncher. The platform potential is set to the value giving maximum transmission and then the current at the end of the structure is monitored as a function of focusing and steering voltages applied to ion optical elements in the ISOLDE beam line.

For fine tuning of the injection (in particular the platform potential), the full accumulation-ejection cycle has to be employed. The result of such a measurement (performed with a buffer gas pressure of $p_{\text{He}} = 1 \cdot 10^{-2}$ mbar) is shown in the bottom part of Fig. 3.20. Plotted as a function of the platform voltage are the average number of $^{132}\text{Xe}^{+}$ ions per cycle extracted from the buncher and detected by the MCP detector. It should be noted that the optimum value for the platform potential has shifted by about 25 eV, which means

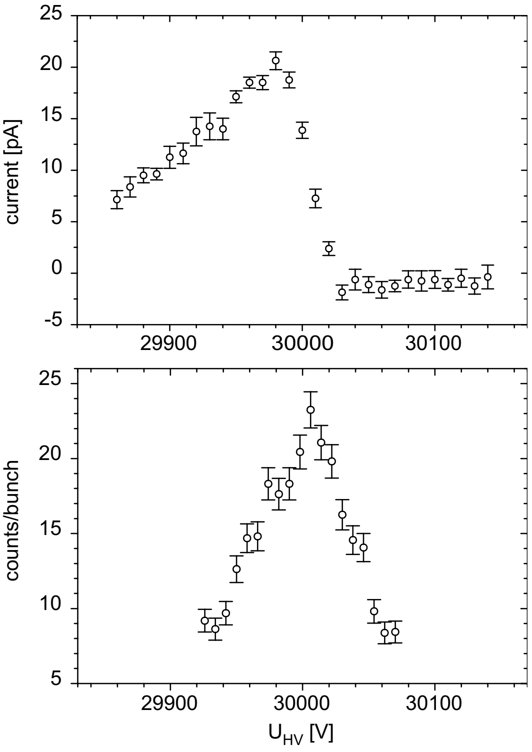

Figure 3.20: Current of ^{132}Xe^{+} ions guided through the RFQ (top) and number of accumulated and ejected ions per bunch in bunching mode (bottom) as a function of the voltage U_{HV} of the HV platform.

that a maximum capture efficiency requires an injection of the ions at an energy slightly lower than that for best transmission.

Similiar test have been performed for a cage voltage U_{HV} around 60 kV. As expected, the results are comparable to the measurements described here.

Radio-frequency parameters

Both, the amplitude and the frequency of the RF potential should have an effect on the ion transmission through the linear trap and on the storage of the ions. Due to technical reasons, the frequency of the RF circuit used in this work was fixed to $\nu_{\mathrm{RF}} \approx 1\,\mathrm{MHz}$. Therefore, only measurements on the effect of a change of the RF amplitude were performed. The result of such a measurement is shown in Fig. 3.21. The upper part shows an injection and transmission measurement similar to those described above. The ion current at the end of the structure is plotted as a function of the amplitude U_{RF} of the applied radio-frequency. As expected, the transmission steadily increases with increasing amplitude (and deeper radial pseudopotential). Above $U_{\mathrm{RF}} \approx 120\,\mathrm{V}$, the transmitted current saturates. The lower figure shows the result of a measurement where the Xe ions are

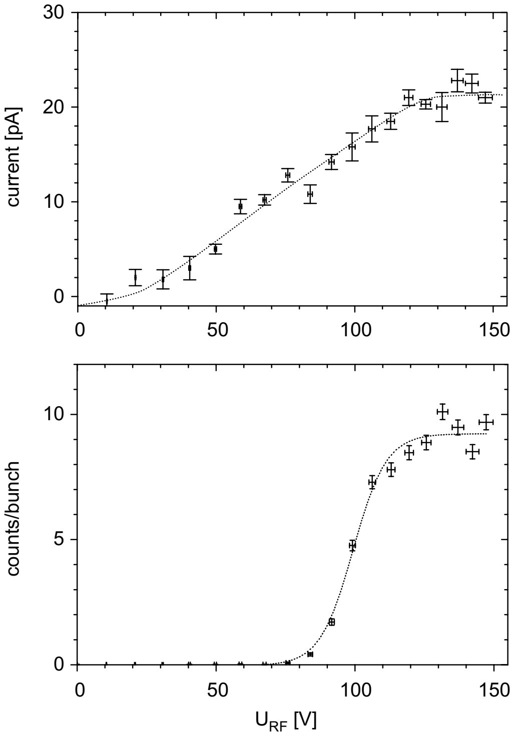

Figure 3.21: Transmission of $^{132}Xe^{+}$ through the cooler and buncher (top) and number of accumulated and ejected ions (bottom) as a function of the radio-frequency amplitude U_{RF}. The lines shown serve to guide the eye.

accumulated, cooled ($p_{\mathrm{He}} = 1 \cdot 10^{-2}$ mbar) and ejected. Shown is the number of detected ions as a function of U_{RF}. It can be seen that a certain threshold amplitude of $U_{\mathrm{RF}} \approx 75$ V is required in order to obtain ions from the trap. The reason is that for too low RF amplitudes, the defocusing radial part of the DC potential at the axial potential minimum of the trap is stronger than the generated pseudopotential, as explained in section 3.1. The ions are transmitted to the "trapping" region where they are finally lost radially. Using (3.6) and the actual trap parameters, one obtains a threshold amplitude of $U_{\mathrm{RF,min}} \approx 60$ V which is in good agreement with the experimentally observed value.

Buffer gas pressure

The accumulation of the ions in the linear ion trap requires sufficient energy dissipation in the buffer gas (see Fig. 3.4) and hence a high enough pressure. If the pressure is too low, then most of the ions will hit the exit electrode of the linear ion trap and are lost. Figure 3.22 shows the number of ions ejected from the trap for constant injection conditions as a function of the gas pressure. It can be seen that a He pressure of a few 10^{-3} mbar is required in order to observe any ions. Above $p_{\mathrm{He}} \approx 10^{-2}$ mbar the number that can be extracted starts to saturate.

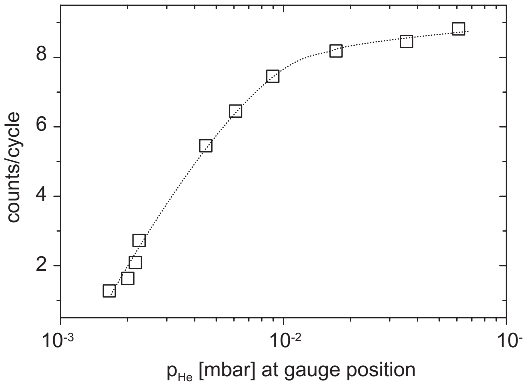

Figure 3.22: Number of accumulated and ejected $^{208}\mathrm{Pb}^+$ ions as a function of the buffer gas pressure p_{He}. The value is the (He-corrected) reading of the gauge at the vacuum chamber containing the linear ion trap. The line shown serves to guide the eye.

3.4.2 Efficiency

After finding good parameters for the operation of the cooler and buncher the efficiency of the system was determined. From a current measurement as shown in Fig. 3.20 (top) and a comparison with the beam current measured with the Faraday cup in front of the system, its injection and guiding efficiency $\epsilon_{\mathrm{trans}}$ was determined. Such measurements have been carried out with ISOLDE beams from various ion sources. Values for the transmission $\epsilon_{\mathrm{trans}}^{\mathrm{exp}}$ between 20% and 40% were found. This is in good agreement with the theoretical value of $\epsilon_{\mathrm{trans}}^{\mathrm{theo}} \approx 35\,\%$ (see chapter 3.2.4).

Most interesting is the total efficiency $\epsilon_{\mathrm{total}}$ of the cooler and buncher which is defined as the ratio of the number of ions injected into the system and the number of ions finally counted in the extracted ion pulse. The measurements are performed in the following way: a weak ISOLDE beam, but still intense enough to perform a reliable current measurement (typically a few pA), is transported to the apparatus. For the injection into the buncher, a very short opening time for the ISOLDE beam gate is used in order to inject a well defined small number of ions N_{ion} into the buncher. These ions are accumulated, cooled, ejected, and finally detected with the multi-channel plate detector. As mentioned above, this detector, which is normally only used for simple monitoring purposes, is not equipped with an electron repelling grid. Therefore, according to [Bre95], only about half of the maximum possible efficiency of $\approx 50\ \%$ is achieved in the case of moderately heavy ions with 2.5 keV energy. With the number of counted events being N_{MCP} and an efficiency $\epsilon_{\mathrm{MCP}} \approx 30\,\%$, the overall efficiency is given by $\epsilon_{\mathrm{total}} = (N_{\mathrm{MCP}}/\epsilon_{\mathrm{MCP}})/N_{\mathrm{ion}}$.

Total efficiency measurements have been performed for various Xe isotopes and values of $\epsilon_{\mathrm{total}} \approx 12\ldots15\,\%$ were achieved. This value allows to study ions from the weakest radioactive beams available at ISOLDE with the ISOLTRAP spectrometer. However, compared to the efficiency $\epsilon_{\mathrm{trans}}$ for injection and transmission, the total efficiency $\epsilon_{\mathrm{total}}$ is lower by a factor of two to three. Storage time measurements for alkali ions have shown lifetimes of up to several 100 ms. For Xe ions as used for the efficiency measurement, no significant charge exchange with gas impurities has been observed, which could have caused ion loss. A possible explanation is that the MCP efficiency is lower than assumed. It is also likely that an optimal match of ISOLDE beam emittance and buncher acceptance has not yet been achieved.

Another possible explanation is connected with the highly asymmetric potential in the region of the linear ion trap (see Fig. 3.2). Even if the storage condition (3.6) is fulfilled in the close proximity of the trap center it can be broken in the region of the steep potential gradient towards the exit of the cooler and buncher. The potential gradient U_{DC}/z_0^2 determines the radial strength of the DC potential that counteracts the radially confining RF potential. Therefore, ions that arrive in this region with too high kinetic energy will not be trapped. The ion energy at injection into the cooler and buncher has to be chosen to meet this criterion regardless whether this thwarts the optimal injection into the rod system itself. This could explain why the optimum value for the platform potential is about 25 eV higher for the trapping mode than for the transmission mode. This will be investigated in forthcoming test measurements accompanied by further beam injection simulations.

3.4.3 Cooling and beam emittance

Damping of ion motion and cooling

In order to illustrate the damping of the axial ion motion in the cooler and buncher for different ions and types of buffer gas, very short ion pulses have been injected. The DC potential of the cooler was permanently set to the extraction mode, which means that the ions were directly accelerated to the MCP detector after a single passage through the system.

The result of such a measurement for various ion species and gases is shown in Fig. 3.23. With buffer gas of higher mass, the ion pulses arrive considerably later and are broadened. This can be understood by looking at the microscopic beam simulations shown in Fig. 3.5. There the trajectories of for instance K ions in Ar show a significant scattering that delays the transport through the system. In the experiment the transmission of $^{39}\mathrm{K}^+$ ions through $^{84}\mathrm{Kr}$ was also tried, but, as expected no ion was able to reach the detector.

An illustration of the transverse cooling process as a function of time is given in Fig. 3.24. In the experiment, $^{133}\mathrm{Cs}^+$ ions were injected into the linear trap for a short period $T_{\mathrm{accu}} = 2\mu\mathrm{s}$. The figure shows the number of ions ejected out of the trap as a function of the cooling time T_{cool} after injection. This measurement was performed for helium and argon as buffer gases at about the same pressure. For short cooling times, the number of ions that can be extracted is small and only above $T_{\mathrm{cool}} > 300\mu\mathrm{s}$ is the maximum number reached. This is because at the pressure of $p_{\mathrm{He}} \approx 3 \cdot 10^{-3}$ mbar used here several oscillations are required inside the trap before the radial extent of the ion cloud is smaller than the radius of the extraction hole. The figure also illustrates that stronger damping and, as a consequence, faster cooling are provided by the heavier buffer gas.

Figure 3.25 illustrates once more the axial cooling process. In the top figure the temporal

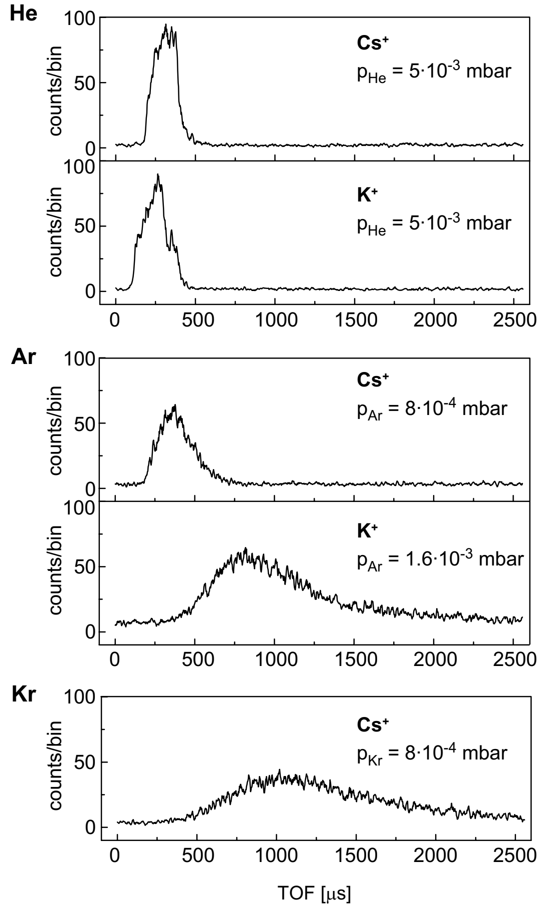

Figure 3.23: Time structure of pulses of different ions after passage through the RFQ system for different buffer gases. Here, the ion trap was operated as an ion guide. Plotted is the number of detected ions per bin, each bin being 2.56 μs wide.

width of the ejected ion pulse is shown as a function of the cooling time for the case of $^{39}K^{+}$ ions and $p_{\mathrm{He}} = 2.5 \cdot 10^{-3}$ mbar. As can be seen in the figure, an exponential decrease of the pulse width with time is observed. The pulse width decreases with decreasing ion temperature and smaller axial distribution of the ions in the trap. The width is therefore a good indicator of the ion temperature. The time constant τ_{cool} of the curve can to first order be regarded as a measure of the cooling time constant. The value of $\tau_{\mathrm{cool}} = 0.5$ ms obtained in the measurement shown in Fig. 3.25 is comparable to a value of 0.3 ms calculated from ion mobility data and an estimate of the pressure inside the buncher close to the trapping region of $p \approx 10^{-2}$ mbar. Figure 3.25 also shows that the cooling time of the ions in the trap should be several times τ_{cool} in order to extract ion pulses with minimum temperature out of the trap. The bottom part of Fig. 3.25 shows the measured time constants τ_{cool} for Cs and K ions as a function of the pressure. For the highest pressures, time constants down to a few hundred microseconds are observed.

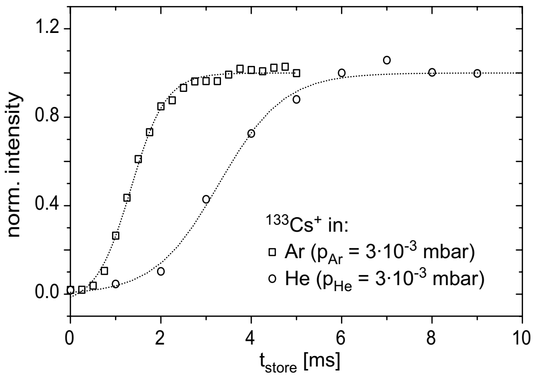

Figure 3.24: Normalized number of $^{133}Cs^+$ ions extracted from the trap as a function of the storage time inside the trap. The measurements were performed with helium and argon as buffer gas.

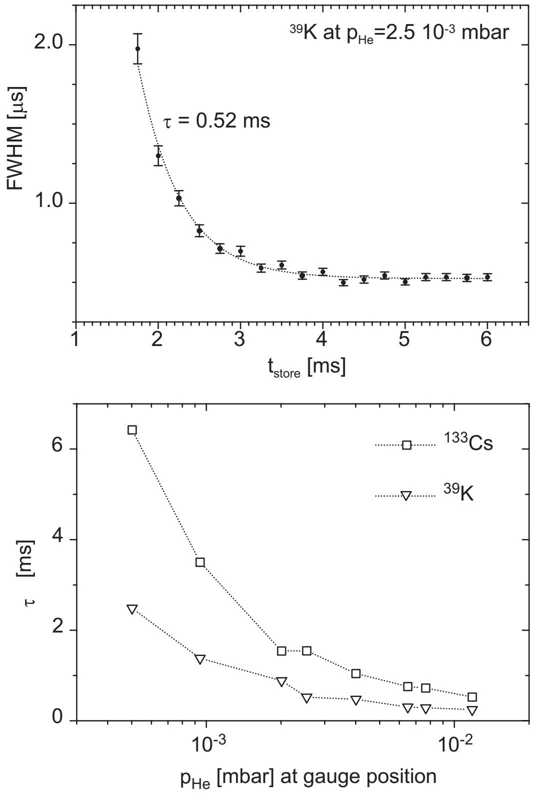

Figure 3.25: Top: temporal width of ejected ^{39}K ion pulses as a function of the storage time inside the trap. An exponential is fitted to the data. Bottom: time constants obtained as shown in the top figure as a function of the helium buffer gas pressure for K and Cs ions.

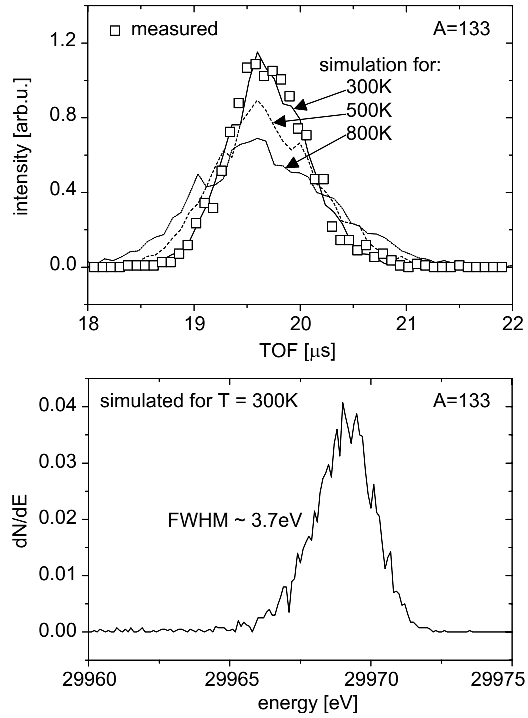

Figure 3.26: Top: temporally resolved 30-keV ion pulse (squares) of $^{133}Cs^+$ ions compared to theoretical ion pulse shapes corresponding to initial ion temperatures of 300 K, 500 K and 800 K. The theoretical curves are normalized to the same number of ions. Bottom: calculated energy spectrum of the ion pulse corresponding to the 300-K pulse shape shown in the top figure.

Cooling limit and emittance

For a determination of the final ion temperature both in the axial and radial direction, two kind of measurements have been carried out. In both cases, ions were accumulated and cooled for $T_{\rm cool} = 20\,$ms to reach their equilibrium temperature.

For the determination of the axial temperature, the number of ions in a pulse has been measured temporally resolved with the MCP detector. The measured shape of the ion pulse can be compared to calculated shapes based on ion distributions at different temperatures. Such pulse shapes are shown in the top part of Fig. 3.26 for ^{133}Cs ions extracted from the linear trap and accelerated to 30 keV. The data are plotted with respect to the time of ejection from the trap. The points correspond to the experimental data and the curves to calculated shapes for ion distributions with temperatures of 300 K, 500 K, and 800 K. A good agreement is achieved for a temperature of 300 K giving evidence that the ions reach the temperature of the buffer gas. This is in accordance with the predictions of Fig. 3.6. The bottom part of Fig. 3.26 shows the calculated energy distribution of the ejected ions. For the calculation, the confirmed 300 K ion distribution was taken together with the electric fields for the extraction as used in the experiment. From the time and energy spread of the ion pulses shown in the Fig. 3.26, an upper limit for the longitudinal emittance $\epsilon_{\mathrm{long}} \approx 10\,\mathrm{eV}\cdot\mu\mathrm{s}$ of the ion pulse ejected from the buncher is obtained.

The transverse temperature of the ions can be extracted from a beam emittance measurement. Such a measurement has been performed in the following way. The beam observation system was mounted at the 90° deflector chamber (Fig. 2.3 with the deflector removed). Ion pulses with an energy of 2.5 keV were created by using the pulsed cavity. With an einzel lens in front of the deflector chamber, the beam was focused onto the detector and the beam profile was observed with a CCD camera. The profile was found to be Gaussian shaped with 90 % of the beam within a radius of about 1.8 mm. A beam scraper mounted on a linear feed-through at a distance of 500 mm in front of the beam viewing system was used to determine the size of the beam at this position. There, a beam radius of 2.5 mm (corresponding to $> 90\,\%$ beam intensity) was observed. From this a beam divergence of 5 mrad is derived. Combining both measurements gives a rough upper limit for the transverse beam emittance of $\epsilon_{\mathrm{trans}} \approx 10\,\pi\,\mathrm{mm\,mrad}$.

If the extracted pulse was accelerated to 60 keV instead of 2.5 keV, it would have an emittance of about $2\,\pi\,\mathrm{mm\,mrad}$, which corresponds to a more than tenfold improvement with respect to the original ISOLDE beam. This shows that gas filled radio-frequency ion guides and traps can very effectively be used to improve the emittance of ion beams.

4 Mass measurements of argon isotopes

4.1 Motivation

4.1.1 The isobaric multiplet mass equation (IMME)

Since the strong, or hadronic interaction is nearly charge independent, the isospin formalism is one of the basic tools in nuclear as well as particle physics. The neutron and the proton have isospin $T = 1/2$ with $T_\mathrm{Z}^\mathrm{neutron} = +1/2$ and $T_\mathrm{Z}^\mathrm{proton} = -1/2$. Every state of a nucleus has an isospin T and belongs to a $2T + 1$ multiplet formed by "analog" levels in different isobaric nuclei. The charge of each member is measured by $T_\mathrm{Z} = (N - Z)/2$.

In light nuclei the isobaric analog states have nearly identical wave functions. The charge dependent energy difference of these states in different isobars can be calculated in first-order perturbation theory under the assumption of only two-body Coulomb forces. This leads to the simple equation, noted first by Wigner [Wig57],

$$M(T_\mathrm{Z}) = a + bT_\mathrm{Z} + cT_\mathrm{Z}^2 \tag{4.1}$$

which gives the mass M of a member of an isospin multiplet as a function of the projection T_Z of the isospin T. This quadratic relation is called the isobaric multiplet mass equation (IMME). It was thoroughly studied in the 70's and reviewed by Benenson and Kashy in 1979 [Ben79]. Looking at the quartets it was found that the IMME worked very well for 21 out of 22 cases. The only exception was the most accurately known quartet: $A = 9$, $T = 3/2$. Due to its success and due to the lack of experimental data, the IMME is widely used to determine masses and level energies, especially of the members with the lowest T_Z.

A more recent compilation of completely measured multiplets having $T \geq 3/2$, which serve to test the quadratic relationship given in Eq. 4.1, can be found in reference [Bri98]. The lowest lying $A = 9$, $T = 3/2$ quartet is still the only significant exception for quartets. Here, a cubic term dT_Z^3 with $d = 5.5 \pm 1.7\,\mathrm{keV}$ is required in order to describe the experimental data. Now, there are also six quintets with known masses. Only one of them, the $A = 8$, $T = 2$ quintet, does not agree with the quadratic form of the IMME. Here at least one higher-order term has to be added to Eq. 4.1, either dT_Z^3 or eT_Z^4, or both.

To verify the predictions of the IMME it is necessary to determine accurately the masses of all members of a multiplet with $T \geq 3/2$. For so called "ground state multiplets" the two states with the highest and lowest T_Z are the ground states of the concerned nuclides. These states are accessible to direct mass spectrometry as performed with the ISOLTRAP mass spectrometer.

4.2 The experiment

4.2.1 Production of radioactive argon

The experiment was performed at ISOLDE/CERN [Kug00] in November 1999 using the CaO target number 123 having a target thickness of 5 g/cm^2. The target was equipped with a water cooled copper transfer line between the target container and the ion source. Due to the cooled transfer line, less volatile elements are strongly suppressed before reaching the ion source .

The heated CaO target (about 1000 °C) was bombarded with bunches of 1.4 GeV protons delivered by the CERN PS-Booster accelerator. The pulses were each 2.4 μs long and arrived with a minimum distance of 1.2 s between two pulses. Per pulse about $3 \cdot 10^{13}$ protons were delivered. In the actual experiment between six and ten proton pulses per super-cycle (16 proton pulses within 19.2 s) were sent to the ISOLDE target. The radionuclides are produced by spallation of Ca and ionized in a plasma ion source filled with a xenon-argon gas mixture. After acceleration to 30 keV the ions were mass separated by the ISOLDE general purpose mass separator (GPS).

Due to the short proton pulses and the low repetition rate, the produced ion beam had a time structure determined by the diffusion time of the radionuclide from the target matrix to the ion source and its half-life [Let97]. The pulse shape, the so called release curve, is characterized by a sharp rise followed by a steep fall and a long tail determined by the half-life and diffusion time.

In the experiment described here the rise time was approximately the same for all argon isotopes. About 100 ms after the proton impact on the target the maximum argon intensity in the ISOLDE ion beam was reached. In the case of the short-lived ^{33}Ar, the maximum intensity was reached after about 100 ms.

The argon yields were determined by β-activity measurements [Gil99] and measurements of β-delayed protons [Fyn99]. The yields determined from the β-decay data are up to a factor of ten higher than those from the β-delayed protons measurements. The reason is that the β-decay measurements are not element selective and measure therefore all β activity present at mass $A = 33$. Evaluating both methods and taking the yield decrease during the run into account [Gil99] the integrated yield for ^{33}Ar could be estimated to be a few thousand ions per proton pulse. The yields for ^{34,42,43}Ar were between 10 and 100 times higher.

4.2.2 The measurement sequence

A mass measurement requires a time of flight measurement as a function of excitation frequencies. Since the time of flight measurement is destructive, a new ion pulse has to be produced, prepared and finally investigated in the high-precision trap for each excitation frequency. This sequence is in the following called a measurement cycle.

Important from the point of efficiency is that the decay losses during one measurement cycle are kept as low as possible. Therefore, the measurement cycle duration must not greatly exceed the half-life of the nuclide.

In most cases it is necessary to ensure a sufficient resolving power in the cooler Penning trap to clean isobaric contaminations delivered by ISOLDE. The resolving power depends mainly on the buffer gas pressure. Lower pressures result in higher resolving powers but also in longer periods of time for cooling the ion bunch. Furthermore, the line width of the cyclotron resonance is determined by the time the radio frequency is applied (see Sect. 2.4). This line width should be as narrow as possible to increase the precision of the mass determination. Therefore, a measurement cycle for very short-lived nuclei ($T_{1/2} < 1\,\mathrm{s}$) will always be a compromise between the needed resolving power in the cooler trap, the line width of the cyclotron resonance in the precision trap and the decay losses due to the half-life.

In Fig. 4.1 the measurement cycle is illustrated as used during the argon mass measurements for both, the reference nuclide and the investigated nuclides. The cycle was started by the proton pulse impinging on the target. After this, a 70 ms delay was introduced before the beam gate was opened for a period of about 30 ms during the time of maximum argon release.

When the beam gate was opened, the ions of the ISOLDE ion beam were continuously injected into the ISOLTRAP ion beam cooler and buncher. Within 2 ms after the beam gate closure, the ions formed a cloud in the potential well at the end of the cooler and buncher before they were extracted in a short pulse (FWHM $\approx 1\,\mu$s) at 2.5 keV kinetic energy. The energy adaption between the about 30 keV potential of the linear ion trap and the beam transfer line at ground potential is done by timely switching the first pulsed cavity (see Sect. 3.2.4).

The low-energy Ar ion pulses were then electrostatically retarded and captured in flight in the first Penning trap. Since the potential in the trap center is -10 V there is a second energy adaptation necessary, done in a second pulsed cavity. Shortly after this cavity was switched, the potential of the lower end-cap of the cooler trap was lowered to let the ions enter the trap and raised back before they could escape.

A cooling time of 8 ms served for reducing the axial amplitude of the ion bunch until the ions relaxed into the smaller harmonic potential well that makes the mass selective cooling scheme possible (see Fig. 2.4). By applying a radio frequency dipole field for 30 ms the magnetron radius of all ions, regardless their mass, was increased until they could not be ejected through the small exit hole of the cooler trap. By exciting the ions with an azimuthal RF quadrupole field for 30 ms the argon ions under investigations were re-centered in the trap (see also Sect. 2.5). After an additional cooling time of the excited cyclotron motion (5 ms), the Ar ion bunch was ejected. The ions spent a total of 73 ms in the first Penning trap. A mass resolving power of $R = 7000$ was achieved.

After this cleaning procedure, the Ar ions were transferred to the second Penning trap where they were captured in-flight. First an ion motion with a defined magnetron radius of $R \approx 1\,\mathrm{mm}$ was prepared by an RF dipole field applied for 10 ms. Then the ions cyclotron motion was excited with an azimuthal RF quadrupole field for $T_{\mathrm{RF}} = 60\,\mathrm{ms}$ yielding a line width for the cyclotron resonance of about 15 Hz. This resulted in a resolving power of

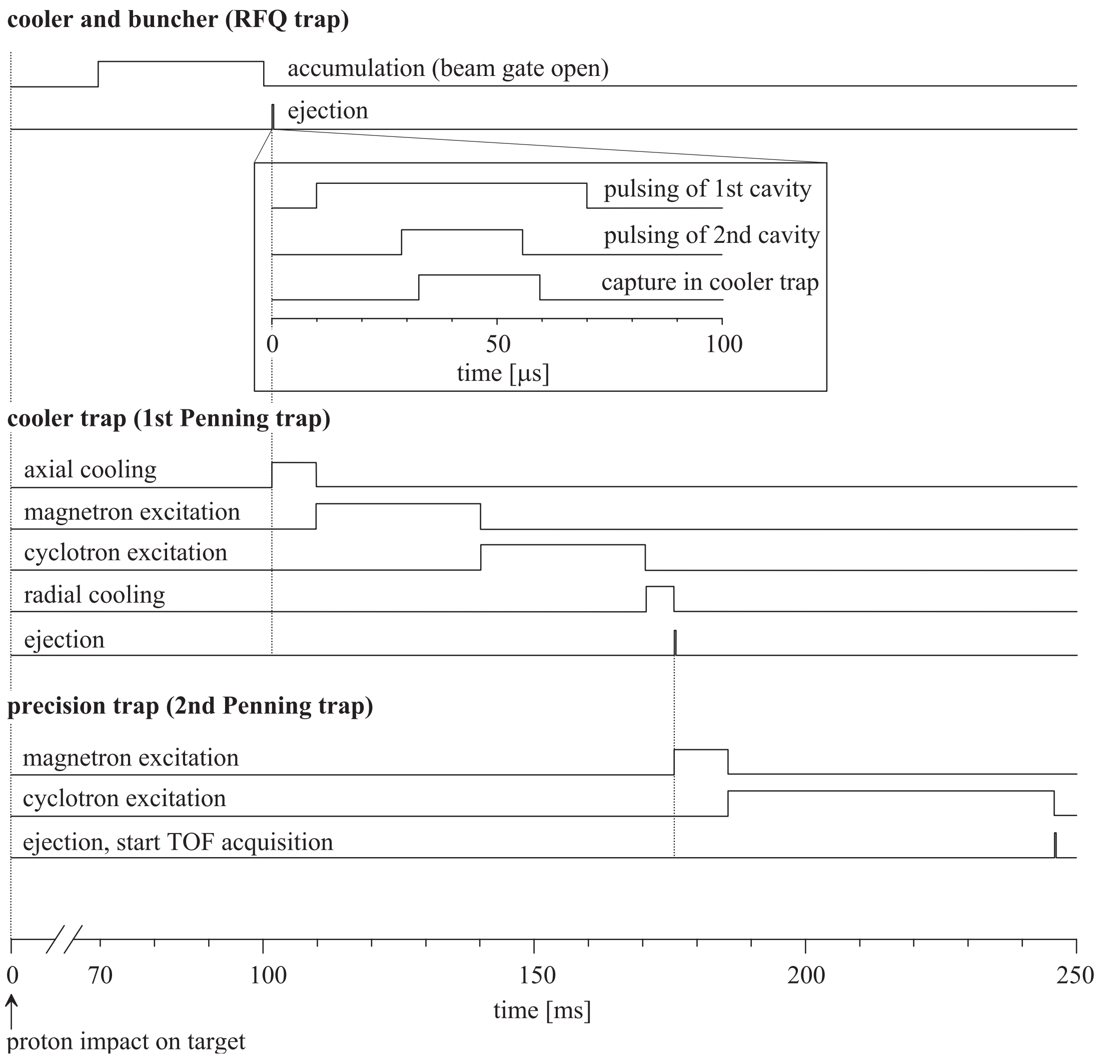

Figure 4.1: Measurement sequence for very short-lived nuclides, as for instance ^{33}Ar. The boxed area indicates an expanded time scale. This sequence is executed for each frequency step of which 41 were used to obtain a resonance.

$R = \nu_c/\delta\nu_c(\mathrm{FWHM}) = 130000$.

In total, each cycle of the measurement of the cyclotron frequency took about 175 ms. This was comparable to the half-life of ^{33}Ar ($T_{1/2} = 174.1\,\mathrm{ms}$ [Bor87]) and kept the decay losses minimal.

One example of the resulting spectra for ^{33}Ar is shown in Fig. 4.2. Plotted is the time of flight from the trap to the MCP detector versus the frequency of the azimuthal RF quadrupole field. For each point the measurement cycle was repeated about 250 times. The total number of detected ions in this cyclotron resonance is about 2000. If only measurement cycles with not more than two ions detected are taken into account, about 1500 ions are left for the evaluation. Fitting the theoretical line shape [Kön95] results in

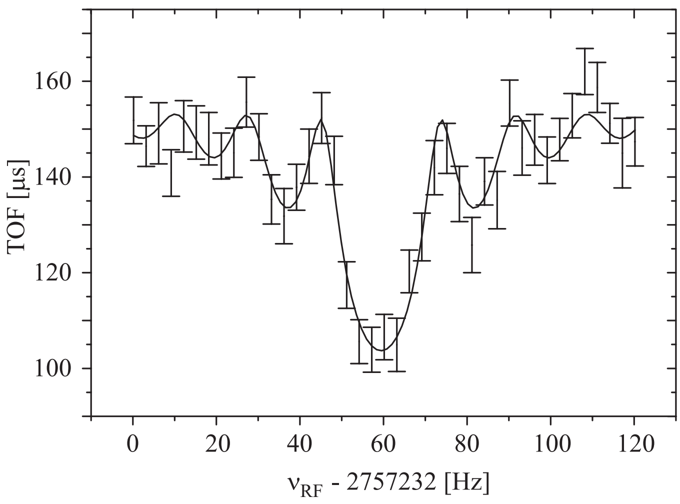

Figure 4.2: Cyclotron resonance curve for ^{33}Ar. Shown is the time of flight (TOF) of the ions from the trap to the ion detector as a function of the applied radio frequency. The solid line is a fit of the theoretical line shape [Kön95] to the data points.

$\chi^2_{\mathrm{reduced}} = 0.74$.

4.2.3 Efficiency

The overall detection efficiency of the ISOLTRAP mass spectrometer is given by the product of three types of losses or efficiencies that can be distinguished: decay losses, efficiency of the MCP detector and transfer efficiencies.

Due to a measurement cycle duration comparable to the half-life, about 50% of the ^{33}Ar ions decay before they reach the detector, i.e. $\epsilon_{\mathrm{decay}} = 0.5$. The detection efficiency for singly charged Ar ions that impinge at about 2.2 keV kinetic energy on a multi channel plate detector is between 40 and 60% [Bre95, Obe97]. Since the MCP detector used for the time of flight detection at ISOLTRAP is not equipped with an electron repelling grid, the detection efficiency is reduced by a factor of two [Bre95]. In total the detection efficiency for singly charged argon ions does not exceed $\epsilon_{\mathrm{detect}} = 0.3$ for the present setup and is likely even smaller.

The losses during the transfer of the ions from the focal plane of the ISOLDE GPS mass separator to the time of flight detection can be divided into three different contributions. About 80% of the ions starting at the focal plane of the GPS magnet arrive at the entrance of the ion beam cooler and buncher, i.e. $\epsilon_{\mathrm{beamline}} = 0.8$. The efficiency of the beam cooler and buncher has been measured to be 12…15% for xenon ions (Chap. 3.4.2). Under on-line conditions for argon the efficiency was $\epsilon_{\mathrm{buncher}} \approx 0.05$, where the main additional loss was due to charge exchange reactions with gas impurities. The main transfer losses occur during the transfer of the ion bunch into the first Penning trap where the ion optics in between the ion beam cooler and buncher and the cooler Penning trap have still to be improved. The transfer efficiency between the first and the second Penning trap is believed to be almost 100%. The total transfer efficiency from the ion beam cooler and buncher into the precision trap is therefore $\epsilon_{\text{transfer}}$.

Multiplying all efficiencies, the overall efficiency is

$$\begin{aligned}\epsilon_{\text{tot}} &= \epsilon_{\text{decay}}\cdot\epsilon_{\text{detect}}\cdot\epsilon_{\text{beamline}}\cdot\epsilon_{\text{buncher}}\cdot\epsilon_{\text{transfer}} \\ &= \ 0.5\ \cdot\ 0.3\ \cdot\ \ 0.8\ \ \cdot\ 0.05\ \cdot\ 0.02 \\ &= 1.2\cdot 10^{-4}. \end{aligned} \tag{4.2}$$

This overall efficiency ϵ_{tot} can be compared to the efficiency of ISOLTRAP determined by the ratio of the number of ^{33}Ar ions detected by the MCP and those delivered by ISOLDE at the focal plane of the GPS separator. On the average, 0.2 ^{33}Ar ions were detected for each measurement cycle by the MCP detector compared to a few thousand ^{33}Ar ions per pulse at the focal plane (see Sect. 4.2.1). This results in a total efficiency of about 10^{-4} during the argon mass measurements and is consistent with the estimated overall efficiency given by (4.2).

4.2.4 Contaminations

Penning trap mass spectrometry relies on the knowledge of the magnetic field. It is measured by measuring the cyclotron frequency of a nuclide having a well known mass. During the argon mass measurements the argon isotope ^{36}Ar, delivered by the ISOLDE ion source-target combination, was used as reference mass. The mass of ^{36}Ar is known with a relative accuracy of $\delta m/m = 8\cdot 10^{-10}$ [Car99a].

Apart from the unobserved magnetic field changes a source of systematic errors is a contamination by ions of another mass than the investigated nuclide present also in the precision trap. These so called contaminant ions cause a change of the cyclotron resonance line shape and/or a shift of the cyclotron frequency. While a distorted line shape is easily seen, it is much harder to uncover a frequency shift caused by contaminations.

It has been shown experimentally [Bol92], that the size of the shift increases with the total number of stored ions. Furthermore, it was found that the sign of the shift depends on the magnitude of the difference in the cyclotron frequencies of the two species compared to the half width of the resonances. When the mass difference is large enough for the unperturbed resonances to be separated by more than their widths, the measured resonances are both shifted to lower frequencies.

During the evaluation of the data a contamination of ^{36}Ar, the nuclide used to monitor the magnetic field strength, was uncovered by observing that the cyclotron frequency was changing with the number of detected ions. One example is shown in Fig. 4.3a, where the cyclotron frequency shifts are plotted versus the number of detected ions per cycle. A line was fitted and the slope evaluated. In Fig. 4.3b the slopes of these lines are compiled for all reference measurements. Averaging all cyclotron resonance measurements for ^{36}Ar the slope turned out to be nonzero, $\overline{S} = 0.013 \pm 0.001\,\text{Hz/(counts/cycle)}$. The decreasing

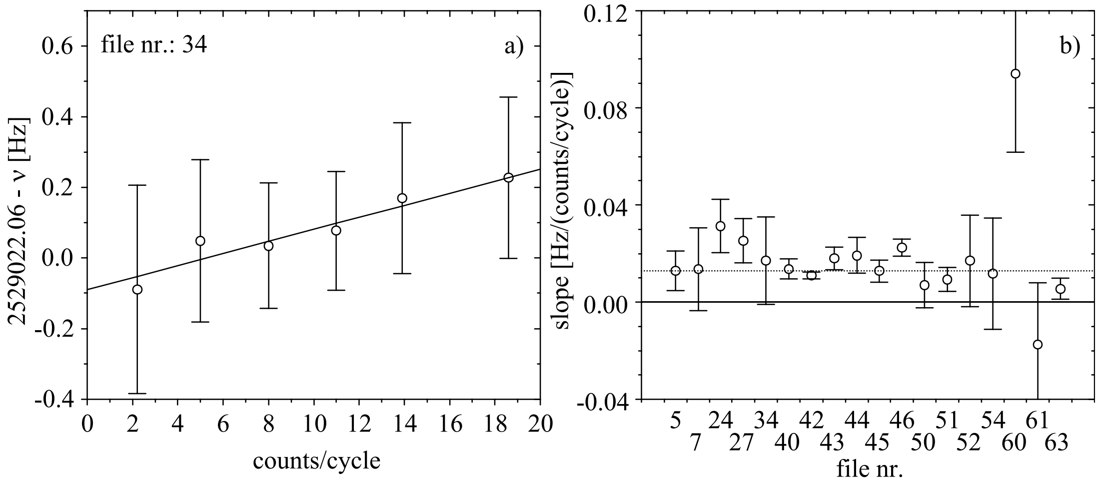

Figure 4.3: a) Plot of the cyclotron frequency for ^{36}Ar versus the number of detected ions per measurement cycle with a fitted line. b) Slopes of similar linear fits for all reference measurements. The dotted line gives the average slope used for correction (see text).

cyclotron frequency with the increasing number of detected ions per cycle indicates a contamination [Bol92], probably caused by ^{36}Cl. This contamination could not be removed in the cooler trap due to the to small mass difference to ^{36}Ar of only 700 keV. To clean this contamination in the cooler trap a resolving power of about 50 000 would have been necessary. Figure 4.3b and a Birge ratio of 1.3 for the uncertainty of the mean slope confirm that this contamination was present throughout the argon run.

To correct for this contamination, i.e. to find the true cyclotron frequency of ^{36}Ar, a straight line with the slope $\overline{S} = 0.013 \pm 0.001\,\mathrm{Hz/(counts/cycle)}$ was fitted to the cyclotron frequency shifts plotted as a function of the number of detected ions per cycle for all reference measurements. The offset of the straight line corresponds to the true cyclotron frequency of ^{36}Ar that one expects to get with a clean sample.

After the argon beam time, the cyclotron frequency for ^{39}K was measured. The mass determined for ^{39}K, using again ^{36}Ar from ISOLDE as reference, agrees well within the error bars ($\delta m/m = 1.1 \cdot 10^{-7}$) with the value in [Aud95], if the cyclotron frequency of ^{36}Ar is corrected for the effect of the contamination.

In the case of the measured radioactive argon isotopes, the resolving power $R = 7000$ (see Sect. 4.2.2) of the cooler trap was sufficient to separate them from their isobars Cl and S delivered by ISOLDE. To exclude contaminations that were not removed in the cooler trap, the measured cyclotron frequencies were investigated as a function of the number of detected ions. No dependencies are observed. Therefore, contaminations with a cyclotron frequency outside the cyclotron resonance line width can be excluded for all measured argon isotopes. Contaminations within the line width can also be excluded, because there where no ions (neither ionized atoms nor molecules) with a mass close enough to the measured isotope *and* produced and ionized at ISOLDE. Furthermore, no increase in the

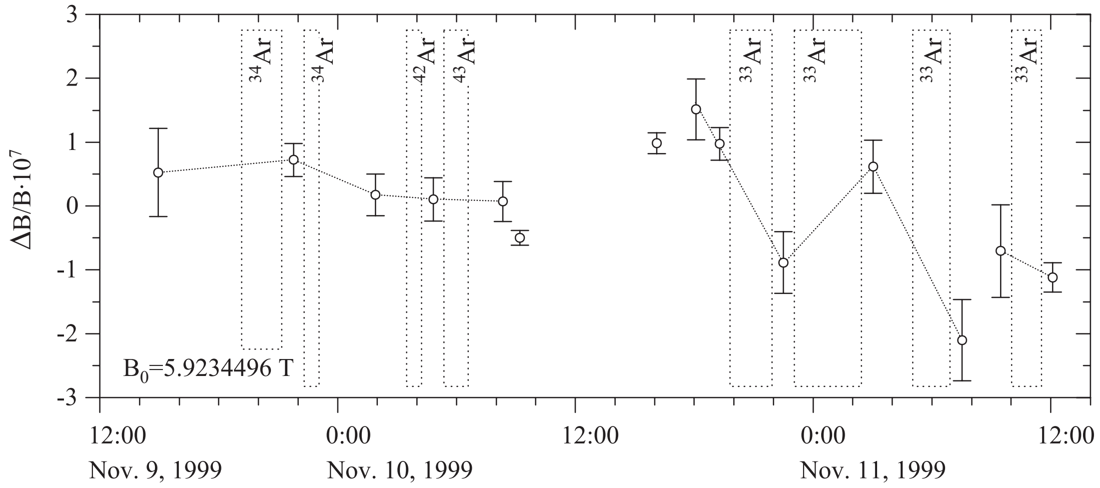

Figure 4.4: Magnetic field variations versus time monitored via the cyclotron frequency of ^{36}Ar. Shown are also the interpolations (dotted lines) of the magnetic field as present during the time the radioactive argon isotopes were investigated. The times ar indicated when the argon isotopes have been measured.

number of detected ions was found, if the opened beam gate duration was prolonged. Thus, nuclides with a slow or constant release can also be excluded as contaminants.

4.2.5 Magnetic field drift and frequency ratios

With a frequent measurement of the cyclotron frequency ν_c^{ref} of a reference nuclide the magnetic field strength is determined. In Fig. 4.4 the resulting magnetic field drift over the measurement time is plotted. The figure was made using the corrected cyclotron frequencies for the reference nuclide ^{36}Ar and the mass from [Car99a].

To determine the experimental result, the frequency ratio $\nu_c^{\mathrm{ref}}/\nu_c$, the magnetic field or the cyclotron frequency of the reference isotope needs to be known at the time the cyclotron frequency of the investigated nuclide ν_c is measured. This is achieved by linear interpolation between the reference measurements before and after the measurement of ν_c. The lines in Fig. 4.4 indicate the interpolations done to determine the frequency ratio for the measured argon isotopes.

4.3 Experimental results

The experimental result of ISOLTRAP measurements is the frequency ratio $\nu_c^{\mathrm{ref}}/\nu_c$. In Tab. 4.1 the experimental results are summarized for the nuclides investigated. The second column gives the frequency ratios $\nu_c^{(^{36}\mathrm{Ar})}/\nu_c$ with their errors. The error contains

Table 4.1: Frequency ratios of argon isotopes relative to ^{36}Ar and mass excess values (ME) as determined in this work. The last column gives literature values from [Aud95].

Nuclide	$T_{1/2}$	$\nu_{\mathrm{ref}}/\nu_{\mathrm{c}}$ $(\sigma_{stat})(\sigma_{tot})$	$\mathrm{ME}^{*}_{\mathrm{exp}}$ [keV]	$\mathrm{ME}_{\mathrm{lit}}$ [keV]
^{33}Ar	174 ms	0.917212520(087)(126)	−9381.9(4.2)	−9380(30)
^{34}Ar	844 ms	0.944747261(046)(105)	−18378.4(3.5)	−18378(3)
^{42}Ar	33 a	1.166694503(128)(173)	−34422.7(5.8)	−34420(40)
^{43}Ar	5.37 m	1.194569791(105)(159)	−32009.8(5.3)	−31980(70)

*using ME(^{36}Ar) $= -32454.927(29)\,\mu$u [Car99a]
and $1\,\mathrm{u} = 931.494013\,\mathrm{MeV}/c^2$ [Moh00].

two components that are added quadratically. The first contribution is the statistical uncertainty. It is given by the accuracy of the cyclotron frequency determinations for the reference as well as for the nuclide under investigation and the statistical uncertainty due to the interpolation of the magnetic field to the time of the frequency measurement for the measured nuclide. The second contribution is the systematic uncertainty mainly due to uncertainties in the calibration of the magnetic field.

The magnetic field is decaying with an average rate of about $5\cdot10^{-8}$ per day. The standard deviation $\sigma = 0.9\cdot10^{-7}$ of the measured points (Fig. 4.4) from this averaged decrease gives a worst case estimate for the uncertainty in the magnetic field calibration. Therefore, a conservative estimate for the relative systematic uncertainty, that contains also frequency shifts due to trap imperfections, is $1\cdot10^{-7}$ of the frequency ratio [Bec97].

The frequency ratio $\nu_{\mathrm{c}}^{\mathrm{ref}}/\nu_{\mathrm{c}}$ can be converted into an atomic mass value for the measured nuclide by

$$m = (\nu_{\mathrm{c}}^{\mathrm{ref}}/\nu_{\mathrm{c}})\cdot(m_{\mathrm{ref}} - m_{\mathrm{e}}) + m_{\mathrm{e}} \tag{4.3}$$

involving the electron mass m_{e} and the atomic mass of the reference nuclide m_{ref}. The electronic binding energy, which is in the order of a few electron volt, can be neglected at this level of accuracy. The mass excess values calculated this way are presented in column four of Tab. 4.1. For comparison, the values found in the latest atomic mass evaluation [Aud95] are given in column five.

The former measurement of the ^{33}Ar mass was performed using the ^{36}Ar(^{3}He,^{6}He)^{33}Ar reaction [Nan74]. The present ISOLTRAP measurement decreases the mass uncertainty by a factor of seven. A similar improvement in accuracy is obtained for ^{42,43}Ar. The value for ^{42}Ar was mainly determined by the investigation of the ^{40}Ar(τ,p)^{42}Ar reaction [Jar61] and the mass of ^{43}Ar was measured using the ^{48}Ca(α,^{9}Be)^{43}Ar reaction [Jel74].

In the latest atomic mass evaluation [Aud95], the mass value for ^{34}Ar is dominated by the result of the ^{36}Ar(p,τ)^{34}Ar reaction study [Har74]. The new ISOLTRAP datum agrees very well with the value from this reaction study, which is slightly more accurate than the ISOLTRAP value, thus demonstrating again the reliability of ISOLTRAP mass measurements.

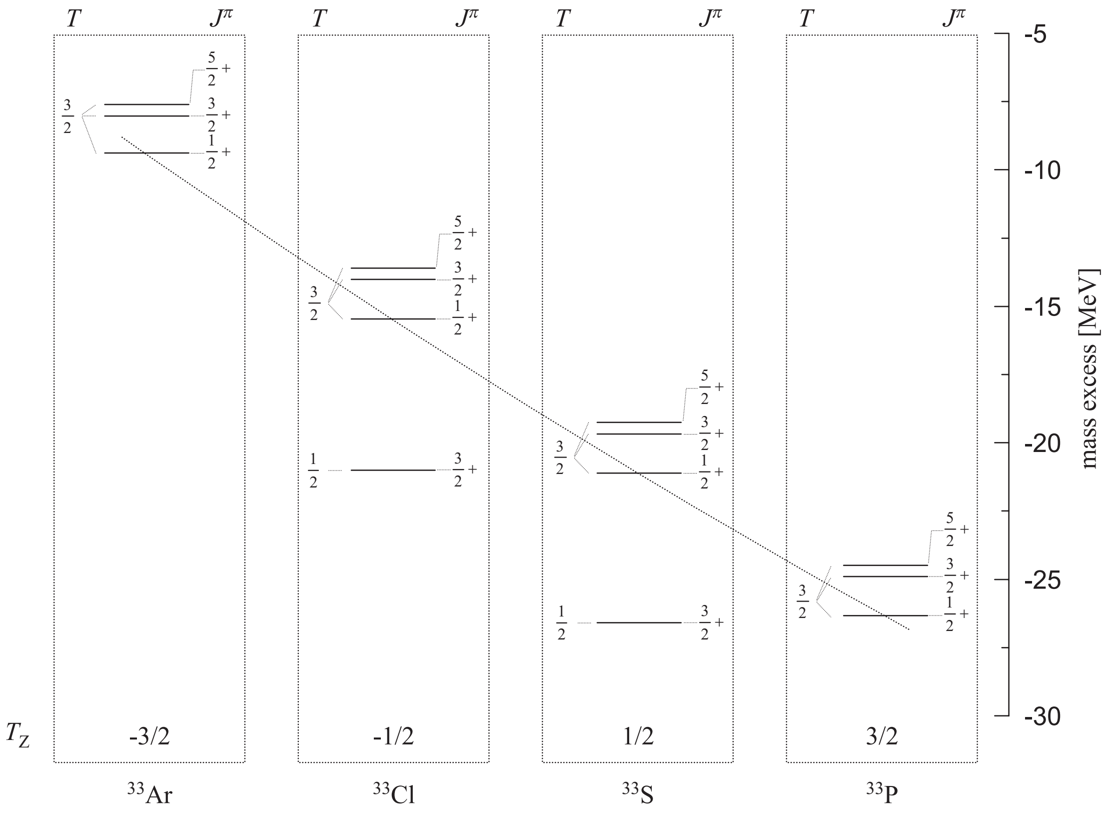

Figure 4.5: Energy levels for the $A = 33$, $T = 3/2$ isospin quartet members. The dotted line shows the curve given by the quadratic IMME for the lowest lying quartet.

4.4 Discussion of the experimental results

4.4.1 ^{33}Ar and the IMME for $A = 33$, $T = 3/2$

The isobaric multiplets for $A = 33$ are quartets formed by isobaric analog states, i.e. states with the same isospin $T = 3/2$ and the same nuclear spin and parity J^π, in ^{33}Ar, ^{33}Cl, ^{33}S and ^{33}P. In Fig. 4.5 the energy levels for the known $A = 33$, $T = 3/2$ isospin quartet members are plotted. Also shown is the curve defined by the IMME (Eq. 4.1) for the quartet with $J^\pi = \frac{1}{2}^+$, i.e. for the "ground state quartet" .

The mass of ^{33}P has been measured by two groups by determining the β^--decay end-point and was evaluated in [Aud95]. The excited levels with $J^\pi = 3/2^+$ and $5/2^+$ have been measured in ^{30}Si(α,pγ)^{33}P and ^{31}P(τ,pγ)^{33}P reactions consistently by three different groups [End78].

The excitation energy for the $J^\pi = 1/2^+$ state in ^{33}S has been measured in a number of reactions compiled in [End78, End90]. The most precise values result from the ^{32}S(n,γ)^{33}S reaction performed by two different groups [Ram85, Ken85]. The excitation energies are

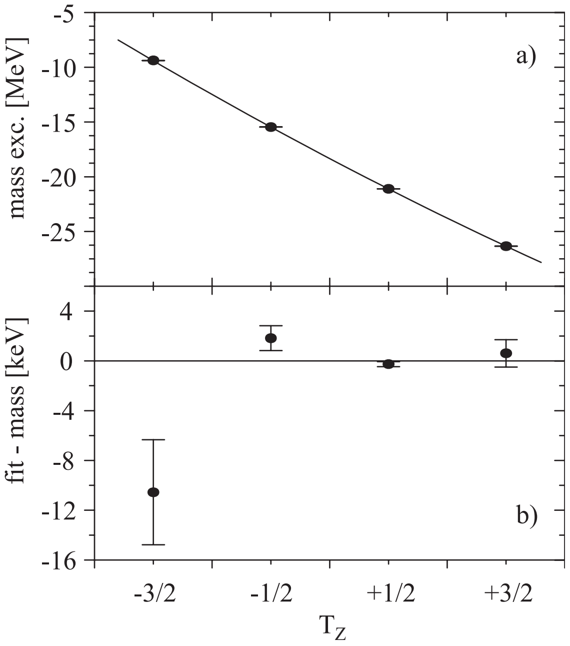

Figure 4.6: Quadratic fit to the mass excesses of the A = 33, T = 3/2, J^π = 1/2$^+$ isospin quartet members (a) and residuals (b).

E_x = 5480.1(4) keV [Ram85] and E_x = 5479.7(1) keV [Ken85]. The value used here is the adopted value from [End90], E_x = 5480.1(4) keV (from [Ram85]). In [End90] is no reason given why the value from [Ken85] is not used.

The $J^\pi = 3/2^+$ and $5/2^+$ states in ^{33}S were measured consistently using ^{34}S(p,d)^{33}S and ^{32}S(d,p)^{33}S reactions [End78].

The $J^\pi = 1/2^+$, $3/2^+$, $5/2^+$ states in ^{33}Cl have been measured by investigating the resonances in the ^{32}S(p,p')^{32}S reaction [Abb70, Abb73, Wam80]. By evaluating the references [Abb70, Abb73] a difference was found by recalculating the transformation of the proton energy from the laboratory frame to the center of mass frame (for details of this calculation see App. B). The recalculation changed the mass excesses of these states by about 1 keV compared to the values found using [Aud95, End90]. For the $J^\pi = 1/2^+$ state the mass excess changed from -15459.5 ± 1.1 keV to -15460.1 ± 1.0 keV. In [End90] the excitation energy from [Wam80] instead of the formerly used value from [Abb73] was assigned to the $T = 3/2$, $J^\pi = 5/2^+$ state. The main argument for this is the width of the resonance found in [Wam80] (Γ = 0.05 keV) that is much smaller than the one found in [Abb73] (Γ = 10 keV).

Including the ISOLTRAP data, all members of the A = 33, T = 3/2 quartets are now very well known (see Tab. 4.2). This allows a more stringent test of the quadratic IMME than before done by a least-square fit of Eq. 4.1 to the masses. Until now the test of the quadratic IMME showed consistency for the "ground state quartet" but was limited by the 30 keV [Nan74] error of the mass value of the ^{33}Ar ground state.

Table 4.2: Data of the members of the $T = 3/2$ quartets for $A = 33$ and the results of the IMME test. Excitation energies are given in the fourth column. The mass excess values given in the fifth column have been reviewed as shown in the sixt column. These data $\mathrm{ME}_{\mathrm{rev}}$ were used to determine the coefficients a, b, c and χ^2 for the quadratic IMME according to Eq. 4.1 (seventh column) and the coefficients a, b, c and d for the cubic IMME as given in the last column.

J^π	n.	T_Z	E_x [keV]	$\mathrm{ME}_{[\mathrm{Bri98}]}$ [keV]	$\mathrm{ME}_{\mathrm{rev}}$ [keV]	a, b, c, χ^2 [keV]	a ,b ,c ,d [keV]
$\frac{1}{2}^+$	P	3/2	0	-26337.7(1.1)	-26337.7(1.1)[a]	$a = -18334.57(49)$	$a = -18366.04(67)$
	S	1/2	5479.7(1)[b]	-21106.1(5)	-21106.54(15)[a,b]	$b = -5648.15(87)$	$b = -5645.3(1.2)$
	Cl	−1/2	5543.4(1.1)[c]	-15460(2)	-15460.1(1.0)[a,c]	$c = 208.81(7.0)$	$c = 211.7(1.1)$
	Ar	−3/2	0	-9380(30)	-9381.9(4.2)[d]	$\chi^2 = 10.6$	$d = -2.95(90)$
$\frac{3}{2}^+$	P	3/2	1431.6(2)[b]	-24906.1(1.2)	-24906.1(1.1)[a,b]	$a = -16903.3(2.5)$	$a = -16898.3(2.7)$
	S	1/2	6905(3)[b]	-19681(3)	-19681.2(3.0)[a,b]	$b = -5649.6(3.6)$	$b = -5665.2(4.8)$
	Cl	−1/2	6982.9(3.0)[c]	-14020(3)	-14020.7(3.0)[a,c]	$c = 209.5(2.9)$	$c = 189.5(5.1)$
	Ar	−3/2	1344(20)[e]	-8036(36)	-8038(20)[d,e]	$\chi^2 = 22.8$	$d = 18.9(4.0)$
$\frac{5}{2}^+$	P	3/2	1847.60(14)[b]	-24490.1(1.1)	-24490.1(1.1)[a,b]	$a = -16479.5(2.8)$	$a = -16479.4(2.8)$
	S	1/2	7337(4)[b]	-19249(4)	-19249.2(4.0)[a,b]	$b = -5635.0(3.7)$	$b = -5637.2(5.1)$
	Cl	−1/2	7390.9(2.1)[d]	-13612(2)	-13612.6(2.0)[a,d]	$c = 196.4(3.5)$	$c = 193.9(5.1)$
	Ar	−3/2	1786(20)[e]	-7594(36)	-7596(20)[e,f]	$\chi^2 = 0.42$	$d = 2.6(4.0)$

[a] from [Aud95]
[b] from [End90]
[c] from [Abb70, Abb73] but recalculating the center of mass energy of the protons, see App. B
[d] from [Wam80]
[e] this work
[f] from [Nan74]

The result of the fit is shown in Fig. 4.6 and Tab. 4.2. The fit of a quadratic function to the data results in $\chi^2 = 10.6$. The probability that this χ^2 value occurs is only 0.1% if the data was described by a quadratic function. Using the data as given in Tab. 4.2 and allowing for a cubic term dT_Z one obtains a d-coefficient of $d(^{33}\mathrm{Ar}) = -2.95 \pm 0.90\,\mathrm{keV}$ that is not consistent with zero.

If the excitation energy for the $J^\pi = 1/2^+$ state in ^{33}S is taken from ref. [Ken85] instead of the adopted value in [End90], the quadratic fit results in $\chi^2 = 9.7$. The fit with a cubic term gives $d = -2.75 \pm 0.88$ keV. That means, there is no major change in the result if the excitation energy for the $T = 3/2$, $J^\pi = 1/2^+$ state in ^{33}S is taken from the source that was not accepted for the compilation in [End90] even though the two values from [Ken85] and [Ram85] do not agree.

Investigating the excited quartets for $A = 33$ one finds improved accuracy for the mass of the excited states of ^{33}Ar due to the improved accuracy for the ground state mass. Using the new ground state value together with the excitation energies from [Nan74] yields d-coefficients of 18.9 ± 4.0 keV and 2.6 ± 4.0 keV for the $J^\pi = 3/2^+$ and $5/2^+$ quartets, respectively. The already previously noted deviation from zero of the d-coefficient of the $J^\pi = 3/2^+$ quartet [Bri98] is now the most significant deviation in all completely measured isospin quartets. However, it is very probable that the level assignment in ^{33}Cl is wrong for the $T = 3/2$, $J^\pi = 3/2^+$ state. By comparing the level widths of the $J^\pi = 1/2^+$ ($\Gamma = 0.1\,\mathrm{keV}$), $J^\pi = 3/2^+$ ($\Gamma = 10\,\mathrm{keV}$) and the $J^\pi = 5/2^+$ ($\Gamma = 0.05\,\mathrm{keV}$) states [End90], it seems that the $J^\pi = 3/2^+$ state is not the isobaric analog state with $T = 3/2$. A hint in this direction is also given in [Wam80], where the value for the $J^\pi = 5/2^+$ level was measured basically on top of the much wider resonance measured in [Abb73] that was formerly assigned to the isobaric analog state. Consequently, we can not consider, the isobaric analog state in ^{33}Cl with $T = 3/2$ and $J^\pi = 3/2^+$ to be measured.

In Fig. 4.7 the d-coefficients for all completely measured quartets are plotted together with the significance of their deviations from zero. All together there are now five quartets with a d-coefficient deviating by two or more standard deviations from zero and thus, in significant disagreement with the quadratic IMME. Statistics allows only 0.8 cases.

There has been great effort to explain a nonzero d-coefficient, triggered by the $A = 9$ ground state quartet. The significant result for the $A = 9$ quartet has partly been explained by isospin mixing effects in the $T_\mathrm{Z} = -1/2$ and $+1/2$ members [Hen69, Jän69a], by the expansion of the least bound proton orbit in ^{9}C, as well as by charge-dependent nuclear forces [Ber70]. However, the situation rests unclear.

In the case of the $A = 33$, $T = 3/2$ quartets, the Thomas-Ehrman shift has to be considered for the proton unbound states in ^{33}Cl. However, in Ref. [Jän69b] it is shown, that this is practically fully absorbed in the a, b, and c-coefficients of Eq. 4.1 and that the contribution to a d-coefficient remains very small.

In conclusion, even though it is not clear which effect causes the breakdown of the IMME for the described $A = 33$, $T = 3/2$ quartets, it is necessary to be very careful if one derives high accuracy masses of proton-rich configurations from the IMME.

In general a three sigma deviation does not seem to be too drastic. But what if important

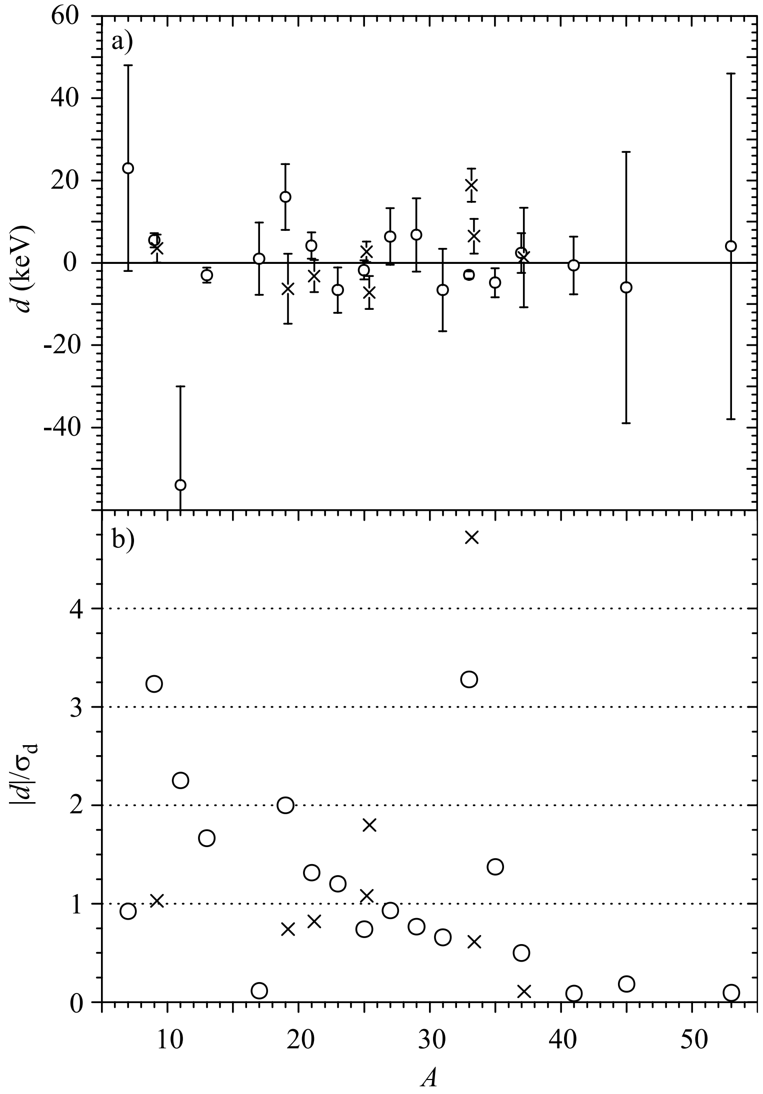

Figure 4.7: a) d-coefficients of all completely measured quartets and, b) the significance of their deviation from zero $S = |d|/\sigma_\mathrm{d}$. The circles label the ground state quartets and the crosses the higher lying quartets. The data for the $A = 33$ quartets are from Tab. 4.2, the other data are from Ref. [Bri98].

experimental results are based on a value that might be inaccurate by so much? One prominent example is the recently performed experiment by Adelberger et al. [Ade99]. With this experiment the constrains on scalar weak interactions were improved investigating with high precision the positron-neutrino angular correlation in the ^{32}Ar β decay. The positron-neutrino angular correlation is inferred from the recoil momentum of the daughter nucleus ^{32}Cl. Since the daughter nucleus is proton unstable its momentum can be determined from the momentum of the emitted proton provided that the kinematics of the decay is known with sufficient precision. The uncertainty in the kinematics is dominated by the uncertainty of the mass difference Δ between the parent and the daughter states of the β decay.

The experimental result is the asymmetry parameter $\tilde{a} = 0.9989 \pm 0.0052(\text{stat}) \pm 0.0039(\text{syst})$. The effect of the uncertainty of Δ or equivalently of a change of the mass of ^{32}Ar on $\tilde{a}$ is discussed in [Ade99] resulting $\delta a/\delta\Delta = -1.2 \cdot 10^{-3}\,\text{keV}^{-1}$. Since the uncertainty $\delta m = 50\,\text{keV}$ of the experimental mass value for ^{32}Ar was the largest uncertainty in the evaluation of $\tilde{a}$, the group decided to use the IMME to obtain a more precise estimate for the mass difference Δ between ^{32}Ar and the daughter state in ^{32}Cl. The calculation using the IMME yielded an uncertainty of only 2.2 keV for the mass difference Δ.

Since the origin of deviations of the IMME from its quadratic form in the cases of the $A = 8$, 9 and 33 multiplets have only partly been explained, a deviation in the case of $A = 32$ can not be excluded either. A correspondingly large d-coefficient would shift the mass of ^{32}Ar by 20 keV and result in a change of the $\tilde{a}$-parameter by three sigma assuming an error of less than 3 keV on Δ. The present result of Adelberger et al. is consistent with the Standard Model without the need of scalar currents. A breakdown of the IMME in the case of ^{32}Ar as large as observed in the other out-standing cases would correspond to a three sigma evidence for scalar currents. This indicates that caution is mandatory if IMME is to be used in such critical cases.

5 Summary and outlook

The work presented here demonstrates for the first time the accumulation, bunching, cooling and emittance improvement of radioactive ion beams from an on-line mass separator by means of a linear radio-frequency ion trap. The efficiency of the system and the properties of the ion bunches are in agreement with theoretical expectations. This RFQ ion beam cooler and buncher has been installed at the ISOLTRAP experiment. Compared to earlier versions of the ISOLTRAP experiment the efficiency has been increased by three orders of magnitude. This enables ISOLTRAP to be applied to very exotic nuclides with low production rates as for instance ^{33}Ar delivered by ISOLDE with an intensity of only a few thousand atoms per second.

In the scope of this work mass measurements were performed on radioactive argon isotopes. With the investigated isotopes ^{33,34,42,43}Ar, the ISOLTRAP spectrometer was for the first time applied to relatively light nuclides. Furthermore, ^{33}Ar with its half-live of only 174 ms is the shortest-lived nuclide ever investigated in a Penning trap. Hence, the present work demonstrates that the Penning trap technique is also applicable to nuclides with an half-life well below one second.

Using the ISOLTRAP Penning trap mass spectrometer, it has already been shown that for half-lives greater than one second the accuracy obtained is independent of the half-live of the measured nuclide. In this work it has been proven that it is possible to obtain an accuracy of $\delta m/m \approx 1 \cdot 10^{-7}$ even for nuclides with half-lives as short as a few hundred milliseconds. This has been the case for ^{33}Ar having a half-live of only 174 ms.

The high accuracy measurement of ^{33}Ar has permitted a stringent test of the isobaric multiplet mass equation (IMME). It provides evidence that an additional cubic term is required for the $A = 33$, $T = 3/2$ and $J^{\pi} = 1/2^{+}$ quartet. Consequently, the generally accepted quadratic form of IMME is not able to reproduce the experimental data.

Regardless the immense progress achieved, there are certain points that have to be improved in the future in order to extend the applicability of the ISOLTRAP spectrometer to even weaker beams delivered by ISOLDE. Already by the application of higher RF-amplitudes in the ion beam cooler and buncher, the efficiency for at least the heavier nuclides could be improved. The transfer optics between the ion beam cooler and buncher and the first Penning trap is presently under investigation and will be improved by using further beam diagnostics. Additionally, the single ion detection at the top of the setup is going to be improved by post-acceleration of the ions and by adding an electron repelling grid. The next step is a novel detection system, based on secondary electron emission from a metallic foil that is able to detect 100% of the incident ions.

To speed up the measurement cycle, argon buffer gas in the cooler trap could be used. Furthermore, one could profit from the fact that the ion beam cooler and buncher delivers already a cold ion bunch. Adapting the shape of the trapping potential to this fact could save time used for axial cooling.

The already substantial sensitivity of the ISOLTRAP spectrometer together with further improvements especially in efficiency opens the door to a highly interesting mass measurement program. There are three main areas of interest.

Further IMME tests: Possible candidates are isospin quartets or quintets where all members but one are well known. Often the trouble spot is the ground state mass of the most exotic member - A quantity that can now easily be measured with the ISOLTRAP spectrometer. Nuclides of this kind produced by ISOLDE in sufficient amounts (presently more than 1000 ions per second) are for instance ^{17}Ne, ^{17}N and ^{35}K. The present uncertainties on their mass values range from 15 to 50 keV. ISOLTRAP measurements could reduce them by at least one order of magnitude.

Mass measurements of nuclides interesting for fundamental tests: Already, first measurements on the very short-lived nuclide ^{74}Rb ($T_{1/2} = 65\,\mathrm{ms}$) have recently been performed using ISOLTRAP. A mass uncertainty of about 30 keV has been reached. The accuracy will be improved in future measurements aiming for an ultimate mass uncertainty of only 1 keV in order to perform a high accuracy CVC-test. The nuclide ^{34}Ar has been remeasured very recently and the data are under evaluation. During this measurement particular attention was paid to control the systematic errors introduced by unobserved magnetic field changes. Hence, the uncertainty of the mass value for ^{34}Ar is expected to be below 1 keV. Along with a repeated measurement of ^{33}Ar aiming for an even higher accuracy, the mass of ^{32}Ar will be measured in the near future.

Astrophysically interesting nuclides: The masses of ^{76,77}Sr and ^{129,130,132}Sn have been measured while this thesis was written. Further measurements will be performed to complete the map of masses in these regions. The special interest arises from the fact that the paths of the rp- and the r-process run through these nuclides or close by. These phenomena of stellar nucleosynthesis are thought to be responsible for producing the bulk on heavy elements in cataclysmic, explosive scenarios.

A Ion optics

A.1 Transfer of the ISOLDE ion beam to the ISOLTRAP cooler and buncher

The new dimensions of the ion beam cooler and buncher compared to the formerly installed very large Paul trap [Sch99] required a change of the ISOLDE beam line just in front of the ISOLTRAP setup. Two quadrupole doublets were replaced by a quadrupole triplet. The beam scanner and Faraday cup had to be moved slightly upstream. The last quadrupole is a steering quadrupole, i.e.the quadrupole field can be made slightly asymmetric and thus redirect the ion beam. In Fig. A.1 the rearranged beam line is displayed from the last ISOLDE beam switchyard up to the entrance of the ion beam cooler and buncher.

The new beam line required a recalculation of the ion beam optics to make sure that the quadrupole triplet could deliver a beam well matched to the acceptance of the ion beam cooler and buncher. In fact, the focus in the plane of the scanner CC0.SC80, just in front of the last switchyard, had to be converted into a beam focus in the region of the deceleration electrode of the ion beam cooler and buncher. These calculation were done with GIOSP [Wol87]. The result of these calculations are summarized in a beam emittance diagram just in front of the deceleration electrode (see Fig. 3.7). Together with the acceptance diagram it can be seen that the quadrupole triplet is sufficient to focus the beam, even though the focal plane is quite far away ($\approx 2\,\mathrm{m}$). The beam transfer upstream from the switchyard was not changed. For a detailed discussion see [Sch99].

To tune the beam for injection into the ion beam cooler and buncher the first step is to create a well focussed beam in the plane of the scanner CD0.SC80. Then the isolated plate just in front of the injection electrode (see Fig. 3.11) is read using a picoamperemeter. Doing this, the deceleration electrode should be close to its final voltage (see Tab. 3.2). The beam is now tuned for maximum transmission trough this electrode, i.e. for minimal beam current on this electrode. As a consequence the focus will shift away from the plane of the beam scanner towards the ion beam cooler and buncher. Now the tuning procedure continues as described in Sect. 3.4.1.

A.2 Transfer of the ion bunch to the first Penning trap

In the bottom of Fig. A.1 and in Fig. A.2 the ion optics for the transfer from the ion beam cooler and buncher to the first Penning trap, the cooler trap, is outlined. The optics involve two pulsed cavities for energy adaptation, a number of einzel lenses and an achromatic bender.

After the ion bunch leaves the ion beam cooler and buncher extraction system (see Sect. 3.3.3) it passes a first einzel lens before it is sent through an ISOLDE type quadrupole

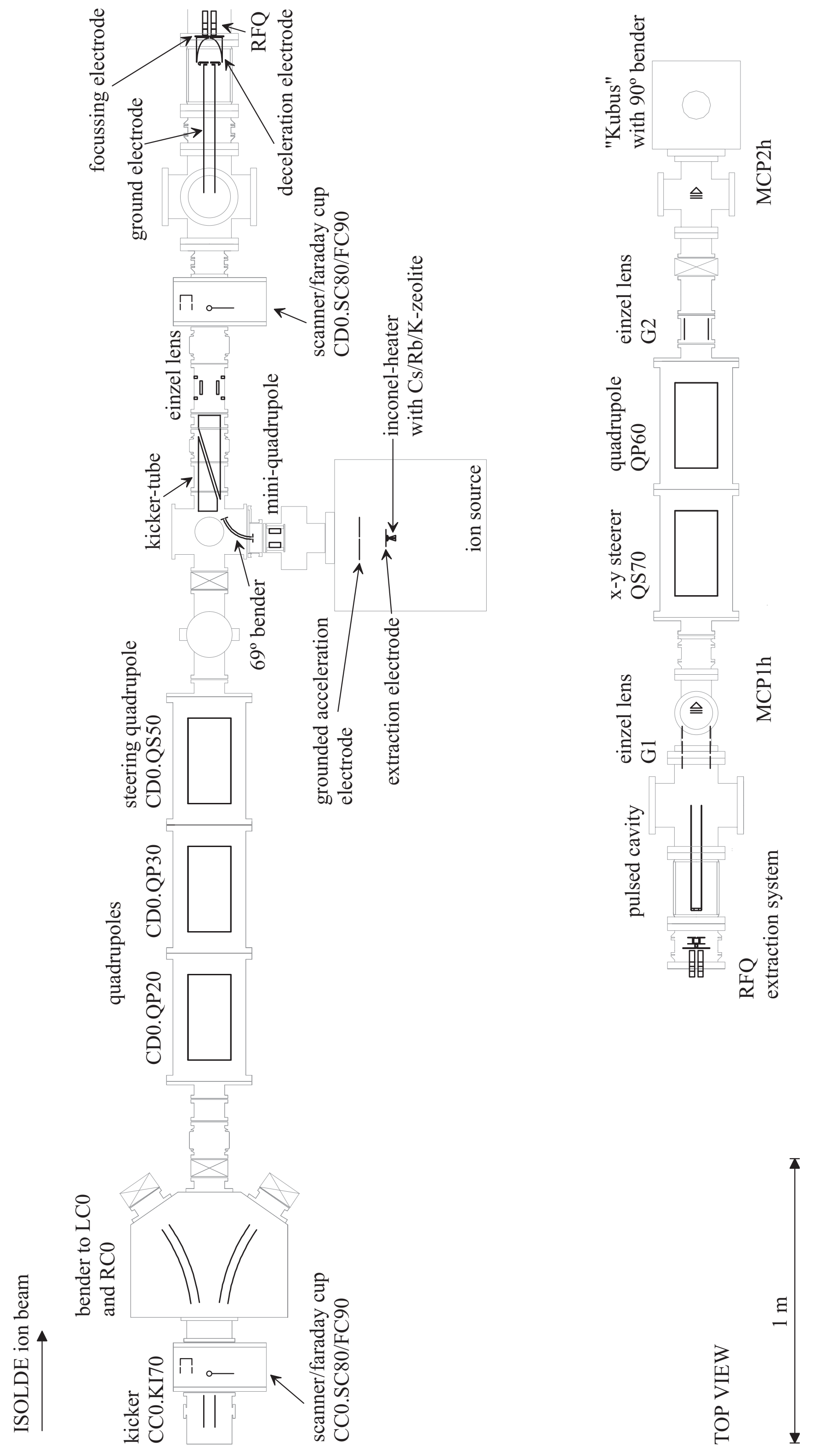

Figure A.1: Beamline in front of and behind the ion beam cooler and buncher (top view).

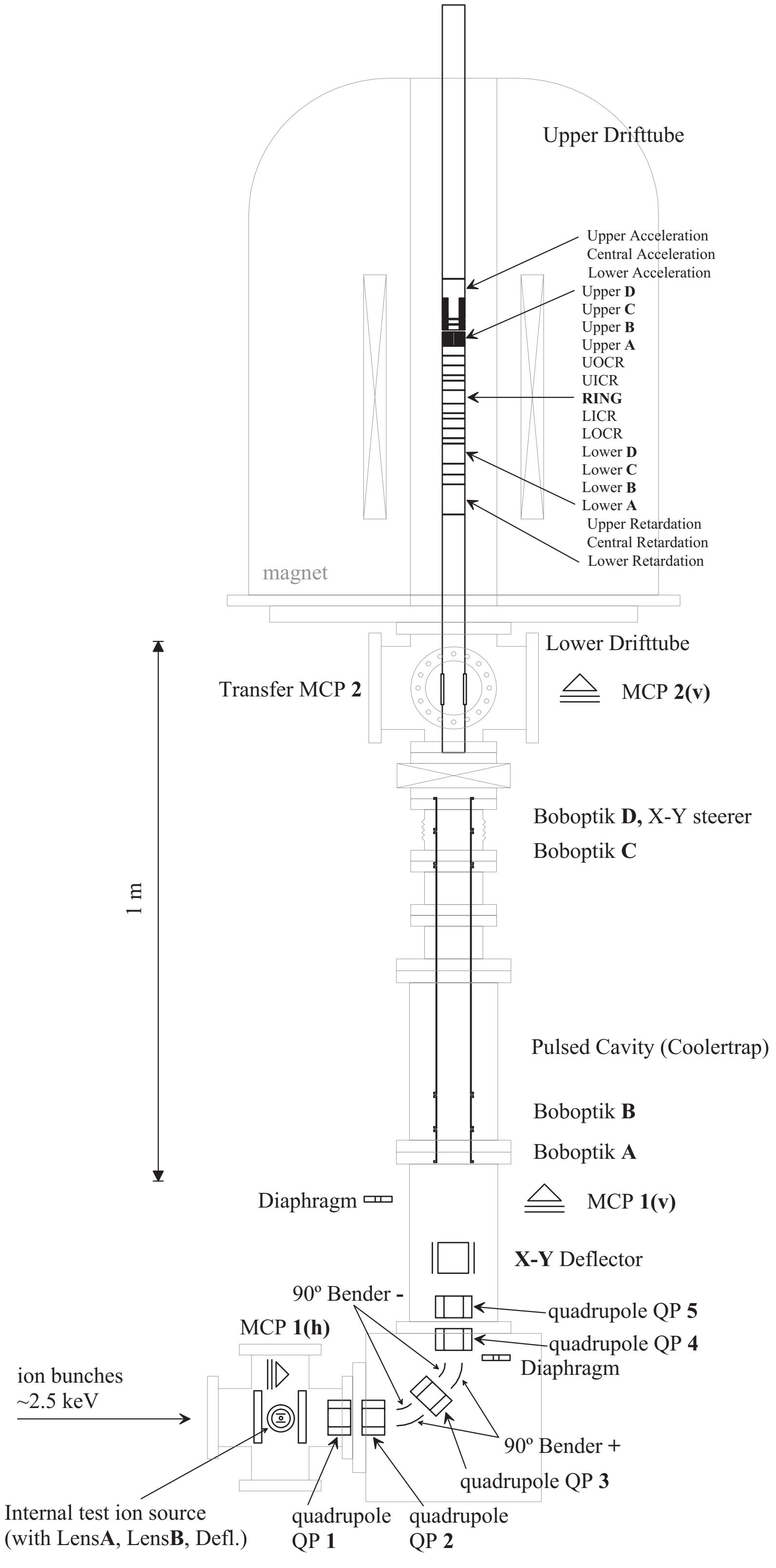

Figure A.2: Beam transfer line to the first Penning trap (side view).

doublet. The electrodes of the first quadrupole are supplied like steerer electrodes would be, opposite electrodes carry opposite polarities, thus there is no focussing effect. This quadrupole is used to steer the beam while the second one is not used and grounded. Before the ions enter the achromatic bender they pass another einzel lens used to focus the beam.

The bender consists of a quadrupole doublet followed by a cylindrical 45°-bender, a quadrupole, another cylindrical 45°-bender and a final quadrupole doublet (see Fig. A.2). This setup provides achromaticity if operated correctly. The difficulty here is to find optimal settings for the further transfer and especially for the injection into the first Penning trap. Until now this effort is thwarted by insufficient beam diagnostic tools. Presently it is impossible with the existing multi channel plate detectors to judge the transversal symmetry of the ion beam that is crucial for the injection into the cooler trap. To control the direction of the ions two small diaphragms (ca. 4 mm diameter) can be inserted. The optimal transmission to the available channel plates in front of the cooler trap results in a beam that is as straight as possible. Two sets of x-y-steerers, on either side of the 5 electrodes that constitute the "bob optic", are used to counterbalance possible misalignments.

The "bob optic" consists of 5 cylindrical electrodes. The central electrode is a pulsed cavity, that is used to adjust the potential energy of the ions such that they can be decelerated into the cooler trap close to ground potential. The first two and the last two electrodes are used to focus the beam into the magnetic field with the least possible radial energy pickup, i.e. as parallel as possible to the magnetic field lines. Then the ions enter the retardation section and are decelerated until they come to rest in the cooler trap.

These optics have been designed and setup in the thesis work A. Kohl [Koh99]. Calculations described in the thesis and also calculations performed subsequently and using a more realistic description of the bender show that an ion beam as delivered by the beam cooler and buncher should be trapped with at least 40% efficiency. Unfortunately the efficiency reached experimentally is much lower. The reason is still unkown and under investigation. It is either a serious problem with the beam shape that prevents efficient injection into the magnetic field or a problem related to the optics behind the cooler trap responsible for the transfer from the cooler to the precision trap. A beam viewing system based on a channel plate setup having a phosphorous screen as anode will be set up in the near future to distinguish between these two possibilities. With this system the beam shape can be controlled at the positions of the two vertical channel plates before injecting into the cooler trap.

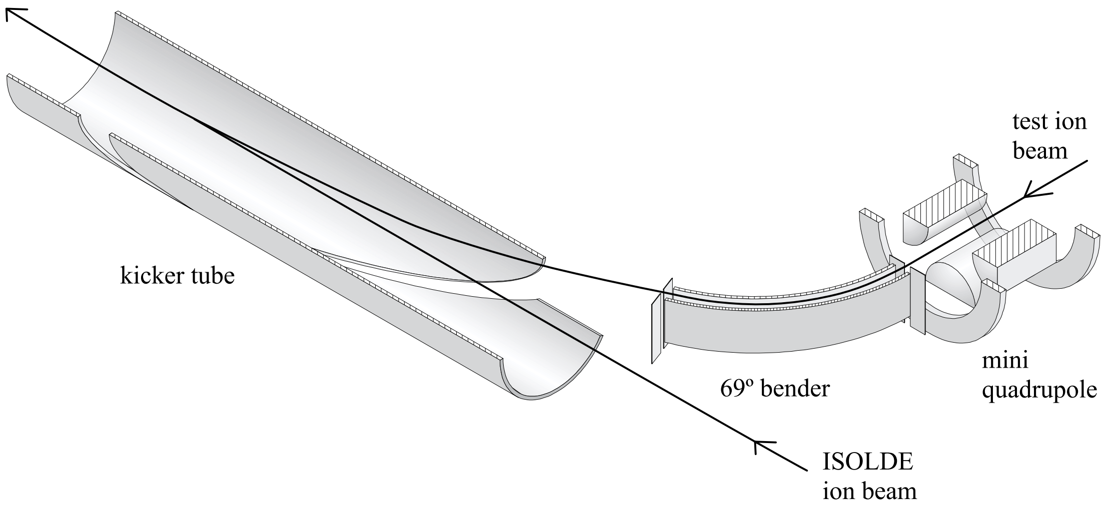

Figure A.3: New ion optics for the test ion source. It allows using the ISOLDE or test ion beam by switching the potential of the kicker tube.

A.3 A new injection optics for the test ion source

Since the newly installed ion beam cooler and buncher has to be prepared and tested with an ion beam comparable to the ISOLDE ion beam at least in energy, a 60 keV ion source is needed. An ion source with the necessary characteristics has initially been built to test the very large Paul trap [Sch99, GD96]. It delivers an ion beam with up to 60 keV ion energy. It is based on surface ionization and delivers cesium, rubidium and potassium ions.

Until recently this test ion source had to be inserted in place of a beam tube in the ISOLDE beam line. To overcome this disadvantage and to operate the test ion source also during the beam times with radioactive beam from ISOLDE, a new ion optics had to be developed and designed. This optics should allow one to switch quickly between the ISOLDE and the test ion beam.

For this purpose a bender-kicker system was designed with the aim of a maximum free space to let the relatively large ISOLDE beams pass. The system consists of a small quadrupole followed by a cylindrical bender and a slotted tube used as a kicker (see Fig. A.3). The quadrupole is used for vertical steering and to correct for the asymmetry a cylindrical bender introduces into the beam. The bender deflects the ion beam by 69° followed by another 21° bending performed by the kicker tube. By the following einzel lens (see Fig. A.1) the beam is focussed into the deceleration electrode of the ion beam cooler and buncher. The ISOLDE beam can pass just by switching off the voltages at the kicker tube electrodes and at the einzel lens.

To control the ion beam intensity, one of the bender electrodes is used as a beam gate.

Table A.1: Typical voltages used at the new ion source injection optics for a 60 keV ion beam.

element		exp. [V]	sim. [V]
mini quadrupole	top	−437	±1 600
	bottom	−810	
	left	+410	
	right	+831	
69°-bender	outer electrode	+5 060	±4 950
	inner electrode	−4 680	
kicker tube	outer electrode	+4 460	±4 780
	inner electrode	−4 460	
einzel lens		+15 000	+22 000

A fast transistor switch[1] is used for changing rapidly (within less than one microsecond) between the nominal voltage and ground potential. The period of time the nominal voltage is supplied to the electrode defines the fraction of the ion beam which is directed to the ion beam cooler and buncher.

In Tab. A.1 typical parameters are summarized for operation with a 60 keV ion beam. The values calculated with SIMION 3D 6.0 [2] are given along with the values obtained experimentally.

While the experimental values for the kicker and bender electrodes are in very good agreement with the simulations, the voltages at the focussing elements, the quadrupole and the einzel lens, are found experimentally considerably lower than in the simulations. One possible reason might be that the beam was focussed into the plane of the 6 mm hole in the deceleration electrode within the simulations. In practice it could be better to avoid a strong focus at this point and to try to keep the divergence as low as possible at the expense of the spatial extend of the ion beam.

---

[1] Behlke Elektronik

[2] An ion optics simulation program by David A. Dahl

B Relativistic kinematics

B.1 Basic equations

A particle with total energy E and 3-momentum p has the 4-momentum vector $\mathbf{p} = (E, p)$. Let the rest mass of the particle be m and its velocity be v. Then

$$\beta = \tfrac{v}{c} \quad \text{and} \quad \gamma = \tfrac{1}{\sqrt{1-\beta^2}} \tag{B.1}$$

holds, with c beeing the speed of light in vacuum. If we adopt units where $c = 1$ (natural units), then

$$\begin{aligned} E &= m + T = \gamma m && \text{(B.2)} \\ \mathbf{p} &= \beta E = \beta\gamma m = \sqrt{E^2 - m^2}\ , && \text{(B.3)} \end{aligned}$$

where T is the kinetic energy of the particle.

B.2 Lorentz transformation

Consider a particle with the 4-momentum $\mathbf{p} = (E, p)$ viewed from a second frame moving at the velocity β^* relative to the original frame and

$$\gamma^* = \frac{1}{\sqrt{1-(\beta^*)^2}}\ . \tag{B.4}$$

The components of $\mathbf{p}$ in the second frame are denoted by $\mathbf{p}^* = (E^*, p^*)$. In the special case that the second frame moves along the z-direction one obtains

$$E^* = \gamma^* E - \beta^*\gamma^*\beta E\ . \tag{B.5}$$

For a particle with 4-momentum $\mathbf{p}_1$ impinging on a target particle with its 4-momentum $\mathbf{p}_2$, the first frame could be the laboratory frame, where the target particle is at rest, while the second frame could then be the center of mass frame. In this case the Lorentz transformations give the transformation from the laboratory frame to the center of mass frame with

$$\beta^* = \beta^{\mathrm{cm}} = \frac{\mathbf{p}_1}{E_1 + m_2} \tag{B.6}$$

and

$$\gamma^* = \gamma^{\mathrm{cm}} = \frac{E_1 + m_2}{(E_1 + m_2)^2 - (\mathbf{p}_1)^2} = \frac{1}{\sqrt{1-(\beta^{\mathrm{cm}})^2}}\ . \tag{B.7}$$

B.3 Calculation of the center of mass energy for the ^{32}S(p,p$\prime$)^{32}S reaction

The reaction ^{32}S(p,p$\prime$)^{32}S shows a resonance at the energy $E_p^{\text{lab}} = 3370 \pm 1\,\text{keV}$ of the incident proton [Abb70]. This resonance corresponds to the $T = 3/2, J^\pi = 1/2+$ state in ^{33}Cl.

Knowing the proton energy in the laboratory frame E_p^{lab} and its mass m_p it is possible (see Tab. B.2) to calculate

$$\gamma = 1 + \frac{E_p^{\text{lab}}}{m_p} \quad = \quad 1.003592(1) \tag{B.8}$$

$$\beta = \sqrt{1 - \frac{1}{\gamma^2}} \quad = \quad 0.08453(1)\ . \tag{B.9}$$

using the equations (B.2) and (B.1). For the center of mass system one finds by using the equations (B.3), (B.2) and (B.6)

$$\beta^{\text{cm}} = \frac{m_p \gamma \beta}{m_p \gamma + m_{^{32}\text{S}}}\ . \tag{B.10}$$

Using (B.7) and (B.5) gives the kinetic energies of the proton and of the sulfur atom in the center of mass frame

$$T_p^{\text{cm}} \quad = \quad \gamma^{\text{cm}}(\gamma m_p + \beta^{\text{cm}} \beta \gamma m_p) - m_p \tag{B.11}$$

$$T_{^{32}\text{S}}^{\text{cm}} \quad = \quad (\gamma^{\text{cm}} - 1) m_{^{32}\text{S}} \tag{B.12}$$

with

$$m_{^{32}\text{S}} = ME(^{32}S) + u \cdot 32 \cdot 10^6\ . \tag{B.13}$$

The total energy available for the reaction (apart from the rest masses of the projectile and the target) yields

$$T^{\text{cm}} = T_p^{\text{cm}} + T_{^{32}\text{S}}^{\text{cm}} = 3266.9 \pm 1.0\text{keV}\ , \tag{B.14}$$

which differs by 0.9 keV from 3267.8 keV quoted in [Abb70]. This difference is not due to the change in the ^{32}S mass by only ≈3 keV found by comparing the mass tables from 1965 [Mat65] and 1995 [Aud95]. Additionally, neither the values for the proton mass, the mass excess for the hydrogen atom nor the energy equivalent for the atomic mass unit u have changed enough to explain the difference found for the kinetic energy in the center of mass frame. Using (B.14) the excitation energy $E_x = 5543.4 \pm 1.1\,keV$ of the $T = 3/2, J^\pi = 1/2+$ state in ^{33}Cl differs by 0.6 keV from the value quoted in [End90].

Using T^{cm} from (B.14) the mass excess of the $T = 3/2, J^\pi = 1/2+$ state in ^{33}Cl can be calculated by

$$ME(^{32}S) + ME(^1H) + T^{\text{cm}} = -15460.1 \pm 1.0\,\text{keV}. \tag{B.15}$$

The other states of ^{33}Cl that are member of an $A = 33$ isospin quartet are listed in Tab. B.1. In Tab. 4.2 the mass excesses of all states are summarized which are relevant to the $A = 33$ isospin quartet.

Table B.1: This table gives the proton energies in the laboratory frame E_p^{lab} and the center of mass frame E_p^{cm}, the excitation energies E_x and the mass excesses ME of all states of ^{33}Cl relevant to the $A = 33$ isospin quartet. (B.14) and (B.15) were used for the calculation.

J^π	E_p^{lab} [keV]	ref.	E_p^{cm} [keV]	E_x [keV]	ME [keV]
$\frac{1}{2}+$	3370(1)	[Abb70]	3266.9(1.0)	5543.4(1.1)	-15460.1(1.0)
$\frac{3}{2}+$	4855(3)	[Abb73]	4706.3(3.0)	6982.9(3.0)	-14020.7(3.0)
$\frac{5}{2}+$	5284(3)	[Abb73]	5122.2(3.0)	7398.7(3.0)	-13604.8(3.0)

Table B.2: Constants used for the transformation.

constant	value [keV]	reference
u	0.931494013(37)	[Moh00]
m_p	938271.998(38)	[Moh00]
$ME(^{32}S)$	-26015.98(11)	[Aud95]
$ME(^{1}H)$	7288.969(1)	[Aud95]

Bibliography

[Abb70] U. Abbondanno, R. Giacomich, L. Granata, M. Lagonegro, G. Poiani, P. Blasi, and R.A. Ricci. *Isospin-forbidden analogue resonances in ^{33}Cl I: The lower $T = 3/2$ analogue resonance.* Il Nuovo Cimento **LXX A**, 391 (1970).

[Abb73] U. Abbondanno, M. Lagonegro, G. Pauli, G. Poiani, and R.A. Ricci. *Isospin-forbidden analogue resonances in ^{33}Cl II: Levels of ^{33}Cl and higher $T = 3/2$ resonances.* Il Nuovo Cimento **13A**, 321 (1973).

[Ade99] E. G. Adelberger, C. Ortiz, A. Garcia, H. E. Swanson, M. Beck, O. Tengblad, M. J. G. Borge, I. Martel, H. Bichsel, and the ISOLDE Collaboration. *Positron-Neutrino Correlation in the $0^+ \rightarrow 0^+$ Decay of ^{32}Ar.* Phys. Rev. Lett. **83**, 1299 and 3101 (1999).

[Ame98] F. Ames, G. Bollen, G. Huber, P. Schmidt, and the REX-ISOLDE collaboration. *REXTRAP, an ion buncher for REX-ISOLDE.* In D.J. Morrissey B.M. Sherrill and Cary N. Davids (eds.), *ENAM98: Exotic Nuclei and Atomic Masses*, page 927 (1998).

[Aud95] G. Audi and A.H. Wapstra. *The 1995 update to the atomic mass evaluation.* Nucl. Phys. **A595**, 1 (1995).

[Bac97] H. Backe, K. Eberhardt, R. Feldmann, M. Hies, H. Kunz, W. Lauth, R. Martin, H. Schöpe, P. Schwamb, M. Sewtz, P. Thörle, N. Trautmann, and S. Zauner. *A compact apparatus for mass selective resonance ionization spectroscopy in a buffer gas cell.* Nucl. Instr. and Meth. **B126**, 406–410 (1997).

[Bec97] D. Beck, F. Ames, G. Audi, G. Bollen, H.-J. Kluge, A. Kohl, M. König, D. Lunney, H. Raimbault-Hartmann, S. Schwarz, and J. Szerypo. *Towards higher accuracy with the ISOLTRPAP mass spectrometer.* Nucl. Instr. and Meth. **B126**, 374 (1997).

[Ben79] W. Benenson and E. Kashy. *Isobaric quartets in nuclei.* Rev. of Mod. Phys. **51**, 527 (1979).

[Ber70] G. Bertsch and S. Kahana. *T_Z^3 term in the isobaric multiplet equation.* Phys. Lett. **33B**, 193 (1970).

[Bol89] G. Bollen. *Erste Massenbestimmungen an instabilen Isotopen mit Hilfe einer Penningfalle.* PhD thesis, Johannes Gutenberg Universität, Mainz (1989).

[Bol90] G. Bollen, R. B. Moore, G. Savard, and H. Stolzenberg. *The accuracy of heavy-ion mass measurements using time of flight-ion cyclotron resonance in a Penning trap.* J. of Appl. Phys. **68**, 4355 (1990).

[Bol92] G. Bollen, H.-J. Kluge, M. König, T. Otto, G. Savard, H. Stolzenberg, R. B. Moore, G. Audi G. Rouleau, and the ISOLDE collaboration. *Resolution of nuclear ground and isomeric states by a Penning trap mass spectrometer.* Phys. Rev. **C46**, R2140 (1992).

[Bol96] G. Bollen, St. Becker, H.-J. Kluge, M. König, R. B. Moore, T. Otto, H. Raimbault-Hartmann, G. Savard, L. Schweikhard, H. Stolzenberg, and the ISOLDE Collaboration. *ISOLTRAP: a tandem Penning trap system for accurate on-line mass determination of short-lived isotopes.* Nucl. Instr. and Meth. **A368**, 675–697 (1996).

[Bol97] G. Bollen. *Radioactive Ion Beams and Penning Traps.* Nucl. Phys. **A616**, 457c–468c (1997).

[Bor87] M. J. G. Borge, P. Dessagne, G. T. Ewan, P. G. Hansen, A. Huck, B. Jonson, G. Klotz, A. Knipper, S. Mattsson, G. Nyman, C. Richard-Serre, K. Riisager, G. Walter, and the ISOLDE Collaboration. *Study of the giant Gamow-Teller resonance in nuclear beta decay. The case of* ^{33}Ar*.* Physica Scripta **36-2**, 218–223 (1987).

[Bra99] M. P. Bradley, J. V. Porto, S. Rainville, J. K. Thompson, and D. E. Pritchard. *Penning trap measurements of the masses of* ^{133}Cs*,* $^{87,85}Rb$*, and* ^{23}Na *with uncertainties* ≤ 0.2 *ppb.* Phys. Rev. Lett. **83**, 4510 (1999).

[Bre95] B. Brehm, J. Grosser, T. Ruscheinski, and M. Zimmer. *Absolute detection efficiencies of a microchannel plate detector for ions.* Meas. Sci. Technol. **6**, 953–958 (1995).

[Bri98] J. Britz, A. Pape, and M.S. Antony. *Coefficients of the isobaric mass equation and their correlations with various nuclear parameters.* At. Data Nucl. Data Tables **69**, 125–159 (1998).

[Bro86] Lowell S. Brown and Gerald Gabrielse. *Geonium theory: Physics of a single electron or ion in a Penning trap.* Review of Modern Physics **58**, 233–311 (1986).

[Car99a] C. Carlberg et al. (1999).

[Car99b] C. Carlberg, T. Fritioff, and I. Bergström. *Determination of the* ^{133}Cs *and proton mass ratio using highly charged ions.* Phys. Rev. Lett. **83**, 4506 (1999).

[Daw76] P.H. Dawson. *Quadrupole Mass Spectrometry.* Elsevier, Amsterdam (1976).

[Deh67] H.G. Dehmelt. *Radiofrequency specrtoscopy of stored ions. I: Storage.* Adv. At. Mol. Phys. **3**, 53–72 (1967).

[End78] P.M. Endt and C. van der Leun. *Energy levels of* $A = 21-44$ *nuclei (VI).* Nucl. Phys. **A310**, 1 (1978).

[End90] P.M. Endt. *Energy levels of* $A = 21 - 44$ *nuclei (VII).* Nucl. Phys. **A521**, 1 (1990).

[Fuj97] S. Fujitaka, M. Wada, H. Wang, J. Tanaka, H. Kawakami, I. Katayama, K. Ogino, H. Katsuragawa, T. Nakamura, K. Okada, and S. Othani. *Accumulation of ions from a recoil mass seperator in a new type of linear ion trap.* Nucl. Instr. and Meth. **B126**, 386–391 (1997).

[Fyn99] Hans Fynbo (1999), private communications.

[GD96] A.M. Ghalambor-Dezfuli, R.B. Moore, and P. Varfalvy. *A compact 65 keV stable ion gun for radioactive beam experiments.* Nucl. Instr. and Meth. **A368**, 611 (1996).

[Ger92] D. Gerlich. *Inhomogeneous RF fields: a versatile tool for the study of processes with slow ions.* Adv. Chem. Phys. **82**, 1–176 (1992).

[Gil99] Tim Giles (1999), private communications.

[GR92] R. B. Moore und G. Rouleau. *In flight capture of an ion beam in a Paul trap.* J. Mod. Optics **39**, 361 (1992).

[Grä80] G. Gräff, H. Kalinowsky, and J. Traut. *A direct determination of the proton electron mass ratio.* Z. Phys. **A297**, 35 (1980).

[Har74] J.C. Hardy and H. Schmeing. *Fermi beta decay: The masses of* ^{22}Mg, ^{26}Si, ^{30}S *and* ^{34}Ar. Phys. Rev. **C9**, 252 (1974).

[Har99] J.C. Hardy and I.S. Towner. *Superallowed Fermi beta decay and Coulomb mixing in Nuclei.* In C. Baktash (ed.), *AIP Conf. Proc. Nuclear Structure 98*, volume 481, page 129. AIP (1999).

[Hen69] E.M. Henley and C.E. Lacy. *Simple model for corrections to the isobaric multiplet mass equation.* Phys. Rev. **184**, 1228 (1969).

[Her00] F. Herfurth, J. Dilling, A. Kellerbauer, G. Bollen, S. Henry, H.-J. Kluge, E. Lamour, D. Lunney, R. B. Moore, C. Scheidenberger, S. Schwarz, G. Sickler, and J. Szerypo. *A linear radiofrequency ion trap for accumulation, bunching, and emittance improvement of radioactive ion beams* (2000), accepted for publication in Nucl. Instr. Meth. A, available as CERN preprint: CERN-EP/2000-062.

[Jän69a] J. Jänecke. *The quartic isobaric multiplet mass equation.* Nucl. Phys. **A128**, 632 (1969).

[Jän69b] J. Jänecke. *Systematics of coulomb energies and excitation energies of isobaric analog states (IAS).* In D.H. Wilkinson (ed.), *Isospin in nuclear physics*, pages 299–387. North-Holland Publ., Amsterdam (1969).

[Jar61] Nelson Jarmie and M.G. Silbert. *Nuclides* ^{42}Ar *and* ^{39}Cl. Phys. Rev. **123**, 909 (1961).

[Jel74] N.A. Jelley, K.H. Wilcox, R.B. Weisenmiller, G.J. Wozniak, and Joseph Cerny. *Masses for* ^{43}Ar *and the new isotopes* ^{45}Ar *and* ^{46}Ar. Phys. Rev. **C9**, 2067 (1974).

[Kel00] A. Kellerbauer, T. Kim, R.B. Moore, P.Varfalvy, and the ISOLTRAP Collaboration. *Buffer-gas cooling of ion beams.* submitted to Nucl. Instr. Meth. A (2000).

[Ken85] T.J. Kennett, W.V. Prestwich, and J.S. Tsai. *Radiative thermal neutron capture by natural sulfur.* Z. Phys. **A322**, 121 (1985).

[Koh99] A. Kohl. *Direkte Massenbestimmung in der Bleigegend und Untersuchung eines Starkeffekts in der Penningfalle.* PhD thesis, Ruprecht Karls Universität, Heidelberg (1999).

[Kön95] M. König, G. Bollen, H.-J. Kluge, T. Otto, and J. Szerypo. *Quadrupole excitation of stored ion motion at the true cyclotron frequency.* Int. J. Mass Spectr. Ion. Proc. **142**, 95 (1995).

[Kre90] Martin Kretzschmar. *Single paricle motion in a Penning trap: Description in the classical canonical formalism.* Physica Scripta **46**, 544–554 and 555–559 (1990).

[Kud98] Y. Kudryavtsev, S. Franchoo, J. Gentens, M. Huyse, R. Raabe, I. Reusen, P. Van Duppen, P. Van Den Bergh, L. Vermeeren, and A. Wöhr. *Status of the laser ion source at the Leuven isotope separator online.* Rev. Sci. Instrum. **69**, 738–740 (1998).

[Kug92] E. Kugler, D. Fiander, B. Jonson, H. Haas, A. Przewloka, H.L. Ravn, D.J. Simon, K. Zimmer, and the ISOLDE Collaboration. *The new CERN-ISOLDE on-line mass-separator facility at the PS-Booster.* Nucl. Instr. and Meth. **B70**, 41–49 (1992).

[Kug00] E. Kugler. *The ISOLDE facility.* Hyperfine Interactions **129**, 23–42 (2000).

[Let97] J. Lettry, R. Catherall, P. Drumm, P. van Duppen, A.H.M. Evensen, G.J. Focker, A. Jokinen, O.C. Jonsson, E. Kugler, H.L. Ravn, and the ISOLDE Collaboration. *Pulse shape of the ISOLDE radioactive ion beams.* Nucl. Instr. and Meth. **B126**, 130–134 (1997).

[Lun99] M.D. Lunney and R.B. Moore. *Cooling of mass-separated beams using a radiofrequency quadrupole ion guide.* Int. J. Mass Spectrom. Ion Proc. **190/191**, 153–160 (1999).

[Mat65] J.H.E. Mattauch, W. Thiele, and A.H. Wapstra. *The 1995 update to the atomic mass evaluation.* Nucl. Phys. **67**, 1–31 (1965).

[McD73] E.W. McDaniel and E.W. Mason. *The Mobility and Diffusion of Ions in Gases.* Wiley (1973).

[Mee53] J.M. Meek and J.D. Craggs. *Electrical Breakdown of gases 1st ed.* Oxford publishing (1953).

[Moh00] P.J. Mohr and B.N. Taylor. *CODATA recommended values of the fundamental physical constants: 1998.* Review of Modern Physics **72**, 351 (2000), 1998 CODATA values.

[Nan74] H. Nann, W. Benenson, E. Kashy, and P. Turek. *Isobaric mass quartets in* $A = 33$ *nuclei.* Phys. Rev. **C9**, 1848 (1974).

[Obe97] J. Oberheide, P. Wilhelms, and M. Zimmer. *New results on the absolute detection efficiencies of a microchannel plate.* Meas. Sci. Technol. **8**, 351–354 (1997).

[Pau90] W. Paul. *Electromagnetic traps for charged and neutral particles.* Review of Modern Physics **62**, 531–540 (1990).

[Pen97] H. Penttilä, P. Dendooven, A. Honkanen, M. Huhta, P.P. Jauho, A. Jokinen, G. Lhersonneau, M. Oinonen, J.-M. Parmonen, K. Peräjärvi, and J. Äystö. *Status report of the Jyväskylä ion guide isotope seperator on-line facilitiy.* Nucl. Instr. and Meth. **B126**, 213–217 (1997).

[Rai97] H. Raimbault-Hartmann, D. Beck, G. Bollen, M. König, H.-J. Kluge, E. Schark, J. Stein, S. Schwarz, and J. Szerypo. *A cylindrical Penning trap for capture, mass selective cooling, and bunching of ioactive ion beams.* Nucl. Instr. and Meth. **B126**, 378 (1997).

[Ram85] S. Raman, R. F. Carlton, J. C. Wells, E. T. Jurney, and J. A. Lynn. *Thermal neutron capture gamma rays from sufur isotopes: Experiment and theory.* Phys. Rev. **C32**, 18 (1985).

[Sav91] G. Savard, St. Becker, G. Bollen, H.-J. Kluge, R. B. Moore, Th. Otto, L. Schweikhard, H. Stolzenberg, and U. Wiess. *A new cooling technique for heavy ions in a Penning trap.* Phys. Lett. **A158**, 247 (1991).

[Sav99] G. Savard (1999), Argonne National Laboratory, private communication.

[Sch99] S. Schwarz. *Manipulation radioaktiver Ionenstrahlen mit Hilfe einer Paulfalle und direkte Massenmessungen an neutronenarmen Quecksilberisotopen mit dem ISOLTRAP-Experiment.* PhD thesis, Johannes Gutenberg Universität, Mainz (1999), ISBN 3-8288-0735-6.

[Sch01] Pit Schmidt. *REXTRAP - Ion accumulation, cooling and bunching for REX-ISOLDE.* PhD thesis, Johannes Gutenberg University, Mainz (2001).

[Sok65] A.A. Sokolov and Y.G. Pavlenko. *Induced and spontaneous emission in crossed fields.* Opt. Spectrosc. **22**, 1 (1965).

[Sto90] H. Stolzenberg, St. Becker, G. Bollen, F. Kern, H.-J. Kluge, Th. Otto, G. Savard, and L. Schweikhard. *Accurate mass determination of short-lived isotopes by a tandem Penning-trap mass spectrometer.* Phys. Rev. Lett. **65**, 3104 (1990).

[Tel74] E. Teloy and D. Gerlich. *Integral cross sections for ion-molecule reactions. I. The guided beam technique.* Chem. Phys. **4**, 417–427 (1974).

[Wam80] H. R. Wampfler and V. Meyer. *Isospin-verbotene* $T = 3/2$ *Analogresonanzen in* ^{33}*Cl.* Helv. Phys. Acta **53**, 317 (1980).

[Wig57] E. P. Wigner. Proc. of the Robert A. Welch foundation conference on chemical research, Houston, ed. W. O. Millikan (1957), Vol.1.

[Wol87] H. Wollnik, J. Brezina, and M. Berz. *GIOS-BEAMTRACE – A program package to determine optical properties of intense ion beams.* Nucl. Instr. and Meth. **A258**, 408–411 (1987).

Acknowledgement

With these short and certainly not always adequate words I would like to express my gratitude to all the people who made this work possible.

I would like to thank Prof. H.-J. Kluge and Prof. G. Bollen for their confidence, for the unique possibility they gave me and of course for their support throughout the time I spent at ISOLTRAP.

I thank the numerous collaborators who were able to bear with me grumbling trying to run ISOLTRAP. Special thank goes to Alex, Didi and Stefan who showed me most of the secrets (they left some fun for me) of how to run an untoward apparatus. Thank you Bob for the ideas leading to a device that stimulated me to free skills I did not know about and that gave outstanding results providing a major part of this thesis. I would also like to thank Jens for the excellent preparation of the buncher before it came to CERN and of course for the hard work we went through together. To Alban, Christoph, Günther, Gerrit, Emily, Jerome, Jurek and Sylvain goes my thank for their valuable help during the setup of the ISOLTRAP ion beam cooler and buncher and during the radioactive beam times.

Additionally I want to acknowledge the continuous support from our trapper friends from REXTRAP, Friedhelm, Oliver and Pit.

I also thank J. Zimmer, C. Chollet and the people from the mechanical workshops that supported our amateurish approach to engineering.

I would like to thank J. Äystö and A. García for an introduction into the physics related to the IMME and for detailed discussions on it.

Many thanks go to Dave who certainly damns the day when he offered me to proofread my thesis.

Thank you, Georges, for the insight into the atomic mass evaluation and for the very helpful discussions not only on uncertainties.

I would like to thank the people of the “technical” group of ISOLDE for the support they gave running the experiment. And of course there are more people at ISOLDE and elsewhere who answered my questions, motivated me, trusted me, criticized me and helped me to enjoy the life during working hours and far beyond.

The people who suffered most from my work are the ones I love most, my wife Ramona and my children Florian and Lucas. Last but not least their everlasting patience and support gave me the power to go through all the ups and downs such a big project entails.

Finally, I want to express special gratitude to my parents who helped me to go my way wherever it took me.